Mechanistic dissection of myosin Va-based melanosome transport *in vitro*

Dissertation zur Erlangung

des akademischen Grades

„Doktor der Naturwissenschaften"

(Dr. rer. nat.)

an der Fakultät für Biologie

der Ludwig-Maximilians-Universität München

vorgelegt von

Angela Oberhofer

München, 21.06.2017

Erstgutachter: Hr. Prof. Dr. Manfred Schliwa

Zweitgutachterin: Fr. Prof. Dr. Angelika Böttger

Dissertation eingereicht am: 21.06.2017

Tag der mündlichen Prüfung: 26.10.2017

Zusammenfassung

Essenzielle zelluläre Prozesse wie Zellwachstum, Teilung und Transport von Cargo sind auf intrazellulären Transport angewiesen. Die dafür verantwortliche Transportmaschinerie besteht aus molekularen Motoren, die sich direktional auf Aktinfilamenten und Mikrotubuli, die als ‚zelluläre Straßen' fungieren, bewegen. Myosin Motoren laufen auf Aktinfilamenten, während Mikrotubuli den entgegengesetzt gerichteten Kinesin und Dynein Motoren als Straßen dienen. Interessanterweise sind in vielen Fällen die koordinierten (oder konkurrierenden) Aktivitäten der entsprechenden Aktin- und Mikrotubuli-basierten Transportsysteme für Cargotransport *in vivo* erforderlich. Trotz dem detaillierten Wissen über jedes einzelne Transportsystem sind nur sehr spärliche Informationen über die funktionelle Verbindung zwischen dem Aktin/Myosin- und dem Mikrotubuli/Kinesin/Dynein-System erhältlich. Um diese Lücke zu schließen konzentriert sich diese Arbeit auf die Frage: Wie kommunizieren die Aktin- und Mikrotubuli-basierten Transportsysteme um die richtige Zustellung von Cargo zu gewährleisten? Um Einblicke in die Mechanismen zu erhalten, die die Aktin- und Mikrotubuli-basierten Transportsysteme verbinden, habe ich Pigmentzellen (Melanophoren) von der Amphibie *Xenopus laevis* und Melanozyten von der Maus als zwei gut etablierte Modellsysteme verwendet. In Melanophoren werden Pigmentgranulen (Melanosomen) durch die vereinten Kräfte der Mikrotubuli-basierten Dynein-1 und Kinesin-2 Motoren und dem Aktin-basierten Myosin Va Motor transportiert. Dieser Transport findet durch extrazelluläre Signale statt, die die Direktionalität des Melanosomentransports *in vivo* definieren. Es ist lange bekannt, das die Proteinkinase A (PKA) den nach innen gerichteten (Aggregation, niedrige PKA-Aktivität) und nach außen gerichteten (Dispersion, erhöhte PKA-Aktivität) Melanosomentransport dirigiert. Trotzdem blieben die molekularen Mechanismen, die eine solche direktionale Verteilung regulieren, die letzten zwei Jahrzehnte unbekannt.

Vorangegangene Arbeit enthüllte zahlreiche Details der Mikrotubuli-basierten Transportmaschinerie, wohingegen nur wenig über das Aktin-basierte Transportsystem bekannt ist, das essenziell für den Dispersionsprozess ist. Um mechanistische Einblicke in die Aktin-basierte Transportmaschinerie des Melanosomentransportes zu geben, habe ich die Aktin-basierte Motilität von aufgereinigten Melanosomen *in vitro* rekonstituiert. Außerdem habe ich die Komponenten der Aktin-basierten Transportmaschinerie (der

dreiteilige Myosin Va Transportkomplex, der aus Rab27a, Melanophilin und Myosin Va besteht) von *Xenopus laevis* und Maus rekombinant exprimiert um eine umfangreiche *in vitro* Charakterisierung durchzuführen.

Die Rekonstitution des Aktin-basierten Melanosomentransportes *in vitro* zeigte, dass Melanosomen von Zellen mit hoher PKA-Aktivität (dispergierter Zellstatus) einen signifikant erhöhten Myosin Va-abhängigen Transport aufweisen verglichen mit Melanosomen von Zellen mit niedriger PKA-Aktivität (aggregierter Zellstatus). Die Charakterisierung der Transportparameter des rekonstituierten Melanosomentransportes *in vitro* zeigte, dass PKA-Aktivität keinen Einfluss auf Geschwindigkeit oder Lauflänge der Melanosomen hatte. Ich habe die PKA als molekularen Schalter identifiziert, der direkt den Transport zwischen den entsprechenden Zellstatus auf der Melanosomenoberfläche reguliert. *In vitro* Phosphorylierungsexperimente mit den rekombinant exprimierten Komponenten Rab27a, Melanophilin und Myosin Va, die den dreiteiligen Myosin Va Transportkomplex *in vivo* bilden, demonstrieren, dass das Adaptorprotein Melanophilin das spezifische Phosphorylierungsziel der PKA in Xenopus und Maus ist. Besonders Melanophilin's C-terminale Aktinbindedomäne ist ausgeprägtes Ziel der Phosphorylierung. Es ist beachtenswert, dass die *in vitro* Phosphorylierung von Melanophilin's Aktinbindedomäne dem bereits beschriebenen *in vivo* Phosphorylierungsmuster sehr ähnlich ist.

In meiner Arbeit stelle ich eine effiziente Strategie zur Assemblierung des dreiteiligen Myosin Va Transportkomplex *in vitro* vor, die es mir ermöglichte die funktionalen Konsequenzen der Melanophilin-Phosphorylierung *in vitro* zu testen. Dekorationsexperimente mit Aktin und dem Rab27a/Melanophilin-Komplex und Einzelmolekül-TIRF (interne Totalreflexionsfluoreszenz)-Mikroskopie-Experimente mit dem dreiteiligen Rab27a/Melanophilin/Myosin Va-Komplex auf Aktinfilamenten deckten unerwartet auf, dass die Phosphorylierung von Melanophilin's Aktinbindedomäne nicht in Aktin-abhängige Prozesse, wie Melanophilin's Bindung zu Aktin oder der Bewegung des Myosin Va-Transportkomplex auf Aktinfilamenten, eingreift. Stattdessen regulierte Melanophilin's Phosphorylierungsstatus überraschend Melanophilin's Assoziation mit Mikrotubuli. Dephosphoryliertes Melanophilin zog die Bindung zu Mikrotubuli sogar in Gegenwart von Aktinfilamenten vor, währenddessen phosphoryliertes Melanophilin

hauptsächlich mit Aktinfilamenten assoziierte auch wenn Mikrotubuli gegenwärtig waren. Tatsächlich gibt Melanophilin's Phosphorylierungsstatus vor, welches Filament der Rab27a/Melanophilin/Myosin Va-Komplex wählt, wenn Mikrotubuli und Aktinfilamente gleichzeitig vorhanden sind. Genauer gesagt zeigte der dreiteilige Myosin Va-Transportkomplex mit phosphorylierten Melanophilin hauptsächlich direktionale Bewegung auf Aktinfilamenten *in vitro*, wie es von einem Aktin-basierten Motorprotein erwartet wird. Im Gegensatz dazu verstärkte die Dephosphorylierung von Melanophilin die Interaktion des dreiteiligen Myosin Va-Transportkomplexes mit Mikrotubuli und eine signifikante Anzahl an Komplexen zeigte Diffusion auf Mikrotubuli. Diese Ergebnisse decken die überraschende regulatorische Dominanz des Adaptorproteins Melanophilin über sein assoziertes Motorprotein Myosin Va auf und bieten einen Mechanismus an, wie Kommunikation zwischen dem Aktin- und Mikrotubuli-Transportsystemen *in vivo* bewerkstelligt werden könnte, und zwar durch das Adaptorprotein Melanophilin, das imstande ist mit Aktinfilamenten als auch mit Mikrotubuli zu interagieren. Die Bindungspreferenz des gesamten dreiteiligen Myosin Va- Transportkomplexes zu Aktinfilamenten oder Mikrotubuli wird durch den Phosphorylierungsstatus von Melanophilin reguliert. Zusammengenommen bieten die Beobachtungen dieser Arbeit erste Einblicke in das funktionelle Zusammenspiel zwischen den zwei zytoskelettalen Transportsystemen und stellen eine mechanistische Erklärung bereit, wie Zellen den Transport auf dem einen oder anderen zytoskelletalen Filament verschieben könnten.

Summary

Essential cellular processes such as cell growth, division, migration, and cargo delivery rely on intracellular transport. The transport machinery responsible for such processes consists of molecular motors that move directionally on actin filaments or microtubules, which serve as 'cellular roads'. Myosin motors walk on actin filaments, whereas microtubules serve as tracks for the oppositely directed kinesin and dynein motors. Interestingly, in many cases, the coordinated (or competing) activities of the respective actin- and microtubule-based systems are required for cargo transport *in vivo*. Despite the detailed knowledge on each individual transport system, only very sparse information is available on the functional interface between the actin/myosin- and the microtubule/kinesin/dynein-systems. To close this gap, this thesis is focused on the question: how is crosstalk between the actin- and microtubule-based transport systems achieved to bring about correct cargo delivery? To gain insights into the mechanisms that link the actin- and microtubule-based transport systems, I used pigment cells (melanophores) from the amphibian *Xenopus laevis* and melanocytes from mouse as two well-established model systems. In melanophores, pigment granules (melanosomes) are transported by the concerted action of the microtubule-based dynein-1 and kinesin-2 motors and the actin-based myosin Va motor upon external cues that in turn define the overall directionality of transport *in vivo*. It is long known that protein kinase A (PKA) orchestrates the inward (aggregation, decreased PKA activity) and the outward (dispersion, increased PKA activity) of movement of melanosomes. However, molecular mechanism(s) of how such directional distribution is regulated remained elusive over the past two decades.

Previous work illuminated numerous details of the microtubule-based transport machinery that move the melanosome, whereas only little is known about the actin-based transport system that is essential for the dispersion process. To provide mechanistic insights into the actin-based machinery of melanosome transport, I reconstituted the actin-based motility of purified melanosomes *in vitro*. Furthermore, I recombinantly expressed the components of the actin-based transport machinery (the tripartite myosin Va transport complex consisting of Rab27a, melanophilin, and myosin Va) from *Xenopus laevis* and mouse to perform an extensive *in vitro* characterization.

Reconstituting the actin-based transport of melanosomes *in vitro* revealed that melanosomes from cells with high PKA activity (i.e. dispersed cell state) exhibit significantly increased myosin Va-dependent transport compared to melanosomes derived from cells with low PKA activity (i.e. aggregated cell state). Characterizing the transport parameters of the reconstituted melanosome transport *in vitro* showed that PKA activity did not influence velocity or run length of melanosomes. I identified PKA as the molecular switch that directly regulates this transport between the respective cell states on the melanosome surface. *In vitro* phosphorylation assays with the recombinantly expressed components Rab27a, melanophilin, and myosin Va that form the myosin Va tripartite transport complex *in vivo* demonstrate that the adaptor protein melanophilin is the specific phosphorylation target of PKA in *Xenopus* and mouse. Particularly melanophilin's C-terminal actin-binding domain is a pronounced phosphorylation target. Of note, *in vitro* phosphorylation of melanophilin's actin-binding domain closely resembled the previously described *in vivo* phosphorylation pattern.

In my work, I present an efficient strategy to assemble the tripartite myosin Va transport complex *in vitro* that enabled me to test the functional consequences of melanophilin phosphorylation *in vitro*. Filament decoration assays with actin and the Rab27a/melanophilin complex and single-molecule total internal reflection fluorescence (TIRF) microscopy assays with the tripartite Rab27a/melanophilin/myosin Va complex on actin filaments revealed unexpectedly that phosphorylation of melanophilin's actin-binding domain did not interfere with actin-dependent processes such as binding of melanophilin to actin filaments or movement of the tripartite complex along actin filaments. Surprisingly instead, melanophilin's phosphorylation state regulated its association with microtubules *in vitro*. Dephosphorylated melanophilin preferred to bind to microtubules even in the presence of actin filaments, whereas phosphorylated melanophilin predominantly associated with actin filaments when microtubules were also present. In fact, melanophilin's phosphorylation state enforced track selection of the tripartite Rab27a/melanophilin/myosin Va complex when microtubules and actin filaments were present simultaneously. More precisely, the tripartite complex assembled with phosphorylated melanophilin mostly exhibited directional movement on actin filaments *in vitro*, as expected of an actin-based motor protein. In contrast, dephosphorylation of melanophilin enhanced the interaction between the tripartite complex and microtubules

and a signification number of complexes showed diffusional movement on microtubules. These results reveal the surprising regulatory dominance of the adaptor protein melanophilin over its associated motor protein myosin Va and provide a mechanism of how crosstalk between the actin- and microtubule-transport systems might be achieved *in vivo*; namely through the adaptor protein melanophilin that is capable of interacting with both actin filaments and microtubules. The binding preference of the entire tripartite complex for actin or microtubules is regulated via the phosphorylation state of melanophilin. Taken together, the observations presented in this thesis offer first insights into the functional interface between the two cytoskeletal transport systems and provide a mechanistic explanation how cells might bias cargo transport on one or the other cytoskeletal filament.

Eidesstattliche Erklärung

Ich versichere hiermit an Eides statt, dass die vorgelegte Dissertation von mir selbstständig und ohne unerlaubte Hilfe angefertigt ist. Ich habe weder anderweitig versucht eine Dissertation einzureichen oder eine Doktorprüfung abzulegen, noch habe ich diese Dissertation oder Teile derselben einer anderen Prüfungskommission vorgelegt.

München, 21.06.2017

Angela Oberhofer

Table of contents

1. <u>Introduction</u>

1.1 <u>Melanosome transport in general and as model system to study intracellular transport</u>

Directed intracellular transport is central to the survival of all eukaryotic cells and pivotal processes such as cell division (1-3), neuronal signaling (4), organization of endomembranes (5), secretion (6), and transport of organelles (7, 8) depend on it. Three super families of molecular motors – dyneins, kinesins and myosins – move on the two cytoskeletal tracks – actin and microtubule (MT) filaments – to transport cargo to its destined place in the cell. Especially, the correct delivery of the vast majority of cargo utilizes the coordinated action of both cytoskeletal systems in the cell. Based on the work of many groups during the last decades, we now have a detailed knowledge on how each transport system works individually, whereas only very limited information is available on how the two cytoskeletal systems are coordinated and crosstalk is brought about to ensure proper intracellular transport of, e.g. organelles. One excellent and well-established model system to study the coordinated action of both cytoskeletal transport systems is the melanosome transport in pigment cells from amphibians or mammals.

Melanosomes are membrane-bound organelles specialized for the synthesis, storage, and transport of the brown-black pigment melanin that reside in epithelial cells termed melanophores in amphibians or melanocytes in mammals, respectively. Melanophores and melanocytes are flat cells that possess protrusions radiating out from the cell body. Pigment cells exist in different colors like brown-black, yellow-red, yellow, red, and white-metal (9). Brown-black pigment cells (melanophores/melanocytes) are the most widespread type of pigment cell and are responsible for most of the dorsal pigmentation in vertebrates. They enable organisms to change the color of their skin and thus serve diverse biological functions including camouflage, sexual display and protection from UV radiation, amongst others. Additionally, it is speculated that melanosomes are involved in the innate immune system in a yet unknown way (10). In order to fulfill these versatile functions, melanosomes need to be synchronously moved intra- (e.g. amphibians and fish) or intercellularly (mouse and human) in response to environmental cues. The process of transporting melanosomes toward the cell periphery to distribute them evenly throughout

the cytoplasm is called dispersion (Figure 1 A). By enlarging the cellular area occupied by dark melanosomes, the organism (i.e. amphibians and fish) appears darker.
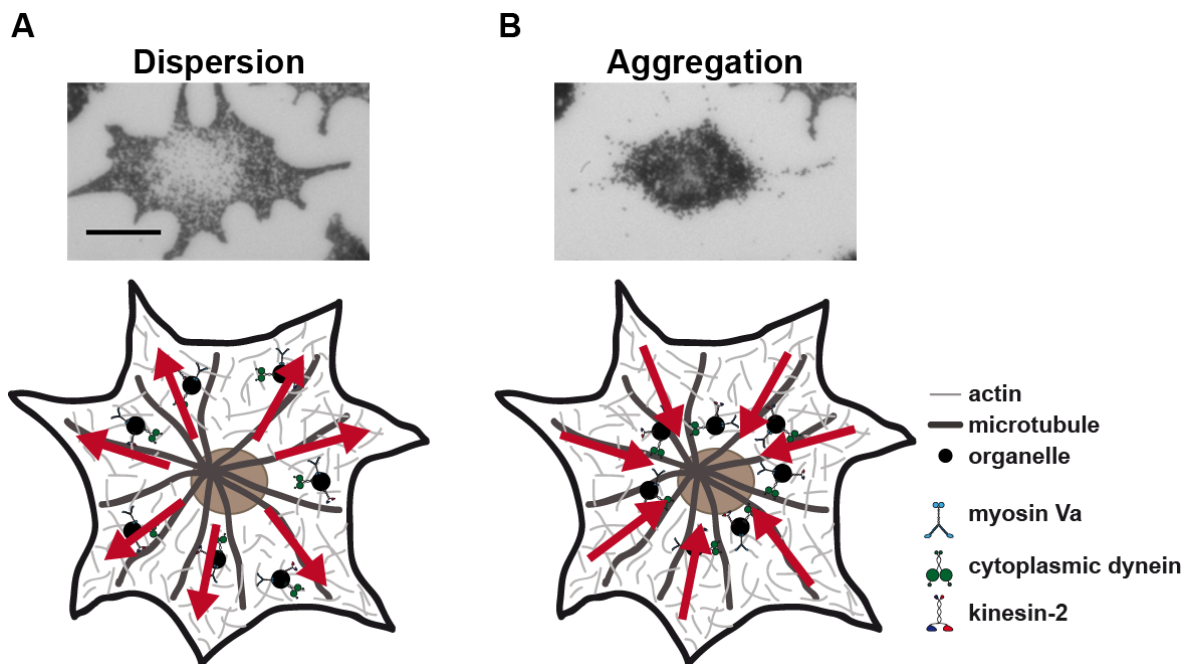
Figure 1: Dispersed and partially aggregated melanophore from the immortalized *Xenopus laevis* cell line. (A) Melanosomes were stimulated to undergo dispersion by adding 100 nM α-MSH (upper panel). Schematic illustration depicting the dispersion process and its net transport direction to the cell periphery (lower panel). (B) Identical cell as in (A) was stimulated to aggregate the melanosomes in the cell center with 50 nM melatonin (upper panel). Melanosomes are gathered in the cell center during aggregation (lower panel). Scale bar: 50 μm.

The opposite-directed transport of melanosomes towards the cell center is termed aggregation (Figure 1 B). Thereby, the dark melanosomes are concentrated in the perinuclear region of the cell, the occupied area by black pigment is minimized and the skin of the organism appears brighter. Thus, melanosome transport in amphibians and fish is a dynamic and reversible process that enables the animal to adapt to its fast-changing environment.

In contrast, melanosomes in mammals are mainly transported toward the cell periphery to be transferred to neighboring keratinocytes that are located in the skin epidermis. In keratinocytes, the melanosomes cluster around the nucleus to protect the DNA from harmful UV radiation. This transport process occurs upon exposure to sun light and is much slower than dispersion in amphibians or fish. Moreover, the main transport direction in the mammalian system is toward the cell membrane to hand melanosomes over to adjacent keratinocytes.

The establishment of an immortalized cell line of melanophores from *Xenopus laevis* by Lerner and coworkers in 1990 (11) paved the way for using these cells as a model system to explore intracellular transport. Melanophores are easily and in high quantities maintained in tissue culture and melanosome transport can be stimulated by the addition of hormones to the growth medium. Furthermore, their size (ca. 500 nm in diameter) and black color make them extremely suitable for microscopy and easily distinguishable from other organelles. In the late 90s, Gelfand and coworkers developed a method to isolate functional melanosomes and reconstitute melanosome transport *in vitro* (12), opening new perspectives on investigating and manipulating melanosome transport *in vitro*. In this study, it was made use of the immortalized *Xenopus laevis* melanophore cell line and the previously developed method to isolate pigment granules for subsequent *in vitro* dissection of pigment granule transport.

1.2 Cytoskeletal components involved in melanosome transport

The transport of melanosomes is achieved by the movement of three distinct motor proteins from all known super families: dyneins, kinesins, and myosins. They are attached to the organelle surface and walk unidirectionally on polar cytoskeletal filaments by converting the chemical energy of ATP hydrolysis into steps along the filament. The motor proteins involved in melanosome transport are the two MT-based molecular motors kinesin-2, which is plus-end directed, and cytoplasmic dynein, which walks toward the minus-end of MTs (12-14).
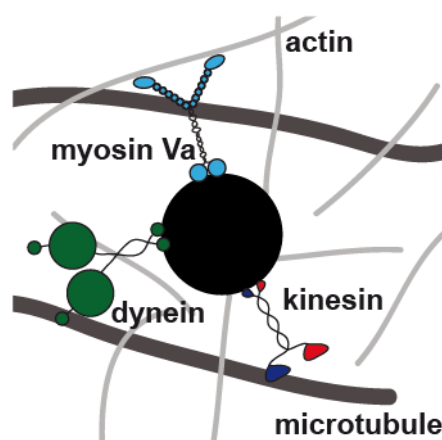
Figure 2: The three molecular motors dynein, kinesin-2 and MyoVa are attached to the melanosome and work together to achieve its proper transport within the cell. The MT-based motor protein cytoplasmic dynein is colored in green, MT-based heterodimeric kinesin-2 is depicted in dark blue and red, and the actin-based molecular motor MyoVa is illustrated in light blue.

Additionally, the actin-based motor protein myosin Va (MyoVa) is responsible for transport of melanosomes on actin filaments (8, 15). Therefore, melanosomes are transported on

both cytoskeletal tracks used for cargo transport inside cells: microtubule and actin filaments. Orientation and localization of these 'cellular roads' within pigment cells significantly impact the transport of melanosomes. Using immunocytochemistry with fluorescently labeled antibodies, fluorescence microscopy revealed the distribution of each filament type in melanophores (Figure 3).
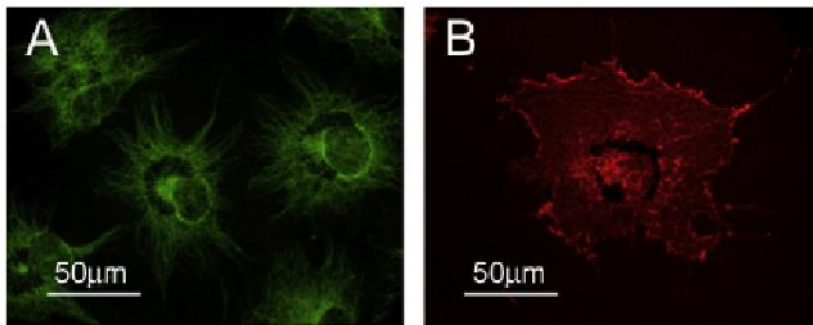
Figure 3: Distribution of cytoskeletal filaments in *Xenopus laevis* melanophores in the aggregated cell state. (A) MTs are arranged in a radial array in melanophores. MTs were labeled in fixed cells with α-tubulin primary antibody and fluorescein-linked secondary antibody. (B) Actin filaments are randomly oriented and more abundant at the cell margins and were labeled using rhodamine phalloidin. Figure 3 is taken and adapted from (16).

MTs are unipolarly distributed within melanophores with their minus-ends located at the microtubule organization center (MTOC) close to the nucleus and their plus-ends pointing toward the cell membrane (Figure 3 A) (17). Early studies on frog and fish melanophores with microtubule-disrupting drugs like nocodazole or colchicine demonstrated that melanosome transport was MT-dependent, because the treatment resulted in both inhibited aggregation and dispersion of pigment granules (18-20). Nevertheless, little motion of melanosomes was still observable after nocodazole treatment, suggesting the existence of yet another transport mechanism (21).

In contrast to MT distribution, actin filaments are randomly distributed throughout the cytoplasm with their polar ends pointing in every direction, showing a higher concentration close to the membrane (Figure 3 B). Disruption of the actin cytoskeleton with the drugs cytochalasin or latrunculin exhibits distinct effects in frog and fish melanophores. The absence of the actin-system in frog melanophores leads to melanosome accumulation in the cell center (15), whereas melanosomes in fish melanophores are transported to the cell margins; a process referred to as hyperdispersion (22). Mammalian melanocytes behave similar to frog melanophores to disruption of the actin cytoskeleton, as melanosomes are

clustered in the cell center and dispersion cannot be achieved anymore (23). These differential behaviors of frog and fish melanophores point to a distinct contribution of the MT- and actin-systems to the overall transport of melanosomes in frog and fish. The MT-system seems to be more dominant in fish melanophores because it is able to transport melanosomes all the way to the plus-ends in the absence of actin filaments. Conversely, the actin-system appears to play a stronger role in frog cells and mammalian melanocytes, as the MT-system alone is not capable of accomplishing melanosome dispersion when actin filaments are disrupted.

1.2.1 MT-based transport of melanosomes

MTs are tubular polymers (ca. 25 nm in diameter) comprised of α- and β-tubulin dimers and possess distinct polarity. The fast growing end is termed the plus-end, whereas the slower growing end that often nucleates from a MTOC or centrosome is called the minus-end. Two motor protein super families – kinesins and dyneins – use microtubule filaments as their tracks and follow the polarity of the roads in distinct directions. Most members of the kinesin superfamily move toward the plus-end of MT, while all known dynein motors walk toward the minus-end of MT. The unipolar microtubule organization enables the transport of organelles to the plus-ends of MT, thus to the cell periphery, by kinesin-2 and the transport toward the minus-ends of MT and the cell center by cytoplasmic dynein. Thus, aggregation of melanosomes in the cell center is mainly achieved by the molecular motor cytoplasmic dynein that transports melanosomes all the way to the minus-ends of MTs, which are all located close to the cell nucleus. Vice versa, kinesin-2 is responsible for delivering melanosomes closer to the cell margins. If kinesin-2 was the only molecular motor involved in the dispersion process, melanosomes would all cluster at the cell membrane. As melanosomes are evenly distributed throughout the entire cytoplasm during the dispersion process, another transporter is needed: the actin-based motor protein MyoVa that moves on actin filaments is involved in melanosome distribution as well (for a detailed description see section 1.2.2). To ensure complete dispersion, kinesin-2 delivers melanosomes to the dense actin network in the cell cortex followed by MyoVa-mediated transport on actin to achieve an even distribution within the entire cell. Vice versa, melanosomes need to be brought in close proximity to MTs by MyoVa where they are further transported toward the cell center by dynein for aggregation.
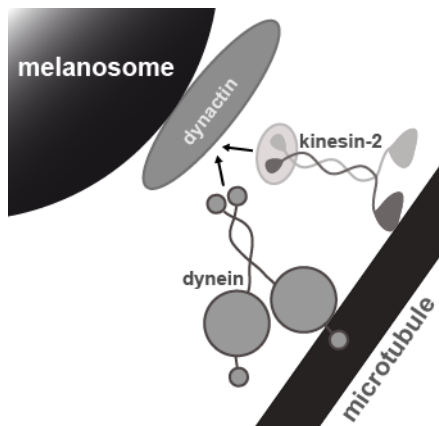
Figure 4: The dynactin complex links cytoplasmic dynein to the melanosome membrane and is also implicated to anchor kinesin-2 to the organelle via the identical domain in p150^{Glued}. The dynein intermediate chain binds to a N-terminal coiled-coil region in p150^{Glued}, dynactin's largest subunit. Immunoprecipitation assays with kinesin-2 and p150^{Glued} suggested an interaction that inhibited simultaneous binding of dynein (30).

The attachment of cytoplasmic dynein to its cargos is well characterized (24-27). The multimeric protein complex dynactin, specifically the subunit p150^{Glued}, binds to the intermediate chain of dynein, linking the dynein motor to the cargo surface. Furthermore, dynactin has been shown to increase dynein's activity and processivity (28). Surprisingly, blocking p150^{Glued} function in extruded squid axoplasm led to the inhibition of both minus- and plus-end directed transport of organelles along MTs (29). Based on that observation, Deacon et al. investigated whether there was an interaction between kinesin-2 and the dynactin complex. Indeed, they showed that the dynactin complex directly binds to kinesin-2, implicating the anchorage of kinesin-2 to the melanosome membrane in *Xenopus laevis* melanophores via dynactin (30). More precisely, the non-motor subunit of kinesin-2, kinesin-associated protein (KAP), was shown to bind to the identical domain of p150^{Glued} as the dynein intermediate chain does.

1.2.2   Actin-based transport of melanosomes

Actin is a very abundant, globular protein that is either present in the cell as a monomer (i.e. G-actin) or polymerized into linear, polar actin filaments (or filamentous actin, F-actin). The polarity derives from the identical orientation of the subunit G-actin and leads to one barbed end (or plus-end) and one pointed end (or minus-end) of the actin filament. Actin filaments are randomly distributed in the cytoplasm of melanophores with a higher concentration close to the cell membrane. Transport of melanosomes by the actin-based motor protein MyoVa that moves toward the barbed end of F-actin thus results in a rather even distribution of melanosomes in the cytoplasm with a higher tendency in close proximity to the cell membrane. MyoVa is the best characterized non-muscle myosin (unconventional myosin) that is involved in a wide range of transport processes (31). Two

identical polypeptide chains homodimerize to assemble a double-headed motor protein that walks in a hand-over-hand fashion on the actin filament toward the barbed end (32).

Figure 5: Domain structure of MyoVa. (A, B) MyoVa possesses an N-terminal catalytic head domain with ATP- and actin-binding sites, followed by a neck domain that binds calmodulins and the C-terminal tail domain for dimerization and cargo binding. The head domain binds to actin and by a conformational change of the neck domain MyoVa is able to take consecutive steps along an actin filament (i.e. MyoVa walks processively on actin).

Three domains are typical for the myosin family: (i) the usually N-terminally located head domain containing the ATP- and actin-binding sites, (ii) the so-called neck domain or lever arm that links the head domain to the stalk and contains a variable number of IQ motifs, and (iii) the tail domain or stalk that is comprised of a coiled-coil region for homodimerization followed by a globular tail domain (GTD) consisting only of α-helices and loops that is proposed to be involved in cargo binding. The coiled-coil region of MyoVa's tail in addition contains six alternatively spliced exons A-F (33, 34), determining MyoVa's cargo specificity in combination with the GTD (35). By alternately binding and releasing of the two head domains and a conformational change upon ATP hydrolysis, MyoVa is able to move processively along actin filaments (36). The melanocyte-specific isoform of MyoVa contains the alternatively spliced exons ACDEF (37).

Genetic studies of three coat color mutants in mouse led to a detailed understanding of MyoVa's attachment to the melanosome (34, 38, 39). These three mutations share a similar phenotype where melanosomes are clustered in the perinuclear region and melanosome dispersion is not correctly accomplished. A similar effect of perinuclear clustering is provoked by disrupted actin filaments (see section 1.2, page 17), suggesting that the mutations affect the actin-based transport of melanosomes. Analysis of these mutations revealed the tripartite MyoVa transport complex that is required for actin-based melanosome motility to achieve dispersion in mouse melanocytes (40-42) (Figure 6). The two proteins involved in linking MyoVa to the melanosome are Rab27a and melanophilin

(Mlph). The complex formed by these three proteins is referred to as the tripartite complex or MyoVa transport complex (41-43).
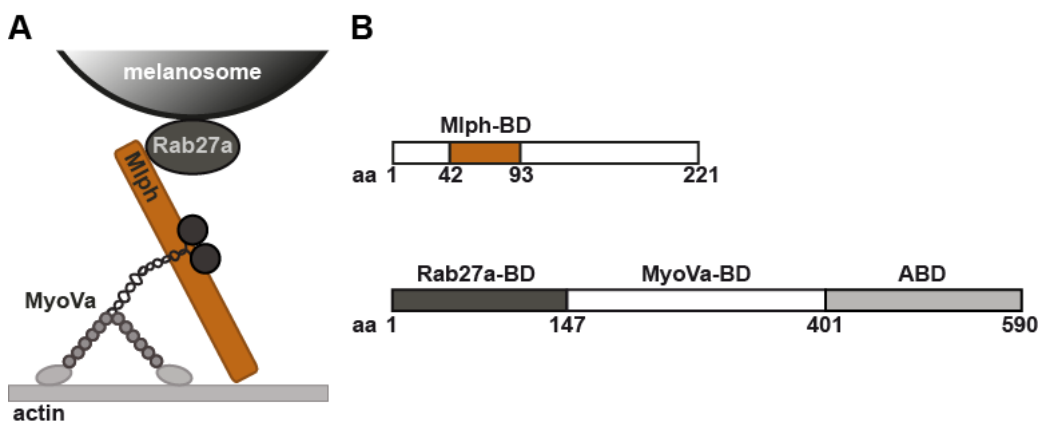
Figure 6: The tripartite MyoVa transport complex on the melanosome surface in mouse melanocytes. The actin-based motor protein MyoVa is recruited to the melanosome via Rab27a and Mlph in mouse melanocytes. (A) Rab27a resides in the melanosome membrane and binds to the adaptor protein Mlph in a GTP-dependent manner. Mlph in turn binds to MyoVa, linking the motor protein to the melanosome surface. (B) Domain structures of Rab27a (top) and Mlph (bottom). Mlph binds to Rab27a's effector-binding domain (Mlph-BD) with its N-terminal Rab27a-BD. MyoVa in turn associates with Mlph's middle domain (MyoVa-BD) with exon F and the GTD domain. Additionally, Mlph contains a C-terminal actin-binding domain (ABD).

Rab27a is a member of the Rab family belonging to the Ras superfamily of small guanosine triphosphatases (GTPases) and resides in the membrane of the melanosome. It inserts into the hydrophobic membrane with two posttranslationally attached C20 geranylgeranyl groups bound to cysteines near the C-terminus. Rab27a is able to bind and hydrolyze GTP with the help of guanine nucleotide exchange factors (GEFs) and guanine nucleotide activating proteins (GAPs), respectively, and exists in two conformational states: the active GTP-bound state that is able to bind to effector proteins, and the inactive GDP-bound state. One effector protein that binds to Rab27a in its active, GTP-bound state is Mlph (or Slac2-a), a member of the synaptotagmin-like protein (Slp) family. The Slp family possesses two conserved domains – SHD1 and SHD2 - at the N-terminus, sometimes interrupted by two zinc-finger motifs. Mlph's SHD (termed Rab27a binding domain, Rab27a-BD in this thesis) directly interacts with the GTP-bound form of Rab27a *in vitro* and *in vivo* (44-46). The middle domain of Mlph (MyoVa binding domain, MyoVa-BD) specifically binds to MyoVa's GTD and exon F, with exon F being essential for this interaction (47). Additionally, Mlph contains a previously described actin-binding domain (ABD) at its C-terminus that was previously reported to interact with F-actin and EB1 (37, 48-50). Therefore, MyoVa is

recruited to the melanosome by the membrane-bound GTPase Rab27a and the adaptor protein Mlph in mouse melanocytes. It remains to be shown whether MyoVa recruitment is accomplished similarly in other organisms like fish or frog.

1.3 <u>Signals governing melanosome transport</u>

The synchronous transport of hundreds of melanosomes by the three motor proteins dynein-1, kinesin-2, and MyoVa to the cell center or the cell periphery requires a tight and fast responsive signal transduction and regulation. Most information on the signaling cascade controlling melanosome transport has been collected in frog or fish melanophores. Previous studies elucidated the involvement of intracellular cyclic adenosine monophosphate (cAMP) levels, protein kinase A or cAMP-dependent kinase (PKA) activity, and phosphorylation and dephosphorylation events in regulation of melanosome transport (8, 9). It is well established that changes in the intracellular cAMP concentration and subsequent activation or inactivation of PKA are the major key players in regulating the melanosome transport direction in frog melanophores. High levels of cAMP accompanied by active PKA induce dispersion, whereas low levels of cAMP and inactive PKA result in aggregation. PKA was shown to be recruited to the melanosome surface in *Xenopus laevis* melanophores by Rab32 (51), implying a role for motor regulation by the key player PKA. Additionally, PKA was found to form complexes with dynein or kinesin-2 and MyoVa (52).

1.3.1   <u>Dispersion</u>

The peptide hormone α-melanocyte-stimulating hormone (α-MSH) produced in the pituitary gland and the hypothalamus stimulates dispersion of melanosomes in frog melanophores. Binding of α-MSH to the Mc1r receptor in the melanophore membrane (53) leads to increased intracellular cAMP levels (54-56), which in turn activate PKA (57, 58). It has been suggested that Ca^{2+} is necessary for the interaction between α-MSH and the receptor (59, 60). Furthermore, PMA, an activator of protein kinase C or calcium-dependent protein kinase (PKC), can partially induce dispersion via a distinct pathway, without elevating intracellular cAMP levels (57). Additionally, an increased activity of the mitogen-activated protein kinase (MAPK) signaling pathway during dispersion in *Xenopus laevis* melanophores was reported (61). The authors speculated it to be a possible indication for the involvement of MAP kinases in coordination of bidirectional melanosome transport (61). Finally, dispersion of melanosomes can be induced by light in *Xenopus*

melanophores. An increase in intracellular IP3 and Ca^{2+} is involved in light-induced dispersion (62).

In this study it will be focused on the α-MSH-induced dispersion via the classical and best studied PKA pathway. This pathway requires phosphorylation events, but also dephosphorylation events occur (57). Taking together all available data so far, the signaling cascade for dispersion involves a high intracellular cAMP concentration and high activity of PKA. In other words, increased PKA activity leads to the transport of melanosomes to the cell periphery achieved by kinesin-2 and MyoVa. Switching from MT filaments to the actin cytoskeleton is an absolute necessity to complete melanosome dispersion. Nevertheless, the target(s) of PKA remain(s) unidentified and it is not known how the signal is further passed on to the motor proteins on the melanosome surface.

In mouse melanocytes, it has been demonstrated that α-MSH induces the rapid transport of melanosomes to the dendrite tips of melanocytes through stimulation of the cAMP pathway (63). The authors suggested involvement of small GTP-binding proteins belonging to the p21Rho family and the effector protein p160 Rho-associated kinase and not PKA to play a key role in redistribution of melanosomes. Further, they postulated that cAMP stimulated the expression of Rab27a and rapidly enhanced the interaction of Mlph with actin filaments. Besides that, no further data is available on signaling cascades governing melanosome transport in mouse melanocytes.

1.3.2   Aggregation

Aggregation in frog melanophores can be induced by the addition of the pineal gland hormone melatonin (64). Melatonin binds the specific high-affinity receptor mel1c (65) and subsequently $G_{i/o}$ proteins are activated, inhibiting adenylyl cyclase and PKA (66). As a consequence, intracellular cAMP levels are decreased in the melanophores (54). An additional melatonin-induced pathway involves mel1c receptor, $G_{\beta\gamma}$ protein-dependent activation of phosphoinositide-3-kinase (PI3-K) and subsequently activation of phosphodiesterase 4 (PDE4), resulting in lowered cAMP levels (67). How the signal is further transduced to the motor proteins on the melanosome to accomplish melanosome aggregation in the cell center is not yet elucidated.

Again as for dispersion, dephosphorylation and phosphorylation events are required for transducing the aggregation signal (57). Using specific phosphatase inhibitors, a role for protein phosphatase 2A (PP2A) in aggregation in *Xenopus* melanophores was discovered (57). Tyrosine-phosphorylation of a 280 kDa protein during aggregation was also demonstrated (68), whose identity is still unknown, but was speculated to be spectrin (68, 69). Moreover, involvement of MEK and MAP kinases is also likely (70). In summary, lowered cAMP levels and subsequent dephosphorylation of unknown targets by PP2A and maybe other phosphatases result in dynein-mediated melanosome transport toward the cell center. Importantly, melanosomes have to be transferred from the actin cytoskeleton back to MTs to allow dynein-mediated transport.

1.4 <u>Regulation of the individual motor proteins to achieve proper melanosome distribution</u>

In vivo, melanosomes show discontinuous, bidirectional movements even when induced to disperse or aggregate. Furthermore, melanosomes often stall and pause before continuing or switching direction on a microtubule (71). Consequently, more than one type of molecular motor on the organelle is active during dispersing or aggregating melanosomes. Therefore, the outcome of the net transport direction is dictated by the motor protein(s) that travels the farthest total distance compared the others (transport toward the cell center versus transport toward the cell margins).

Investigations on motor regulation can be performed using two distinct experimental approaches, amongst others: i) Isolation of melanosomes and performance of *in vitro* motility assays, possibly in the presence of potential regulating substances. ii) Manipulation of one cytoskeletal system (actin filaments or microtubules) or inhibition of one type of motor protein (dynein, kinesin, or myosin) in living cells and observing the effects on transport with *in vivo* tracking of melanosomes. In 1997, Gelfand and coworkers showed that isolated pigment granules retained their regulated states *in vitro* (12), as a first insight into MT-based motor regulation that seems to occur on the melanosome surface. The majority of melanosomes purified from dispersed melanophores moved to the plus-ends of MTs in motility assays *in vitro* (12). Vice versa, melanosomes isolated from aggregated melanophores mostly exhibited minus-end directed movement on MTs *in vitro* (12). The use of dominant negative tail constructs to selectively block either kinesin-2 or MyoVa

activity in *Xenopus* melanophores impaired the cells' ability to properly disperse their pigment granules, demonstrating that the activity of both kinesin-2 and MyoVa is required for pigment dispersion (13, 72). A combination of motor manipulation with dominant negative tail constructs and biophysical characterization of melanosome transport *in vivo* contributed extensively to today's understanding of motor regulation in *Xenopus* melanophores (73). Gross et al. revealed that dynein activity is upregulated during aggregation and downregulated when melanosomes disperse (73). Conversely, MyoVa is downregulated by about 50% during aggregation compared to pigment dispersion, whereas kinesin-2-mediated transport is not changed during aggregation or dispersion (73). Thus, competition between the dynein/MT-and MyoVa/actin-system seems to occur, whose winner determines the transport direction of the organelles. Quantitative immunoblotting indicated identical amounts of cargo-bound kinesin-2 and dynein between dispersed melanosomes versus aggregated melanosomes (73). However, MyoVa showed a ca. 35% decrease on aggregated melanosomes compared to dispersed pigment granules (65 ± 10 per aggregated melanosome on average and 88 ± 7 MyoVa molecules per dispersed melanosome on average) (73). The authors speculated that the observed downregulation of the actin-based motor MyoVa during aggregation is achieved by decreasing the organelle-bound motor number (73). From their observation that dynein velocity is not altered in a kinesin-2-blocked background, they further concluded that there likely is coordination between the two MT-based motors, but a continuous tug-of-war between the actin- and MT-systems that determines the transport direction (73). By downregulating MyoVa and upregulating dynein, pigment granule aggregation is favored. Vice versa, upregulating MyoVa activity and lowering dynein activity set the course for pigment dispersion. Lastly, they hypothesized that switching from MT onto actin filaments primarily occurs during minus-end runs, because minus-end runs are predominantly decreased during dispersion (73). Another *in vivo* tracking study using a novel algorithm by Rodionov and colleagues suggested that, in addition to upregulation of MyoVa, MT-based transport toward the MT plus-ends by kinesin-2 is increased during early dispersion and gradually declines again as dispersion advances (correlating with high cAMP levels at the beginning of dispersion that continuously decline again to reach basal levels at late dispersion) (71). Gelfand and coworkers continued investigating how the MT-based motors on the melanosome are regulated with the means of a novel fast-tracking method *in vivo*

(74). By comparing the velocity distribution of MT-mediated transport during the aggregation and dispersion process, they postulated that only the number of active dyneins changes (74). In contrast, they found the number of active kinesin molecules to be similar between aggregation and dispersion. Therefore, the number of active dynein motors determines the transport direction of a single melanosome on MTs. According to their model, one to three active dynein copies move a pigment granule toward the MT minus-end, whereas one to two kinesin-2 molecules are responsible for the plus-end-directed transport (74).

One candidate for coordinating the MT-based motor proteins kinesin-2 and dynein is the dynactin complex, in particular the largest subunit p150^{Glued}. p150^{Glued} is long known as the adaptor that establishes the direct link between dynein and various cargos via the dynactin complex. Moreover, p150^{Glued} was also demonstrated to interact with kinesin-2 on *Xenopus* melanosomes via the same binding domain on p150^{Glued} utilized by dynein (30). Thus, binding of kinesin-2 and dynein is mutually exclusive. Inhibition of one MT-based motor or the dynactin complex also affects the other MT-based motor in other systems, implying that MT-based transport is likely to be coordinated as observed in several other transport processes (29, 75, 76). In addition, dynein needs the dynactin complex to processively move on MTs (77) and dynactin was also shown to increase the activity of kinesin-2 (78). Dynactin as a shared organelle adaptor for both MT-motors that is additionally capable of modulating both motor's processivities is a promising candidate in coordinating melanosome transport on MT. How this is achieved mechanistically in the cell remains an object of investigation.

During the last 20 years, many advances have been achieved in elucidating regulation of the three motor proteins that power melanosome transport. The common consensus is that dynein activity is higher during aggregation and decreased during dispersion. Furthermore, MyoVa transport is regulated in the opposite manner: higher activity during pigment granule dispersion and lower activity during aggregation. The decision which way to go (aggregation or dispersion) seems to be determined by a tug-of-war between the dynein/MT- and MyoVa/actin-system. Kinesin-2 transport is reported to be relatively constant and might only be temporarily upregulated during early dispersion. Importantly, correct dispersion cannot be accomplished in all organisms if MyoVa activity is impaired

(*Xenopus* and mammals: perinuclear clustering; fish: hyperdispersion); indicating that switching from MTs onto actin filaments is an absolute necessity for the dispersion process. Vice versa, for aggregation of melanosomes, it is absolutely essential that melanosomes are handed from the actin cytoskeleton back to the microtubule system.

1.5 Crosstalk between the actin-based and the MT-based transport systems in melanosome transport

Extensive work on the model system for intracellular transport, transport of melanosomes, established that switching between actin filaments and MTs is an absolute prerequisite for proper intracellular melanosome distribution. This necessitates regulatory mechanisms controlling the switching of melanosomes from one cytoskeletal system to the other. However, information on how crosstalk is achieved mechanistically between the two cytoskeletal systems to bring about the precisely regulated melanosome transport is still very sparse.

Disruption of the actin cytoskeletal system was already sufficient to impair proper dispersion in all pigment cell types, implying that both transport machineries work closely and coordinately together. Several experimental observations point to a coordination between the two MT-based motor proteins without providing a molecular mechanism. A tug-of-war seems to occur between the dynein/MT- and MyoVa/actin-system, where downregulation of one motor helps the other to determine the transport direction. However, only sparse information on the crosstalk between the two cytoskeletal systems is available to date and mechanistic details remain elusive.

Previous *in vitro* work with dynein-dynactin and myosin-V-coated beads showed that the force produced by dynein and myosin-V controls motor switching at actin-MT junctions (79). The force produced by each motor type correlated to the motor number on the beads. By varying the ratio of dynein and myosin-V on the beads, switching of motor-coated beads could be biased to either MTs (if the force produced by dynein was higher) or actin filaments (if the force produced by myosin-V was higher), independent of the entry filament. The authors concluded that a simple mechanical tug-of-war could explain many of the observations. Experiments with kinesin-2- and myosin-V-coated beads suggested that switching frequencies between actin filaments and MTs were dependent on the starting track (80). Twice as many kinesin-2 compared to myosin-V molecules were

required for equal switching probabilities when the starting track was a MT. Identical numbers of kinesin-2 and myosin-V molecules yielded in an equal switching probability when the starting track was an actin filament. The authors propose that, in addition to relative force, the switching probability of kinesin-2- and myosin-V-coated beads at actin-MT intersections is determined by the dynamics of the motor-filament interaction. Higher number of kinesin-2 molecules are needed due to the quick detachment of kinesin-2 under load. Collectively, these two studies provide first valuable information that regulation of cargo switching between MTs and actin filaments is influenced by the number of active motors, however, it is very likely that cells employ additional mechanisms to link the two cytoskeletal transport systems.

Work on fish melanophores by Rodionov and coworkers demonstrated that switching from MTs onto actin filaments is tightly controlled by the intracellular concentration of cAMP (81), implicating that coordination of both cytoskeletal systems is accomplished at least in part by signaling events. The underlying mechanism, however, remains still completely unclear. Employing a combination of *in vivo* particle tracking and computational modeling suggested that switching of filaments is solely determined by changing the switching rate from actin filaments onto MTs in fish melanophores (82). The authors hypothesized that the switching rate from actin filaments to MTs is controlled by modulating motor protein activities (decreasing MyoVa activity and increasing dynein activity) and additionally changing the affinity for one or both cytoskeletal track(s) or a yet unknown mechanism. So far, no experimental evidence has been put forward to explain the molecular mechanism governing this switching rate.

Another study in fish melanophores, specifically on the zebrafish mutant *j120* put forward the adaptor protein Mlph as a potential coordinator between MT- and actin-dependent transport. The mutant *j120* displays defects in dispersion that are caused by a mutation in the Mlph gene (i.e. one of the adaptor proteins linking MyoVa to the melanosome), resulting in a premature stop codon and thus a shortened, nonfunctional Mlph protein (83). The authors further observed that this dispersion defect arises from exceptionally long minus-end runs on MTs and provided evidence that an additional function of Mlph, besides linking MyoVa to the melanosome, is to suppress dynein runs during dispersion. Mechanistic details on this additional function of Mlph implied by this study remain to be

demonstrated. This is the first indication of a direct crosstalk between the two cytoskeletal systems through the adaptor protein Mlph.

It is very likely that the actin- and MT-systems employ further mechanisms for coordination and crosstalk. This thesis was focused on elucidating further details on how the cytoskeletal systems are intertwined to achieve transport of melanosomes to the proper destination within the cell at the correct time.

2. <u>Aims of this thesis</u>

2.1 <u>Reconstitution of the actin-based melanosome transport *in vitro*</u>

Transport of melanosomes in *Xenopus laevis* melanophores served as a model system to study intracellular transport for more than 30 years. Despite the detailed knowledge about the microtubule-based transport system involved in melanosome transport, little is known about the actin-based transport of melanosomes. It was previously shown that MyoVa is the motor responsible for actin-based melanosome transport in *Xenopus laevis* melanophores (15), however, the components of the putative MyoVa receptor complex remain unidentified. Previous reconstitution of actin-based melanosome transport on *Nitella* actin cables *in vitro* exhibited an atypically slow velocity of 40 nm s^{-1} (15).

Even though the involvement of cAMP and PKA in signal transduction in amphibian melanophores is well established, the underlying molecular mechanisms of how PKA activity modulates the transport direction of melanosomes are not yet known.

One major goal of this thesis was to gain insights into the regulation of the actin-based transport of melanosomes in *Xenopus laevis* melanophores. To this end, I aimed to reconstitute melanosome transport on actin filaments instead of *Nitella* actin cables *in vitro* and characterize MyoVa-dependent transport dependent on the respective cell states (i.e. dispersed and aggregated cell state). Additionally, this experimental setup enabled me to directly test the effects of the 'master regulator' (i.e. PKA) on MyoVa-driven transport under defined experimental conditions. Results will shed light onto the mechanisms underlying MyoVa-mediated transport of melanosomes in amphibians.

2.2 <u>Formation of the MyoVa transport complex in the amphibian *Xenopus laevis*</u>

The second aim of this study was to elucidate details on the formation of the MyoVa transport complex on *Xenopus laevis* melanosomes. Despite its essential role in melanosome transport, it is not known how MyoVa is linked to melanosomes in *Xenopus laevis* melanophores. Genetic studies in mouse melanocytes identified the two adaptor proteins Rab27a and Mlph that link MyoVa to the melanosome surface. By recombinant expression of the respective proteins from *Mus musculus* and *Xenopus laevis/tropicalis* and subsequent coexpression, I aimed to assemble the MyoVa transport complex *in vitro*.

Reconstituting the MyoVa transport complex *in vitro* will enable an in-depth mechanistic dissection of MyoVa-driven transport *in vitro*.

2.3 Regulation of the MyoVa transport complex from *Mus musculus in vitro*

Phosphorylation events appear to be a common signal for melanosome transport toward the cell periphery. However, it is not yet known how the signal(s) is/are passed to the motor proteins conducting this transport. The third aim of this thesis was to identify (a) downstream target(s) of phosphorylation by, for example, the prevalent kinase PKA using the recombinantly expressed proteins from Xenopus and mouse.

How is the MyoVa transport complex regulated to switch from the MT network to the actin network to enable efficient dispersion of melanosomes? As previously demonstrated, MyoVa is capable of interacting with MTs and exhibits bidirectional diffusional movement on MTs *in vitro* (84, 85). Does this special property of MyoVa help to switch melanosomes from actin onto MTs in cells? To provide first insights into how cells bias the transport direction of melanosomes, TIRF microscopy assays were employed in this work. I performed filament decoration assays with different complexes on actin and MTs and mixed networks of both filaments to observe the individual and combined binding preferences. Single-molecule TIRF assays with the reconstituted MyoVa transport complex on actin, MTs, and mixed networks will reveal potential mechanisms by which cells regulate the binding preferences toward actin or MTs.

3. <u>Materials</u>

3.1 <u>Cell culture accessories</u>

Name of item	Company, location
Fetal Bovine Serum (FBS) USA origin, sterile-filtered, cell culture- and hybridoma-tested	Sigma-Aldrich, Taufkirchen
Cellfectin® II reagent	Life Technologies, Darmstadt
Insulin from bovine pancreas	Sigma-Aldrich, Taufkirchen
Trypsin/EDTA	PAA, Cölbe
Melatonin	Sigma-Aldrich, Taufkirchen
α-melanocyte stimulating hormone (α-MSH)	Sigma-Aldrich, Taufkirchen
Leibovitz's L-15 medium	Life Technologies, Darmstadt
Penicillin/streptomycin	Life Technologies, Darmstadt
Gentamicin	Bio&Sell, Feucht bei Nürnberg
Sf-900 II SFM medium	Life Technologies, Darmstadt

3.2 <u>Buffers and solutions</u>

All buffers and solutions used in this study were prepared with reagents from Sigma-Aldrich (Taufkirchen) and Carl Roth (Karlsruhe). Compositions are listed in the respective method section.

3.3 <u>Antibodies</u>

	Antibody name	Isotype/host	Company, location
	α-GAPDH	IgG1/mouse	Millipore, Temecula (U.S.A.)
Primary	α-Mlph	IgG/goat	Everest Biotech, Upper Heyford (UK)
	α-MyoVa (clone LF-18), polyclonal	IgG/rabbit	Sigma-Aldrich, Taufkirchen
	α- protein kinase A (PKA) catalytic subunit α/β/γ	IgG/rabbit	Santa Cruz, Heidelberg
	α-Rab27a	IgG/mouse	Benson Dickinson, Heidelberg, Germany
Secondary	Anti-Mouse IgM (μ-chain specific) peroxidase conjugate	IgM/goat	Sigma-Aldrich, Taufkirchen
	Anti-Goat (whole molecule) peroxidase conjugate	IgG/rabbit	Sigma-Aldrich, Taufkirchen
	Anti-Rabbit IgG (whole molecule) peroxidase conjugate	IgG/goat	Sigma-Aldrich, Taufkirchen
	Anti-Mouse IgG (Fc-specific) Peroxidase Conjugate	IgG/ goat	Sigma-Aldrich, Taufkirchen

3.4 <u>Chemicals and ready-to-use solutions</u>

Name	Company, location
Casein from bovine milk, technical grade	Sigma-Aldrich, Taufkirchen

cOmplete Protease Inhibitor cocktail, EDTA-free	Roche, Penzberg
PhosSTOP Phosphatase Inhibitor cocktail	Roche, Penzberg
H-89 dihydrochloride hydrate	Sigma-Aldrich, Taufkirchen
peqGOLD prestained Protein Marker IV	PeqLab, Erlangen
peqGOLD Protein Marker II	PeqLab, Erlangen

3.5 Media

For cell culture media composition refer to respective section in 4. Methods.

3.6 Plasmids and vectors

Description	Distributor, Location
pFastBac™ Dual	Life Technologies, Darmstadt
pFastBac™ 1	Life Technologies, Darmstadt

3.7 Oligonucleotides

3.7.1 Cloning primers

Primer name	Primer sequence	Restriction site
*Xl*Rab27a_Fw	5'-aggctcgagatgtcggatgg-3'	XhoI
*Xl*Rab27a_6XHis_Rv	5'-ggcaaatgcggctgtggcgcgccacaccaccatcaccatcattaaggtaccata-3'	KpnI
*Xt*Mlph-NFLAG-SalI_Fw	5'-acggaagtcgacatggactacaaggacgacgatgacaagggcgcacctgggaagaagctggactt-3'	SalI
*Xt*Mlph-SalI_Fw	5'-acggaagtcgacatggggaagaagctggactt-3'	SalI
*Xt*Mlph-NotI_Rv	5'-cccattgtgaatcagagatgagcggccgcttccgt-3'	NotI
*Xt*Mlph_ABD_del1_Rv	5'-gccagcaacatcagtgacaaaggaggatgagcggccgcttccgt-3'	NotI
*Xt*Mlph_ABD_del2_Rv	5'-ggagcatgcccgtcagagcggttgagcggccgcttccgt-3'	NotI
*Xl*MyoVa_NheI_Fw2	5'-gcgctagcatggaaaacaatttagattttgc-3'	NheI
NheI-FLAG-*Xl*MyoVa_Fw	5'-atagctagcatggactacaaggacgatgacgacaagggcggcgaaaacaatttagattttgc-3'	NheI
*Xl*MyoVa_1110_NheI_FLAG_Fw	5'-atagctagcatggactacaaggacgatgacgacaagggcggcccaggacacaagcgc-3'	NheI
*Xl*MyoVa_m1247_SphI_Rv	5'-gcgcaaggcaatcactgagaaagcttccccatgagcatgcata-3'	SphI
*Xl*MyoVa_SphI_Rv	5'-ggttcctcacacgcgtctgagcatgcaac-3'	SphI
*Mm*Mlph_BamHI_XhoI_FLAG_Fw	5'-aggggatccctcgagatggactacaaagatgacgacgataaaggcggtggaaaaagattggacc-3'	BamHI
*Mm*Mlph_ABD_del1_Rv	5'-gcctggaggaattgacatccaacatcagcggaagttcgacgtaaggtaccaagcttata-3'	HindIII
*Mm*Mlph_ABD_del2_Rv	5'-cgcaaccctcgttcacccggaaacccagctaggccgacaaagtaaggtaccaagcttata-3'	HindIII

***Mm*MyoVa_HMM_Ba mHI_XhoI_FLAG_Fw**	5'-aggggatccctcgagatggattacaaagacgatgatgataaggc ggagcggcttcgg-3'	BamHI XhoI
***Mm*MyoVa_HMM_11 19G_HindIII_KpnI_Rv**	5'-ggaaatgaccttgatgctgaacgtgcctaagcccggctaaggt accaagcttata-3'	KpnI HindIII

3.7.2   Sequencing primers

Primer name	Primer sequence
PH	5'-cctataaatattccggattattcataccg-3'
P10	5'-cggacctttaattcaaccc-3'
***Xt*Mlph_Seq1_Fw**	5'-agtggacaggttggtgaagg-3'
***Xt*Mlph_Seq2_Fw**	ttcaagagcaagggcagaat
***Xt*Mlph_Seq3_Fw**	5'-cggtaccactgactccgaat-3'
***Xl*MyoVa_Fw13**	5'-gccacctgaagcaagaattg-3'
***Xl*MyoVa_Fw16**	5'-ttgttcatgtgtttgcgtca-3'
***Xl*MyoVa_Fw17**	5'-gccattaattcaggctgctc-3'
***Mm*Mlph_Seq1**	5'-gccgagcatgtctgggccgtggtccagaggg-3'
***Mm*Mlph_Seq2**	5'-gccgtcgggcgaggacgcacatgcgg-3'
***Mm*Mlph_Seq3**	5'-gggcggatctcccaaggtctgcacagacacgggcc-3'
***Mm*MyoVa_Seq0**	5'-cggtgtctggttcagcaagtgaagcg-3'
***Mm*MyoVa_Seq1**	5'-gggcaacgctgactcgttccattacactaagcaggg-3'
***Mm*MyoVa_Seq1_1**	5'-gccgtgcatcaacctgattgagagtaagttggg-3'
***Mm*MyoVa_Seq2**	5'-ccccgaattgttccaggacgatgagaaggctatctcgcctac-3'
***Mm*MyoVa_Seq3**	5'-cgcgtgcgtggatggctcgctcgc-3'
***Mm*MyoVa_Seq4**	5'-cgcccctcgcacggaggaaccc-3'

3.8 Microorganisms

Cell strain	Company
MAX Efficiency® DH10Bac^{TM} Competent *E. coli*	Life Technologies, Darmstadt
XL1-Blue Subcloning-Grade Competent Cell	Stratagene, La Jolla (U.S.A.)

3.9 Media and agars for microorganisms

For bacteria media composition refer to respective sections in 4. Methods.

3.10   Enzymes and kits for biochemistry and molecular biology

Name of item	Company, location
Antarctic Phosphatase (Kit)	New England Biolabs, Frankfurt a. Main
Bac-to-Bac® Baculovirus Expression System	Life Technologies, Darmstadt
Platinum® Pfx Polymerase (Kit)	Life Technologies, Darmstadt
T4 Ligase (Kit)	New England Biolabs, Frankfurt a. Main
QiaPrep® Miniprep Kit	Qiagen, Hilden
Restriction enzymes	New England Biolabs, Frankfurt a. Main

Protein Kinase A Catalytic Subunit from bovine heart (PKA)	Sigma-Aldrich, Taufkirchen
cAMP-dependent Protein Kinase A (PKA), catalytic subunit	New England Biolabs, Frankfurt a. Main
Protein Phosphatase 2A C subunit (human recombinant; L309 deletion)	Cayman Chemical, Ann Arbor (U.S.A.)
SNAP-Surface® Alexa Fluor® 488	New England Biolabs, Frankfurt a. Main
SNAP-Surface® Alexa Fluor® 647	New England Biolabs, Frankfurt a. Main

3.11   Software for data acquisition and analysis

Software	Company, location
Igor Pro Version 6.12	WaveMetrics Inc., Portland (U.S.A.)
ImageJ Versions 1.44p and 1.50i	NIH, Bethesda (U.S.A.)
ImageJ plugin ParticleTracker 2D/3D	NIH, Bethesda (U.S.A.)
ImageJ macro MultipleKymograph	NIH, Bethesda (U.S.A.)
MATLAB R2016b	The MathWorks, Natick (U.S.A.)
OriginPro 9.1G 64-bit	OriginLab, Northampton (U.S.A.)

4. <u>Methods</u>

4.1 <u>Cell culture</u>

4.1.1   <u>Cell culture of immortalized *Xenopus laevis* melanophores</u>
Immortalized *Xenopus laevis* melanophores (gift of Vladmimir I. Gelfand, Northwestern University, Chicago, U.S.A.) were cultured at 28 °C in melanophore medium as previously described (11). Depending on the amount of melanosomes needed, cells were grown in 25 cm^2, 75 cm^2, or 175 cm^2 sterile tissue culture-treated flasks. Usually cells were grown to confluency and split by trypsinization once a week.

Cells were transferred into serum-free medium 24 hours prior to hormone stimulation. One hour prior purification, aggregation or dispersion of pigment granules was stimulated by adding 50 nM Melatonin or 100 nM α-melanocyte stimulating hormone to the serum-free culture medium, respectively.

For long-term storage and subsequent thawing, freeze cultures of melanophores were prepared. To this end, a confluently grown 75 cm^2 culture flask was trypsinized and melanophores were resuspended in 30 ml 0.7X L-15 medium. Cell suspension was transferred into two sterile 50 ml Falcon tubes and centrifuged at room temperature for 15 minutes at 150X g. After discarding the supernatant, cells were gently resuspended in 3 ml melanophore freeze medium I and incubated on ice for five minutes. 3 ml of melanophore freeze medium II were added dropwise under constant shaking to the chilled cell suspension. The mixture was cooled on ice for 15 minutes before transferring 1 ml each into sterile cryo vials. Vials were placed into a box with absorbent cotton and frozen for three to four hours at -80 °C. Finally, cryo vials were placed in a liquid nitrogen tank for long-term storage.

To start a new melanophore culture, one vial was taken out of the liquid nitrogen tank and quickly thawed in a 37 °C water bath. Cell suspension was transferred into a sterile 15 ml Falcon tube and 5 ml of warm melanophore medium was slowly added. After centrifuging at room temperature for five minutes at 500X g, cells were gently resuspended in 10 ml warm melanophore medium and seeded in a 25 cm^2 tissue culture flask. To remove melanophores that did not survive freezing and thawing procedure, melanophore medium was exchanged after two to three days after incubation at 28 °C.

Melanophore medium: 0.7X L-15 medium, 10% fetal bovine serum, 5 μg/ml insulin, 100 U/ml penicillin and streptomycin

Trypsin in 0.7X PBS: 0.05% Trypsin/EDTA, 0.7X PBS

Melanophore freeze medium I: 0.7X L-15 medium, 40% FBS

Melanophore freeze medium II: 0.7X L-15 medium, 50% FBS, 20% DMSO

4.1.2   <u>Cell culture of Sf9 insect cells</u>
The Sf9 insect cell line (Life Technologies) was used to recombinantly express proteins with the baculovirus system (Life Technologies). This cell line is a clonal isolate derived from the parental

Spodoptera frugiperda (fall armyworm) cell line IPLB-Sf-21-AE (86-88), which originated from a population of cells that was isolated from *S. frugiperda* ovarian tissue.

Sf9 cells were suspension-cultured in Sf-900 II SFM medium supplemented with 10% FBS and 0.5 mg/ml Gentamicin at 28 °C and 110 rpm in Erlenmeyer flasks. The cultures typically had a volume from 50 to 500 ml and a cell density of 0.5 to $8X10^6$ cells/ml. Cells were diluted every other day with fresh supplemented medium. For protein expression, cells were diluted to a density of $2X10^6$ cells/ml before adding virus(es), whereas cells were brought to a density of $0.5X10^6$ for the purpose of amplifying a virus generation.

In general, cells were propagated up to 30 passages. To start a new round of Sf9 propagation, liquid nitrogen-stored cell stocks were thawed and expanded according to the manufacturer's protocol. Aliquots of cells to be stored in liquid nitrogen were prepared and handled as described by the manufacturer.

Sf-900 II SFM medium (supplemented): Sf-900 II SFM medium, 10% FBS, 0.5 mg/ml Gentamicin

4.2 Molecular biological methods
Standard molecular biological methods were mainly performed as described in (89).

4.2.1   DNA

4.2.1.1 Constructs generated by PCR or by restriction enzyme-mediated cloning
All constructs were placed inside the appropriate vector by restriction enzyme-mediated cloning. All restriction sites employed in this work are summarized for each construct in Table I.

Table I: Used restriction sites for cloning of constructs into pfastBac1.

Construct name	5' restriction site	3' restriction site
*Xl*Rab27a constructs	XhoI	KpnI
*Xt*Mlph constructs	SalI	NotI
*Xl*MyoVa constructs	NheI	NotI
*Mm*Rab27a constructs	XhoI	KpnI
*Mm*Mlph constructs	XhoI	KpnI
*Mm*MyoVa constructs	XhoI	KpnI

C-terminally 6XHis-tagged (6XHistidin-tag, Qiagen) *Xl*Rab27a was generated by PCR with the primers *Xl*Rab27a_Fw and *Xl*Rab27a_6XHis_Rv (for sequences refer to section 3.7.1 Cloning primers).The C-terminal SNAP-tag (New England Biolabs) was introduced into the constitutively active *Xl*Rab27a-Q78L using the restriction sites AscI and KpnI.

Mlph DNA from *Xenopus tropicalis* (accession number NM_001126722.1) was a kind gift of Vladimir I. Gelfand (Northwestern University, Chicago, U.S.A.). An N-terminal FLAG-tag (Sigma-Aldrich) was introduced into the Mlph gene using the PCR primers *Xt*Mlph_NFLAG-SalI_Fw and *Xt*Mlph-NotI-Rv. An untagged Mlph was cloned using the primers *Xt*Mlph-SalI_Fw and *Xt*Mlph-NotI_Rv. PCR of untagged and N-terminally FLAG-tagged *Xt*Mlph was performed by Dennis Zimmermann. C-terminally truncated Mlph constructs with an N-terminal FLAG-tag were generated using the primers *Xt*Mlph_NFLAG-SalI_Fw and *Xt*Mlph_ABD_del1_Rv or *Xt*Mlph_ABD_del2_Rv, respectively.

X. laevis MyoVa sequence was cloned from cDNA from immortalized *X. laevis* melanophores (accession number JX494698.1) via RACE-PCR by Dennis Zimmermann (90). The N-terminally FLAG-tagged *Xl*MyoVa construct was generated using the primer pair NheI_FLAG_*Xl*MyoVa_Fw and *Xl*MyoVa_SphI_Rv (90). The untagged *Xl*MyoVa construct was obtained by PCR with the primers *Xl*MyoVa_NheI_Fw2 and *Xl*MyoVa_SphI_Rv (90). The *Xl*MyoVa-HMM construct (1-1237) was generated using the primers NheI-FLAG_*Xl*MyoVa_Fw and *Xl*MyoVa_m1247_SphI_Rv, whereas the C-terminal truncation construct *Xl*MyoVa C-tail (1110-1852) was obtained by PCR with the primer pair *Xl*MyoVa_1110_NheI_FLAG_Fw and *Xl*MyoVa_SphI_Rv. *Drosophila melanogaster* calmodulin (gift of James A. Spudich, Stanford University, Stanford, U.S.A.) was always coexpressed with MyoVa constructs for motor functionality.

The C-terminally truncated *Mm*Mlph constructs with an N-terminal FLAG-tag were obtained by PCR with the primer pairs *Mm*Mlph_BamHI_XhoI_FLAG_Fw and *Mm*Mlph_ABD_del1_Rv or *Mm*Mlph_ABD_del2_Rv, respectively.

The N-terminal truncation construct of *Mm*MyoVa (1-1109) was generated with the primers *Mm*MyoVa_HMM_BamHI_XhoI_FLAG_Fw and *Mm*MyoVa_HMM_1119G_HindIII_KpnI_Rv.

4.2.1.2 Polymerase chain reaction (PCR)

To generate truncated or modified constructs, PCRs were performed with specifically designed oligonucleotides (primers) to amplify the template DNA. The respective DNA template was mixed with the forward and reverse primer, DNA polymerase, deoxyribose nucleoside triphosphates (dNTPs), and the appropriate reaction buffer and objected to a thermal cycle to amplify the desired DNA part. The PCR cycle starts with heat-denaturation of the double-stranded DNA, is followed by hybridization of the single strands and added primers, and is completed by the eventual synthesis of the complementary strand via DNA polymerase. Repeating this cycle 35 times yields in a large amount of the specific DNA fragment.

Reactions were performed as outlined in Table II using Pfx DNA Polymerase, together with the desired combination of forward and reverse primer and previously purified template DNA. The applied PCR program is shown in Table III.

Table II: PCR setup for reactions with Pfx Polymerase.

Component (concentration)	Final concentration	Applied volume (µl)
Reaction buffer 10X	1X	5
Template DNA (200-300 ng)	-	1
dNTP-mix (10 mM)	0.4 mM	2
Forward primer (10 µM)	0.5 µM	2.5
Reverse primer (10 µM)	0.5 µM	2.5
Platinum Pfx Pol (250 U)	2.5 U	1
Sterile H$_2$O	-	Δ 50
Total reaction volume		50

Table III: Thermal cycle for PCR with Pfx Polymerase.

	Temperature (°C)	Cycle Time (s)	Cycles
Denaturation	94	120	
	94	15	35
Annealing	55	45	35
Elongation	68	180	35
	68	420	

4.2.1.3 DNA fragment analysis by agarose gel electrophoresis

The expected size of the amplified DNA fragments was verified by agarose gel electrophoresis. To this end, agarose (1%) and ethidium bromide (1%) were dissolved in TAE buffer. Ethidium bromide intercalates into DNA and makes the fragments visible under ultraviolet light. Samples were mixed with 6X DNA loading buffer prior to applying them on the gel. Gels were usually run at 50 to 90 volts for 30 to 60 minutes. 1 kb DNA ladder was used to determine the sizes of the amplified DNA fragments. DNA bands were detected by a UV light source.

TAE buffer (50X): 24.2% (w/v) Tris Base, 5.7% (v/v) Glacial acetic acid, 50 mM EDTA pH 7.0

DNA loading buffer: 20% Glycerol, 0.1 M EDTA, 1% SDS, 0.25% Bromophenol Blue

4.2.1.4 Gel extraction of DNA fragments

Subsequent to electrophoresis, restriction-digested DNA fragments were excised with a clean scalpel and DNA was purified using the Qiaquick® Gel Extraction Kit (Qiagen) to remove enzyme, template and dNTPs. Typically, purified DNA was eluted in 30 to 50 µl elution buffer. Samples were then stored at -20 °C until further usage.

Elution buffer: 10 mM Tris Base pH 8.0, 1 mM EDTA

4.2.1.5 Purification of PCR products and plasmids

PCR products and amplified plasmids were purified using the Qiaquick® PCR Purification Kit (Qiagen) according to the manufacturer's instruction. Purified DNA was eluted from the column with 30 µl elution buffer and samples were stored at -20 °C.

Elution buffer: 10 mM Tris Base pH 8.0, 1 mM EDTA

4.2.1.6 DNA sequencing

All plasmids and PCR products were purified before sequencing at the Sequencing Service Unit of the Ludwig-Maximilians-Universität (München). 50 to 200 ng of PCR product or 150 to 300 ng plasmid DNA was mixed with 3.3 pmol sequencing primer in elution buffer. Sequencing at the service unit was performed with the "Cycle, Clean & Run" program using BigDye v3.1.

Sequencing was partly performed by MWG Eurofins (Ebersberg). 50 to 100 ng/µl purified DNA were mixed with 15 pmol sequencing primer in a total volume of 15 µl H_2O. Sequencing at the company was performed using the Single Read Service.

Elution buffer: 10 mM Tris Base pH 8.0, 1 mM EDTA

4.2.1.7 Determination of DNA concentration

The concentration of purified DNA was measured spectroscopically by determining the optical density at 260 nm. DNA was diluted 1:100 or 1:200 in H_2O and measured against H_2O. DNA concentration of the sample was calculated using the following equations:

1:100 dilution: $(OD_{260\,nm}$ x 10)/2 = µg DNA/µl

1:200 dilution: $OD_{260\,nm}$/2 = µg DNA/µl

4.2.1.8 DNA sequence synthesis of Rab27a, Mlph, and MyoVa constructs

The majority of constructs used in this study was synthesized by GenScript (Piscataway, U.S.A.) employing the OptimumGene™codon optimization technology to increase protein yields in insect cells. To this end, the OptimumGene™ algorithm was used that alters the bases in the DNA sequence without changing the amino acid sequence.

*Xl*Rab27a DNA was synthesized using the GenBank sequence NM_001092394.1 with a C-terminal FLAG-tag. Constitutively inactive and active forms of FLAG-tagged *Xl*Rab27a were created by substituting the threonine at position 23 with an asparagine (*Xl*Rab27a-T23N) and exchanging the glutamine at position 78 with a leucine (*Xl*Rab27a-Q78L), respectively (46). Furthermore, *Xl*MyoVa GTD (1445-1852) was synthesized with an N-terminal FLAG-tag and the molecular leucine zipper GCN4 to ensure dimerization.

*Mm*Rab27a (accession number NM_023635.4) and *Mm*Rab27a-Q78L with a C-terminal SNAP-tag followed by a 6XHis-tag, *Mm*Mlph (accession number NM_053015.2) with N-terminal FLAG-tag, and *Mm*MyoVa (accession number NM_010864.1) with N-terminal FLAG-tag were synthesized as well. Four point mutated and N-terminally FLAG-tagged *Mm*Mlph constructs, mimicking the dephosphorylated state by substituting serine or threonine with alanine residues, were prepared by GenScript. Following point mutants were generated: *Mm*Mlph T443A/S445A/T446A, *Mm*Mlph S491/498A, *Mm*Mlph S544/546/547A, and *Mm*Mlph Dephos control mutant T392A/S393/396/398/399A/T400A/S401A.

4.2.2 Cloning techniques

4.2.2.1 Restriction enzyme-mediated DNA digest

All constructs have been cloned using two different restriction sites engineered at their 5' and 3' ends and digested with the respective restriction enzymes according to the manufacturer's guidelines. Double digests were performed whenever possible, sequential digest was carried out when no buffer suitable for both enzymes was available. 5 µg DNA were employed for digesting vectors.

4.2.2.2 Dephosphorylation of linearized DNA

Religation was prevented by dephosphorylation of the digested 5' vector end. For this, the vector was incubated with Antarctic Phosphatase for 1 hour at 37 °C following the manufacturer's recommendation. After dephosphorylation, the phosphatase was heat inactivated for 5 minutes at 70 °C.

4.2.2.3 Ligation of DNA fragments into linearized vector

T4 DNA Ligase was employed to fuse the insert with the respective vector. Ligation reaction was carried out for 16 to 72 hours at 16 °C in the provided T4 Ligase buffer.

4.2.2.4 Transformation of chemically competent *E. coli* XL1-Blue cells

Ligated vector and insert were gently mixed with 200 µl slowly thawed *E. coli* XL1-Blue cells and incubated on ice for 5 minutes. Cells were heat shocked for 1 minute at 42 °C, immediately put back on ice and incubated for 2 minutes. 200 µl S.O.C. medium was added to the transformed cells and incubated in a thermo mixer at 37 °C and 900 rpm for one hour. Cells were plated onto a LB agar plate supplemented with selection antibiotic and incubated at 37 °C for approximately 18 hours.

S.O.C. medium: 2% (w/v) Tryptone, 0.5% (w/v) Yeast extract, 10 mM NaCl, 2.5 mM KCl, 10 mM MgCl$_2$, 10 mM MgSO$_4$, 2% (v/v) 1 M Glucose

LB-Ampicillin agar: 1.5% (w/v) Agar, 1% (w/v) Tryptone, 0.5% (w/v) Yeast extract, 1% (w/v) NaCl, 0.1% (v/v) Ampicillin solution (100 mg/ml)

4.2.2.5 Selection and expansion of transformed *E. coli*

Growth on LB agar plates with ampicillin only allows growth of those cells that incorporated the plasmid-DNA containing the ampicillin-resistance cassette (pFastBac1 and pFastBacDual vectors). Transformed *E. coli* were incubated overnight at 37 °C in an incubator. Four to six colonies were picked and two to four ml LB-Ampicillin medium were inoculated with a single colony each for Mini-plasmid preparation (Mini-Prep). Shaking cultures were incubated overnight at 37 °C and 210 rpm in a shaking incubator device.

LB-Ampicillin medium: 1% (w/v) Tryptone, 0.5% (w/v) Yeast extract, 1% (w/v) NaCl, 0.1% (v/v) Ampicillin solution (100 mg/ml)

4.2.2.6 Plasmid-DNA extraction from transformed bacteria

Overnight shaking cultures were transferred into 2 ml reaction tubes and cells were pelleted by centrifugation at 14.000 rpm for one minute in a tabletop centrifuge. Supernatant was discarded and DNA was extracted using the QIAprep Spin Miniprep Kit (Qiagen) and corresponding buffers. DNA was eluted with typically 50 µl pre-warmed elution buffer.

Elution buffer: 10 mM Tris Base pH 8.0, 1 mM EDTA

4.3 Protein biochemistry

4.3.1 Analytical methods

4.3.1.1 Protein analysis by SDS-polyacryl amide gel electrophoresis (SDS-PAGE)

This technique is employed to separate proteins according to their mass. SDS is an anionic detergent which denatures secondary and non-disulfide-linked tertiary structures, and applies a negative charge to each protein in proportion to its mass. In an electric field, the negatively charged proteins move to the positive charged electrode.

In this thesis, gels containing 10% or 12% acrylamide were used. First the resolving gel mixture was prepared and filled in the gel chamber (Bio-Rad). About 1.5 cm of the gel chamber were left for the stacking gel. To get a straight etch of the resolving gel, isopropyl alcohol was layered on top of the liquid resolving gel. After polymerization, the isopropyl alcohol was discarded and the stacking gel mixture was filled into the chamber. The protein samples, usually 5 to 30 µl, were mixed with 1 to 6 µl SDS loading buffer (6X) and incubated at 95 °C for five minutes. The samples, along with protein marker, were carefully loaded into the pockets of the gel. To analyze the size of the respective

proteins, electrophoresis was performed at about 20 to 80 mA for 40 to 60 minutes. The gel was either stained with Coomassie Brilliant Blue or used for immunoblotting.

The gels were put in Coomassie Brilliant Blue solution and heated for 15 seconds in a microwave. Staining occurred for 20 to 60 minutes under constant shaking at 60 rpm. Coomassie Brilliant Blue solution was exchanged with destain buffer and heated for 15 seconds in a microwave. After 20 minutes of shaking at 60 rpm, the destain buffer was replaced with fresh destain buffer and incubated for another 20 minutes. Destained gels were stored in H_2O and digitalized.

Separating gel (10%, 10 ml): 3.3 ml Rotiphorese Gel 30, 2.5 ml Separating gel buffer, 4.2 ml H_2O, 10 μl Temed, 100 μl APS

Separating gel buffer (10X): 0.5 M Tris Base pH 6.8, 0.4% (w/v) SDS

APS solution (100X): 10% (w/v) APS in H_2O

Stacking gel (10%, 10 ml): 1.3 ml Rotiphorese Gel 30, 2.5 ml Stacking gel buffer, 6.2 ml H_2O, 10 μl Temed, 100 μl APS

Stacking gel buffer (10X): 1.5 M Tris Base pH 8.8, 0.4% (w/v) SDS

Electrophoresis buffer (10X, pH 8.8): 3% (w/v) Tris Base, 1% (w/v) SDS, 14% (w/v) Glycine

SDS protein sample buffer (6X): 300 mM Tris Base pH 6.8, 15 mM EDTA, 12% (w/v) SDS, 30% (v/v) Glycerol, 0.06% (v/v) Bromphenol Blue, 15% (v/v) β-Mercaptoethanol

Coomassie Brilliant Blue solution: 0.25% (w/v) Brilliant Blue R-250, 50% (v/v) Methanol, 10% (v/v) Glacial acetic acid

Destain solution: 10% Glacial acetic acid, 25% Isopropyl alcohol

4.3.1.2 Determination of protein concentration

To determine the protein concentration of purified proteins Bovine Serum Albumin (BSA) standards were run on the SDS-PAGE with the protein(s) of interest. Four different concentrations of BSA (0.1; 0.2; 0.3, and 0.4 mg/ml) were used to generate a calibration curve. To this end, the Coomassie-stained gel was digitalized and the band intensities were measured using the ImageJ software (91). The protein concentrations were calculated by measuring the respective band intensity and employing the BSA calibration curve.

4.3.1.3 Western blot analysis

Following gel electrophoresis, proteins were transferred onto a nitrocellulose membrane (Protran-Whatman, Dassel, Germany) using a semi-dry transfer apparatus (PeqLab, Erlangen, Germany). Blots were blocked for 3 hours with milk powder (5%, in TBST buffer). Incubation with primary and secondary antibodies was performed overnight at 4 °C and at room temperature for 1 h, respectively.

Primary antibodies used were as follows: anti-GAPDH, anti-protein kinase A (PKA) catalytic subunit α/β/γ, anti-MyoVa, anti-Mlph, α-Rab27a. Secondary antibodies (all horseradish-peroxidase-conjugated) used were the following: anti-mouse polyclonal IgG (fc-specific), anti-rabbit polyclonal IgG (whole molecule), anti-goat IgG (whole molecule).

Blotting buffer: 24 mM Tris, 192 mM Glycin, 0.02% SDS, 20% Methanol

TBS buffer: 20 mM Tris pH 7.4, 150 mM NaCl

TBST buffer: 20 mM Tris pH 7.4, 150 mM NaCl, 0.05% (v/v) Tween-20

Solution A (ECL) (200 ml): 100 mM Tris-HCl pH 8.6, 50 mg Luminol

Solution B (ECL) (10 ml): 11 mg Coumaric acid in DMSO

ECL solution (4.4 ml): 4 ml solution A (ECL), 0.4 ml solution B (ECL), 1.2 µl H_2O_2 (30%)

4.3.2 Isolation, purification and handling of cytoskeletal proteins

4.3.2.1 G-actin purification from rabbit muscle tissue
Actin from rabbit skeletal muscle was extracted from an acetone powder as described (92). The back and upper thigh muscles of a rabbit were chilled, ground twice and, to remove myosins, extracted with high-salt extraction buffer for 10-15 minutes on a stirrer. The mixture was centrifuged (4 000X g, 4 °C, 10 minutes) and re-extracted. The pellet was then stirred in cold distilled water for 10 minutes and subsequently centrifuged as before with repeats until swelling of the sediment was observed. The pellet was incubated with cold acetone for about 30 minutes, filtered and dried overnight. The acetone powder was stored at -20 °C for subsequent actin preparations.

Usually, 10 g acetone powder were extracted with 200 ml G-buffer plus 0.2 mM ATP at 4 °C for 30 minutes, filtered through nylon nets and re-extracted for 15 minutes. The filtrate was centrifuged (30 000X g, 30 minutes, 4 °C), actin polymerization was promoted by the addition of 50 mM KCl, 2 mM $MgCl_2$ and 1 mM ATP dissolved in 100 mM NaOH and the mixture was incubated at 4 °C for two hours or overnight. To remove tropomyosin, solid KCl was slowly added until a final concentration of 0.8 M was reached. Filamentous actin was subsequently pelleted by centrifugation (150 000X g, 3 hours, 4 °C), the supernatant was discarded and the pellet was homogenized in G-buffer with a douncer. For actin depolymerization, the homogenized F-actin pellet was dialyzed against G-buffer for 2-3 days with a total of about 6 buffer changes.

The solution was centrifuged at 150 000X g and 4 °C for 3 hours, and about 65% from the top supernatant were further purified using a Sephacryl S300 gel filtration column (2.5 x 45 cm, Pharmacia). Fractions were collected and the actin concentrations determined by measuring the optical density at 290 nm (1 mg/ml pure actin: OD_{290nm}=0.65) (93) and their quality tested in a falling ball viscometry assay. The prepared G-actin could be stored on ice for up to 3 weeks for most applications and was dialyzed against fresh G-buffer before usage.

High-salt extraction buffer: 0.5 M KCl, 0.1 M K_2HPO_4

G-buffer: 2 mM Tris HCl pH 8.0, 0.2 mM $CaCl_2$, 0.5 mM DTT, 0.01% NaN_3

4.3.2.2 G-actin polymerization
For the preparation of fluorescent actin filaments, 5 µM of purified G-actin (gift of Michael Schleicher, Ludwig-Maximilians-Universität, and Andreas Bausch, Technische Universität München) was polymerized in assay buffer (AB) (zero ATP) for 1 h at room temperature in the presence of 5 µM Atto488-phalloidin.

AB: 25mM Imidazole pH 7.5, 25mM KCl, 1mM EGTA, 4mM $MgCl_2$, 10 mM DTT, 1 mM ATP, protease inhibitor cocktail

4.3.2.3 Tubulin purification from porcine brain tissue

Tubulin was purified as described previously (94). Briefly, meninges, connective tissue and veins of at least 10 porcine brains were quickly removed in the cold room. 700 g of brain material were mixed with one volume of buffer A and homogenized in a mixer. The homogenate was centrifuged at 13 000 rpm at 4 °C for 70 minutes. The supernatant was collected in a graduated cylinder and the volume was measured. ¼ volume glycerol and 2 mM ATP was added to the supernatant. The suspension was kept at 35 °C for 30 minutes to polymerize the tubulin. Polymerized MTs were centrifuged at 42 000 rpm and 35 °C for 45 minutes. Afterwards, a centrifugation step at 35 000 rpm and 32 °C for 50 minutes was performed. Pellets were resuspended in buffer C. Pellets were homogenized on ice and MTs were depolymerized for 25 minutes on ice. Homogenate was centrifuged at 36 000 rpm and 4 °C for 30 minutes. Supernatant was collected in a graduated cylinder and 2 mM ATP was added. For polymerization, the suspension was kept at 35 °C for 30 minutes. MTs were sedimented by centrifugation at 35 000 rpm at 35 °C for 40 minutes. Supernatant was discarded and pellet was resuspended in buffer B and transferred in a homogenizer. Suspension was homogenized and kept on ice for 25 minutes to depolymerize MTs and occasionally homogenized. Tubulin was centrifuged at 36 000 rpm and 4 °C for 25 minutes. The volume of the supernatant was measured and 1/10 volume DMSO and 2 mM ATP was added. For polymerization of tubulin, the suspension was kept at 35 °C for 30 minutes. Polymerized MTs were pelleted at 33 000 rpm at 35 °C for 40 minutes. Supernatant was discarded and pellet was resuspended in buffer D and transferred into a homogenizer on ice. To depolymerize filaments, the suspension was homogenized on ice for 30 minutes. Precipitates were removed by centrifugation at 34 000 rpm at 4 °C for 30 minutes. Supernatant was transferred onto an equilibrated phosphocellulose (P-11) column to separate tubulin from microtubule-associated proteins (MAPs). Tubulin was eluted with buffer B and main fractions were united. 0.1 M GTP was added to purified tubulin and aliquots were frozen in liquid nitrogen and stored at -80 °C.

Buffer A: 100 mM Pipes pH 6.8, 2 mM EGTA, 1 mM $MgSO_4$, 1 mM DTT, 0.1 mM ATP

Buffer B: 500 mM Pipes pH 6.8, 2 mM EGTA, 1 mM $MgSO_4$, 1 mM DTT, 1 mM ATP

Buffer C: 100 mM Pipes pH 6.8, 1 mM EGTA, 1 mM $MgSO_4$, 1 mM DTT, 1 mM ATP

Buffer D: 100 mM Pipes pH 6.8, 1 mM EGTA, 1 mM $MgSO_4$, 0.05 mM ATP, 0.022 mM GTP, 1 mM DTT

4.3.2.4 Tubulin polymerization

Biotinylated and Atto488-labeled tubulin was polymerized in BRB80 buffer supplemented with 1 mM GTP. To stabilize filaments, 5 µM taxol were added after 30 minutes of incubation at 35 °C. Polymerization was continued overnight at 35 °C. Prior to use, MTs were diluted with BRB80/TX and stored at 35 °C at all times.

BRB80/TX: 80 mM Pipes pH 6.9, 2 mM $MgCl_2$, 1 mM EGTA, 5 mM DTT, 5 µM taxol

4.3.3   Isolation of melanosomes

Melanosome purification from aggregated or dispersed melanophores was performed as described previously (12, 52) in AB, supplemented with cOmplete EDTA-free protease inhibitor. Aggregation or dispersion of hormone-stimulated melanophores was checked and flasks were flushed with 5 ml 0.7X PBS (per 175 cm^2 flask), followed by 5 ml 1X AB without ATP, DTT, and protease inhibitors. Cells were scraped into 2 ml supplemented AB and transferred into 2 ml reaction tubes. Melanophores were lyzed in AB with the so-called Balch-Homogenizer using a tungsten ball with 6 µm clearance and 20 passages. Lysate was transferred into a 15 ml falcon tube and cell debris was pelleted at 750X g for 7 minutes at 4 °C. The supernatant was centrifuged at 2 500X g for 7 minutes at 4 °C to pellet melanosomes. Supernatant was discarded and pigment granules were then resuspended in 50 to 100 µl of AB with supplements.

In experiments with the PKA catalytic subunit from bovine heart and/or H-89 dihydrochloride hydrate, PKA and H-89 was present during the purification at 74 nM and 40 µM, respectively. AB was additionally supplemented with PhosSTOP phosphatase inhibitor cocktail when PKA was present.

In experiments with the cytoplasmic extract from either dispersed or aggregated cells, the respective supernatant after the second centrifugation step was added to the purified melanosomes. Prior to mixing the cytoplasmic extract with purified melanosomes, deprivation of storage buffer was performed by pelleting the pigment granules for 3 minutes at 1 500X g and 4 °C. Melanosomes were then gently resuspended in cytoplasmic extract from the respective cell state.

For immunoblotting, melanosomes were purified as described above, resuspended in a suitable volume of AB and run on a 10% SDS-PAGE.

PBS buffer (1X): 137 mM NaCl, 7.9 mM Na_2HPO_4 X 2 H_2O, 2.7 mM KCl, 1.5 mM KH_2PO_4

AB: 25mM Imidazole pH 7.5, 25mM KCl, 1mM EGTA, 4mM $MgCl_2$, 10 mM DTT, 1 mM ATP, protease inhibitor cocktail

4.3.4   Protein expression using the baculovirus expression system

The baculovirus expression system was used for protein expression in this thesis. Examination of proteins relies on the quality of expressed proteins. Especially for motor proteins, proper folding and posttranslational modifications are essential for functionality. Furthermore, the baculovirus system provides high expression levels and mostly soluble proteins that can be easily purified from insect cells. Lastly, the system is safe to work with because only a small range of invertebrates serve as hosts.

4.3.4.1   Generation of the recombinant transfer vector for protein expression

As described in section 4.2.2 Cloning techniques, the gene of interest was cloned into a pFastBac^{TM} donor plasmid (in this study: pFastBac^{TM}1 and pFastBac^{TM} Dual). This donor plasmid was transformed into *Escherichia coli* MAX Efficiency®DH10Bac^{TM} cells to produce the baculovirus shuttle vector (bacmid) used for transfection of insect cells, virus generation and subsequent protein expression. The *E. coli* DH10 Bac^{TM} cells contain a helper plasmid that encodes a transposase and has a tetracycline-resistance. The mini-Tn7 element from the pFastBac^{TM} donor plasmid is site-specifically transposed to the mini-attTn7 attachment site on the bacmid, introducing the gene of interest into the viral genome and disrupting the lacZα gene. Cells with successfully transposed

bacmids will be white, in contrast to non-transposed cells that grow blue on blue-white-selection agar plates.

DH10Bac^{TM} competent cells were thawed on ice. Approximately 500 ng of recombinant donor plasmid was added to the thawed cells and gently mixed. The mixture was kept on ice for 20 minutes followed by a heat shock for one minute at 42 °C. Afterwards, cells were cooled on ice for two minutes. 800 µl S.O.C.-medium was gently added to cell suspension and cells were allowed to grow at 37 °C for four hours at 225 rpm. Different amounts of cell suspension (50, 15, and 1.5 µl) were plated on freshly prepared blue-white plates and incubated at 37 °C for two to three days. White colonies were restriked onto new blue-white plates and again grown for two to three days to confirm colony color.

To isolate bacmid DNA, a single white colony was picked, added to 6 ml blue-white medium and grown overnight at 37 °C with medium agitation. Cells were pelleted and DNA was isolated with QIAprep Spin Miniprep Kit (Qiagen). Isolated DNA was finally solved in 50-100 µl sterile H_2O or TE buffer.

Blue-white agar: 1.5% (w/v) Agar, 1% (w/v) Tryptone, 0.5% (w/v) Yeast extract, 1% (w/v) NaCl, 0.1 mg/ml Bluo-gal, 0.04 mg/ml IPTG, 0.05 mg/ml Kanamycin, 7 µg/ml Gentamicin, 0.02 mg/ml Tetracycline

Blue-white medium: 1% (w/v) Tryptone, 0.5% (w/v) Yeast extract, 1% (w/v) NaCl, 0.05 mg/ml Kanamycin, 7 µg/ml Gentamicin, 0.02 mg/ml Tetracycline

Tetracycline solution (100 ml): 50 mg Tetracycline in 100 ml H_2O

Kanamycin (100 ml): 50 mg Kanamycin monosulfate in 100 ml H_2O

Gentamicin solution (100 ml): 50 mg Gentamicin sulfate in 100 ml H_2O

TE buffer: 10 mM Tris pH 8.0, 1 mM EDTA

4.3.4.2 Transfection of Sf9 insect cells with recombinant bacmid

5 to 15 µl of isolated bacmid DNA were used to transfect Sf9 insect cells. For each construct, 2 ml of Sf9 cells at $0.5X\ 10^6$ c/ml were plated into one 35-mm well of a 6-well plate. Bacmid DNA was mixed with 10 µl Cellfectin® II reagent and 200 µl Sf-900 II SFM medium and incubated at room temperature for 30 minutes. This allowed the lipid to cover the DNA for better uptake by the insect cells. Seeded cells were washed twice with unsupplemented Sf-900 II SFM medium. 800 µl unsupplemented Sf-900 II SFM medium was added to the DNA-Cellfectin mixture and the mixture was carefully applied onto the cells for 5 hours at 28 °C. After incubation time, DNA-Cellfectin mixture was aspirated from the cells and 2 ml Sf-900 II SFM medium supplemented with Gentamicin and FBS was gently added. Cells were allowed to grow for three to four days at 28 °C in sealed 6-well plates. Successful transfection of insect cells led to swelling of cells and finally cell death and was checked by light microscopy. The first virus generation P_0 was harvested with a sterile 2 ml syringe and filtered through a filter with 0.22 µm pore size prior to storage at 4 °C in the dark.

4.3.4.3 Amplification of baculovirus P_0 generation

Due to the low virus titer of P_0, the second baculovirus generation P_1 was amplified. P_1 was then used for later virus amplification and for protein test expression. For this purpose, 30 ml Sf9 cells at

a density of $0.5X\ 10^6$ c/ml were seeded in a sterile 26-cm tissue culture dish and 1 ml of P_0 was applied to transfect the cells. One dish with Sf9 cells at $0.5X\ 10^6$ c/ml without addition of virus was always incubated as a negative control for later comparison. Transfected cells were incubated for five to seven days at 28 °C protected from light. Transfection was checked by light microscopy and virus was harvested when holes in the cell lawn and many dead cells that detached from the surface could be observed. Cell suspension was transferred into a fresh 50 ml falcon tube and centrifuged for 15 minutes at 3 500 rpm and room temperature. Thus virus particles remained in the supernatant, whereas cells and debris were pelleted. Supernatant was stored at 4 °C in the dark in a sterile 50 ml falcon tube and used for amplification of the third virus generation P_2 and once for protein test expression. P_2 was obtained following the identical procedure as for P_1.

4.3.4.4 Protein expression in Sf9 insect cells
Protein expression in Sf9 insect cells was carried out in suspension culture at 28 °C and 110 rpm in an Innova 43 shaker (Eppendorf, Hamburg). The desired amount of Sf9 cells at a density of $2X\ 10^6$ c/ml was prepared in a sterile Erlenmeyer flask. Sf9 cells were infected with 1-6% (v/v, of prepared cell suspension) of virus and grown for 48 to 72 hours at 28 °C and 110 rpm. Cells were harvested by centrifugation at 1 500 rpm and room temperature for 15 minutes. Medium was discarded and cell pellets were either used for immediate protein purification or stored at -20 °C for later protein purification. Whenever MyoVa was expressed, cell pellets were shock-frozen in liquid nitrogen and used for protein purification or stored at -80 °C.

4.3.5   Affinity protein purification procedures
Protein tags introduced at the N- or C-terminus of the protein sequence enable easy protein purification and mostly yield in reasonably clean protein preparations. Either a FLAG® or a 6XHis-tag was used for protein purification in this study.

4.3.5.1 His-tag affinity purification
Cell pellet was resuspended in His lysis buffer. Cell debris was separated by centrifuging the suspension at 30 000 rpm and 4 °C for 10 minutes. The supernatant containing the target protein was incubated with about 0.5% (v/v) of washed Ni-NTA agarose beads (Qiagen) for 1.5 hours rolling in a Falcon tube at 4 °C. Agarose beads were spun down at 500 rpm and 4 °C for 15 minutes and supernatant was discarded. Beads were transferred into a 1.5 ml Eppendorf tube and agarose was washed six times with 1 ml His wash buffer. His-tagged protein was eluted twice with elution buffer for 30 minutes at 4 °C. Protein was either aliquoted, shock-frozen in liquid nitrogen and stored at -80 °C or subjected to subsequent FLAG-tag affinity purification. Protein purification was verified and protein concentration was determined by SDS-PAGE.

His lysis buffer: 20 mM Tris pH 8.0, 300 mM NaCl, 10 mM Imidazole, 1 mM DTT, 0.5% Triton X-100, protease inhibitor cocktail

His wash buffer: 50 mM Tris pH 8.0, 500 mM NaCl, 40 mM Imidazole, 1 mM $MgCl_2$, 1 mM EGTA, 1 mM DTT, 0.05% Tween-20

His elution buffer: 50 mM Tris pH 7.5, 150 mM NaCl, 300-500 mM Imidazole, 1 mM $MgCl_2$, 1 mM EGTA, 1mM DTT, 0.05% Tween-20

4.3.5.2 FLAG-tag affinity purification

FLAG®-tagged proteins were purified with the following procedure: Cells were lyzed in FLAG lysis buffer. Lysate was centrifuged at 30,000 rpm and 4 °C for 10 to 15 minutes to pellet cell debris. Supernatant was transferred into a fresh Falcon tube and 0.1% (v/v) FLAG® Resin (Sigma-Aldrich) was added and incubated for 1.5 hours at 4 °C on a rolling device. Suspension was centrifuged at 500 rpm and 4 °C for 15 minutes to pellet agarose beads. Supernatant was discarded and beads were transferred into a fresh 1.5 ml Eppendorf tube. To remove unspecifically bound proteins from FLAG® resin, beads were washed three times with 1 ml FLAG wash buffer I followed by three times 1 ml of FLAG wash buffer II. Protein was eluted twice by applying 0.2% (v/v) elution buffer to FLAG® resin and incubating it for 30 minutes at 4 °C on a rolling device. Elution was aliquoted, shock-frozen in liquid nitrogen and stored at -80 °C. Protein concentration was determined on a SDS gel.

FLAG lysis buffer: 20 mM Tris pH 7.5, 300 mM NaCl, 1 mM $MgCl_2$, 1 mM DTT, 0.5% Triton X-100, protease inhibitor cocktail

FLAG wash buffer I: 50 mM Tris pH 7.5, 500 mM NaCl, 1 mM $MgCl_2$, 1 mM EGTA, 1 mM DTT, 0.1% Tween-20

FLAG wash buffer II: 50 mM Tris pH 7.5, 150 mM NaCl, 1 mM $MgCl_2$, 1 mM EGTA, 1 mM DTT, 0.05% Tween-20

FLAG elution buffer: 50 mM Tris pH 7.5, 150 mM NaCl, 1 mM $MgCl_2$, 1 mM EGTA, 1 mM DTT, 0.05% Tween-20, 0.2 mg/ml FLAG® peptides

4.3.5.3 Optimized FLAG-tag affinity purification for *Xl*MyoVa and *Mm*MyoVa

Purification of FLAG®-tagged MyoVa was performed as described in (95) with minor changes. After 72 hours of growth, virus-infected cells were harvested. Supernatant was discarded and cell pellet was frozen in liquid nitrogen. Pellet was resuspended in MyoVa lysis buffer and homogenized in a glass homogenizer for five minutes on ice. Homogenate was transferred into a fresh Falcon tube and incubated on a rolling device at 4 °C for 20 minutes. Suspension was cleared by centrifugation for 15 minutes at 4 °C and 35 000 rpm. Supernatant was incubated with FLAG®-Resin for 1.5 hours. Beads were washed on a PolyPrep column (Bio-Rad) with 2 ml each of MyoVa wash buffer I, MyoVa wash buffer II, MyoVa wash buffer I, MyoVa wash buffer III, MyoVa wash buffer IV, MyoVa wash buffer III and MyoVa wash buffer I. MyoVa was eluted with MyoVa elution buffer, aliquoted, frozen in liquid nitrogen and stored at -80 °C.

MyoVa lysis buffer: 10 mM MOPS pH 7.0, 200 mM NaCl, 10 mM $MgCl_2$, 1 mM EGTA, 2 mM ATP, 0.1 mM PMSF, 1 mM DTT, protease inhibitor cocktail

MyoVa wash buffer I: 10 mM MOPS pH 7.0, 500 mM NaCl, 0.1 mM EGTA, 1 mM DTT, 0.1 mM PMSF

MyoVa wash buffer II: 10 mM MOPS pH 7.0, 500 mM NaCl, 0.1 mM EGTA, 1 mM DTT, 0.1 mM PMSF, 1 mM ATP, 5 mM $MgCl_2$

MyoVa wash buffer III: 10 mM MOPS pH 7.0, 0.1 mM EGTA, 1 mM DTT, 0.1 mM PMSF, 1 mM EDTA

MyoVa wash buffer IV: 10 mM MOPS pH 7.0, 500 mM NaCl, 0.1 mM EGTA, 1 mM DTT, 0.1 mM PMSF, 1 mM EDTA

MyoVa elution buffer: 10 mM MOPS pH 7.0, 200 mM KCl, 0.1 mM EGTA, 1 mM DTT, 0.1 mM PMSF, 0.3 mg/ml FLAG® peptides

4.3.6   Reconstitution of the tripartite MyoVa receptor complex *in vitro*

Previously tandem purified Rab/Mlph complex was again bound to NiNTA agarose beads for 1.5 hours at 4 °C and washed with His wash buffer to remove unbound proteins. Rab27a/Mlph-loaded NiNTA beads were incubated with separately purified MyoVa diluted in His dilution buffer for 1.5 hours rolling at 4 °C. Beads were washed six times with His wash buffer before eluting the tripartite complex twice for 30 minutes with His elution buffer.

His dilution buffer: 50 mM Tris pH 7.5, 150 mM NaCl, 1 mM $MgCl_2$, 1 mM EGTA, 1mM DTT

His wash buffer: 50 mM Tris pH 8.0, 500 mM NaCl, 40 mM Imidazole, 1 mM $MgCl_2$, 1 mM EGTA, 1 mM DTT, 0.05% Tween-20

His elution buffer: 50 mM Tris pH 7.5, 150 mM NaCl, 300-500 mM Imidazole, 1 mM $MgCl_2$, 1 mM EGTA, 1mM DTT

4.3.7   Fluorescent labeling of proteins

Recombinantly expressed proteins in this study were fluorescently labeled employing the SNAP-tag method (New England BioLabs, Frankfurt a. Main).

For this purpose, the protein of interest (here: Rab27a) was N- or C-terminally tagged with a SNAP-tag. The SNAP-tag is derived from mammalian O^6-alkylguanine-DNA-alkyltransferase and has a size of about 30 kDa (96, 97). Fluorescent dyes (in this study: SNAP-Surface® Alexa Fluor® 488 or 647) are coupled to derivatives of benzylguanines and benzylchloropyrimidines that are employed as SNAP substrates. During the labeling reaction, the substituted benzyl group of the substrate with the dye is covalently bound to the SNAP-tag carrying protein of interest. The respective protein was purified using the standard protein purification protocol and prior to elution it was labeled with 10 µM SNAP-tag substrate in the wash buffer for one hour at room temperature and in the dark on a rotator. The beads were extensively washed with wash buffer to remove excess dye prior to elution.

4.3.8   Dephosphorylation and phosphorylation of Mlph

*Xt*Mlph or *Mm*Mlph was dephosphorylated or phosphorylated during the purification procedure to reveal direct effects of Mlph phosphorylation. Therefore, protein was bound to agarose beads and unspecifically bound proteins were washed off. To phosphorylate Mlph, 200 to 900 nM PKA catalytic subunit (Sigma-Aldrich) and 10 000 U PKA (catalytic subunit, New England Biolabs) in kinase buffer with 0.25 mM ATP were incubated with Mlph-coated beads for one hour at room temperature on a rotator. To protect phosphorylated protein, phosphatase inhibitor cocktatil PhosSTOP was included in all wash buffers. For dephosphorylation, 30 to 60 units of antarctic phosphatase and 30 units of human protein phosphatase 2A in dephosphorylation buffer were applied onto the protein-bound beads for one hour at room temperature on a rotator. Kinase and phosphatases were removed by washing the beads at least four times with wash buffer.

Kinase buffer: 25 mM Imidazole pH 7.5, 25 mM KCl, 10 mM $MgCl_2$, 10 mM DTT

Dephosphorylation buffer: 25 mM Imidazole pH 7.5, 25 mM KCl, 11 mM $MgCl_2$, 10 mM DTT, 50mM Bis-Tris-Propane-HCl, 0.1 mM $ZnCl_2$

4.3.9   Protein purification by chromatography

4.3.9.1 Ion exchange chromatography

To purify (especially) His-tagged proteins further, ion exchange chromatography was applied. This separation technique relies on electrostatic interactions between charged molecules and a charged bead matrix. Each protein possesses a characteristic isoelectric point where the net electrical charge is zero. Due to this property, every molecule is released from the bead matrix at a different salt concentration when the pH value remains constant. In this thesis, the strong anion exchanger column Mono Q HR 5/5 (GE Healthcare Life Sciences) was employed. It is packed with 10 µm beads that are positively charged with the group -CH_2-$N^+(CH_3)_3$ allowing high performance chromatography and sharp peaks. In order to separate the protein of interest from contaminating proteins that were also eluted, previously dialyzed protein mixture was loaded onto a Mono Q HR 5/5 column that was equilibrated in Mono Q buffer A with 30 mM NaCl (3% Mono Q buffer B) using a FPLC system (Amersham Biosciences). All buffers were sterile-filtered through a 0.22 µm pore size membrane and degassed prior to usage. A salt gradient over 20 column volumes (CV) from 30 mM to 500 mM NaCl was run at a flow rate of 0.75 to 1 ml per minute (ml/min) depending on the back pressure of the column. Peak fractions were collected in 0.5 ml fraction size and analyzed on a SDS gel. Mono Q column was cleaned with five CVs of 100% Mono Q buffer B followed by at least 20 CVs of 3% Mono Q buffer B. Buffer was washed out with minimum 20 CVs of H_2O and column was slowly rinsed with 20% EtOH for long-term storage.

Dialysis buffer: 20 mM Tris pH 8.0, 30 mM NaCl, 1 mM $MgCl_2$, 1 mM EGTA, 1 mM DTT

Mono Q buffer A: 20 mM Tris pH 8.0, 1 mM $MgCl_2$, 1 mM EGTA, 1 mM DTT

Mono Q buffer B: 20 mM Tris pH 8.0, 1 M NaCl, 1 mM $MgCl_2$, 1 mM EGTA, 1 mM DTT

4.3.10   Methods for functional protein analysis

4.3.10.1   *In vitro* motility assay with melanosomes on F-actin

Figure 7: Schematic overview of motility assay setup with isolated melanosomes on surface-adhered F-actin *in vitro*.

For motility assays, 15 µl flow cells covered by a nitrocellulose coverslip were used (Figure 7). Actin-adherence to the glass coverslip was performed as previously described (98). For this purpose, 0.2 mg/ml N-ethylmaleimide-modified heavy meromyosin (NEM-HMM) (gift of Matthias Rief, Technische Universität München) was infused into the flow cell and incubated for 5 minutes. Remaining NEM-HMM was removed by washing with AB. Then, 0.5 to 1 µM fluorescently labeled F-actin was infused and incubated for 5 minutes, followed by a wash step with AB. To prevent unspecific binding to the glass surface, an additional wash step with casein (15 mg/ml in AB) was included. Finally, purified pigment granules diluted in AB (plus 2 mM ATP) were perfused into the flow cell and incubated for an additional two minutes.

In vitro motility was observed at room temperature by video-enhanced differential interference contrast (DIC) microscopy using a Zeiss Axiophot (Oberkochen) equipped with a plan-apochromatic oil immersion objective lens (63X; NA 1.4), DIC prisms, and an oil-immersion condenser (for NA 1.4). Images were captured with a C2400 Newicon camera (Hamamatsu Photonics, Herrsching), while contrast enhancement was performed using a DVS1000 video processor (Hamamatsu Photonics). Image data was digitally recorded and saved as TIFF image sequences with a frame interval of one second. By taking eight image sequences of approximately one minute, the average acquisition time of one flow chamber typically was ten minutes.

Quality and density of actin filaments in flow cells was monitored for every flow cell using an Axiophot (Zeiss) equipped with plan-apochromatic oil immersion objective lens (63X; NA 1.4), and filter No. 10 (Zeiss; excitation: BP 450-490 nm, FT 510 nm, emission: BP 515-565 nm). For excitation, a HBO 100 light source was used (Zeiss). Fluorescent images of flow cell-adhered F-actin were acquired using an inverted Axiovert 200M microscope (Zeiss) equipped with a plan-apochromatic oil immersion objective lens (100X; NA 1.4). For excitation, a HBO 103 light source was used and emission was collected using a Zeiss filter set 38HE.

NEM buffer: 25 mM Imidazole pH 7.5, 4.4 mM $MgCl_2$, 1 mM EGTA, 300 mM KCl, 10 mM DTT

Collodion solution: 0.1% collodion in isoamyl alcohol

Casein: 15 mg/ml Casein (30 mg/ml in Tris-Cl) in AB buffer

AB: 25 mM Imidazole pH 7.5, 25 mM KCl, 4 mM $MgCl_2$, 1 mM EGTA, 10 mM DTT

ATP solution (0.1 M pH 7.0): 100 mM Na_2ATP in H_2O

4.3.10.2 Coimmunoprecipitation

To test the interaction of two proteins, Sf9 cells were coinfected with two baculoviruses. It was important to always use differently tagged protein combinations. A FLAG-tagged protein was coexpressed with either an untagged protein or a His-tagged protein. Standard protein purification was carried out (section 4.3.5.2 FLAG-tag affinity purification) and coimmunoprecipitation was analyzed with SDS-PAGE.

4.3.10.3 Negative-staining transmission electron microscopy

Samples were adsorbed on glow-discharged formvar-supported carbon-coated Cu400 TEM grids (Science Services, Munich) and stained using a 2% aqueous uranyl formate solution containing 25 mM sodium hydroxide. Imaging was performed using a Philips CM100 EM operated at 100 kV. Images were acquired using an AMT 4 Megapixel CCD camera. Micrograph scale bars were calibrated by imaging 2D catalase crystals and using the lattice constants as length reference. Imaging was performed at 28 500X magnification. Single particle micrographs were created by manual particle picking using the Xmipp 3.1 boxing routine (99).

4.3.10.4 *In vitro* phosphorylation assay with isotope-labeled ATP

The use of radiolabeled ATP (Adenosine 5'-triphosphate [γ-32P]) enables to identify targets of protein kinases. Kinase and presumptive target are incubated in the presence of isotope-labeled ATP. The mixture is separated by SDS-PAGE and the gel is placed against a phosphor storage screen. The screen is then scanned with a phosphorimager and appearing bands represent phosphorylated proteins.

200 nM of freshly dissolved PKA catalytic subunit was mixed with 1.2 µM of substrate in kinase buffer in a constant sample volume of 30 µl. 1 µM isotope-labeled ATP (diluted 1:30 with cold ATP) was added to start the reaction and incubated at 30 °C in a thermo mixer for 15 minutes. Reaction was stopped by adding 10 µl of SDS sample buffer. Time course experiments were performed using a master mix of kinase-substrate mixture. At desired time points, 30 µl were taken out and pipetted into previously prepared Eppendorf tubes with 10 µl SDS sample buffer. For determining the stoichiometry of ABD phosphorylation, 0.5 µM of substrate was mixed with 200 nM PKA and incubated at 30 °C for 20 minutes. 15 µl of each reaction were applied onto a 12.5% SDS gel and electrophoresis was run for 1 hour at 300 V and 35 mA per gel. The gel apparatus was carefully disassembled and the gel was sealed with plastic wrap before placing it against the phosphor storage screen overnight. The screen was scanned with a phosphorimager (Typhoon 9200, Molecular Dynamics) and digital images were used for analysis.

Kinase buffer: 25 mM Imidazole pH 7.5, 25 mM KCl, 10 mM MgCl$_2$, 10 mM DTT

4.3.10.5   *In vitro* filament decoration assay with Mlph proteins and F-actin

0.25 µM biotinylated G-actin and 4.75 µM G-actin were polymerized with 5 µM Atto488-phalloidin in AB for 30 minutes at room temperature. 0.5 mg/ml biotinylated BSA was flowed into a 10 µl flow chamber and incubated for three minutes. Glass surface was blocked with 8 mg/ml BSA in AB. 0.5 mg/ml streptavidin was bound to biotinylated BSA for three minutes followed by a wash step with 8 mg/ml BSA in AB. Biotinylated actin filaments were attached to the biotin-streptavidin layer and unbound filaments were washed out with 8 mg/ml BSA in AB. Alexa Fluor 647-labeled Rab27a/Mlph complex diluted in AB was infused into the flow chamber. The chamber was washed with AB supplemented with 0.4% Glucose, 0.18 mg/ml glucose-oxidase, and 0.06 mg/ml catalase and image acquisition of the sealed chamber was performed at room temperature using a commercially built TIRF microscope (Leica AF6000 Modular Systems, Leica, Wetzlar, Germany) equipped with a HCX PL Apo 100X/1.47 TIRF objective. Images were acquired with an iXon Ultra X-9360 EMCCD camera (Andor, Belfast, U.K.) controlled by the Leica Application Suite Advanced Fluorescence. Acquired images were further processed using the ImageJ software.

AB: 25 mM Imidazole pH 7.5, 25 mM KCl, 4 mM MgCl$_2$, 1 mM EGTA, 10 mM DTT

4.3.10.6   Single-molecule TIRF assay with tripartite complex on F-actin

The tripartite MyoVa transport complex Rab27a/Mlph/MyoVa was reconstituted and labeled with Alexa Fluor 488 or 647 on the SNAP-tagged Rab27a subunit as described in section 4.3.7. 0.25 µM biotinylated G-actin and 4.75 µM G-actin were polymerized with 5 µM Atto488- or Atto647N-phalloidin in AB for 90 to 120 minutes at room temperature and then stored on ice. Actin filaments were attached to the glass surface via biotin-streptavidin (see 4.3.10.5) and wash steps were carried out with AB supplemented with 1 mg/ml BSA. The glass surface was blocked with 8 mg/ml BSA in AB after incubation with actin filaments. Reconstituted tripartite complex diluted in AB supplemented with 0.4% Glucose, 0.18 mg/ml glucose-oxidase, 0.06 mg/ml catalase, 2 mM ATP, and 0.06 mg/ml bovine calmodulin (Calbiochem, San Diego, U. S. A.) was flowed into the chamber. Sealed chambers were imaged at room temperature using the TIRF microscope setup described before. Acquired images and movies were further processed using the ImageJ software.

4.3.10.7   Photobleaching assay

All tripartite complexes used for single-molecule TIRF assays were also subjected to photobleaching assays to ensure that transport parameters were mainly obtained from single tripartite complexes and not oligomeric complexes. For this purpose, Rab27a/Mlph/MyoVa complexes were diluted in AB and unspecifically bound to the glass surface of a flow chamber. The time-lapse recordings were performed at 80% laser power and 200 ms exposure time. Spots for analysis were chosen for all constructs by intensity over mean intensity and the intensity values for a 3X3 pixel window were summarized. Observation of the spot intensities over time resulted in bleaching curves. Performing a gliding-t-value test with a corresponding threshold identified the bleaching steps (100).

4.3.10.8   *In vitro* filament decoration assay with Mlph proteins and MTs

Tubulin was prepared from porcine brain and polymerized as described previously (4.3.2.3 and 4.3.2.4). Biotinylated BSA was flowed into a 10 µl flow chamber and incubated for three minutes. Glass surface was blocked with 8 mg/ml BSA in BRB80 buffer. Streptavidin was bound to biotinylated BSA for three minutes followed by a wash step with 8 mg/ml BSA in BRB80 buffer. Biotinylated and Atto488-labeled MTs were attached to the biotin-streptavidin layer and unbound filaments were washed out with 8 mg/ml BSA in BRB80 buffer. Alexa Fluor 647-labeled Rab27a/Mlph complexes diluted in BRB80 buffer were flowed into the flow chamber. Excess protein was removed by washing with BRB80 supplemented with 0.4% Glucose, 0.18 mg/ml glucose-oxidase, and 0.06 mg/ml catalase. Sealed chambers were imaged at room temperature as described above (see 4.3.10.5).

BRB80 buffer: 80 mM Pipes pH 6.9, 2 mM $MgCl_2$, 1 mM EGTA, 5 mM DTT

4.3.10.9   MT cosedimentation assay with Mlph proteins

Tubulin was polymerized at 35 °C in BRB80 buffer supplemented with 1 mM GTP. 5 µM taxol was added after incubation for 30 minutes at 35 °C and polymerized MTs were kept at 35 °C overnight. MTs were centrifuged through a sucrose cushion (40% sucrose in BRB80) and resuspended in BRB80 buffer supplemented with 5 µM taxol. Cosedimentation assays were carried out in BRB80 buffer with 2 µM MTs and 5 µM of the respective *Mm*Mlph protein. Reactions were mixed thoroughly and incubated at room temperature for 15 minutes. MT-Mlph mixes were carefully pipetted onto a sucrose cushion and centrifuged at 80 000 rpm for 15 minutes at 22 °C. Supernatant was gently removed and sucrose cushion was washed with BRB80. Sucrose cushion was taken off and pellet was washed twice with BRB80. Pellet was resuspended in BRB80 and samples of total reaction, supernatant, and pellet were prepared and analyzed with SDS-PAGE.

BRB80 buffer: 80 mM Pipes pH 6.9, 2 mM $MgCl_2$, 1 mM EGTA, 5 mM DTT

4.3.10.10   *In vitro* filament decoration assay with Mlph proteins on networks built with F-actin and MTs

Competition experiments with mixed networks (MTs and actin filaments) were performed with biotinylated, Atto488-labeled MTs and biotinylated, Atto565-labeled actin filaments. Surface-attachment of filaments was performed via the biotin-streptavidin layer in BRB80 buffer (see 4.3.10.8). Actin filaments were flowed into the prepared flow chamber first, followed by MTs. After removing unbound filaments with a wash step with 8 mg/ml BSA in BRB80 buffer, Alexa Fluor 647-labeled, dephosphorylated or phosphorylated Rab27a/Mlph protein was infused into the flow chamber and image acquisition was performed as described above (see 4.3.10.5).

BRB80 buffer: 80 mM Pipes pH 6.9, 2 mM $MgCl_2$, 1 mM EGTA, 5 mM DTT

4.3.10.11   Single-molecule TIRF assay with tripartite complex on F-actin and MTs

MTs and actin filaments were prepared as described previously. Briefly, Atto488-labeled MTs and Atto565-labeled actin filaments, both biotinylated, were employed in this experiment. MTs were first attached to the surface of a flow chamber, followed by actin filaments. Wash steps were performed using BRB80 buffer. After perfusing the actin filaments into the flow chamber, surface was blocked with 10 mg/ml BSA in AB. Alexa Fluor 647-labeled dephosphorylated or phosphorylated Rab27a/Mlph/MyoVa complex was diluted in AB supplemented with 0.4% Glucose, 0.18 mg/ml glucose-oxidase, 0.06 mg/ml catalase, 2 mM ATP, and 0.06 mg/ml bovine calmodulin and flowed into the chamber. Time-lapse movies with a cycle time of 223 ms were acquired using the previously described TIRF microscope. To analyze the switching behavior of the MyoVa transport complex on mixed networks, only complexes in close proximity to a MT-actin intersection were taken into account. The number of complexes that switched filament at an intersection or passed the intersection without changing filament was manually counted. The percentage of switching complexes or passing complexes was calculated for dephosphorylated or phosphorylated Rab27a/Mlph/MyoVa complexes with and without Mlph's ABD.

BRB80 buffer: 80 mM Pipes pH 6.9, 2 mM $MgCl_2$, 1 mM EGTA, 5 mM DTT

AB: 25 mM Imidazole pH 7.5, 25 mM KCl, 4 mM $MgCl_2$, 1 mM EGTA, 10 mM DTT

4.3.10.12   Sequence alignment

*Xl*MyoVa sequence (JX494698.1) was aligned with *Mm*MyoVa (NP_034994.2) and *Mm*MyoVb (NP_963894.1) using ClustalX 2.1 (101). Following Mlph ABD sequences were aligned: *Mm*Mlph (NP_443748.2), *Hs*Mlph (NP_077006.1), *Fd*Mlph (XP_010624436.1), *Cl*Mlph (NP_001096689.2), *Oa*Mlph (NP_001139743.1), and *Xt*Mlph (NP_001120194.1). Alignment figures were prepared with the means of BioEdit Sequence Alignment Editor (102).

4.3.10.13   Mass spectrometry (LC-MS/MS) analysis

Wild type *Mm*Mlph was FLAG-affinity purified and dephosphorylated or phosphorylated while bound to FLAG-affinity resin. Purified protein was analyzed by the Mass Spectrometry Service of the Max Planck Institute of Biochemistry (Martinsried) using the following procedure: Protein samples were denatured adding 4 M guanidium hydrochloride solution (final concentration). The proteins were reduced and alkylated using 10 mM Tris(2-carboxyethyl)phosphine hydrochloride (TCEP) and 40 mM Chloroacetamide (CAA), respectively. Samples were then diluted to a final concentration of 0.4 M guanidium hydrochloride using 50 mM ammonium bicarbonate solution. These reduced and alkylated protein samples were digested overnight with trypsin (1 µg trypsin for 50 µg protein). After overnight digestion, peptides were desalted using a C_{18} StageTip (103) and used for LC-MS/MS analysis. Peptides were loaded on a 15 cm long 75 µm inner diameter reversed phase C_{18} column packed with 1.9 µm beads via autosampler in the Thermo Easy LC 1000. The peptides were separated over a 120 minute linear gradient with 0.1% formic acid (buffer A) as the loading buffer and 0.1% formic acid and 80% acetonitrile as the eluting buffer (buffer B). Separated peptides were directly electrosprayed into Q Exactive HF benchtop Orbitrap mass spectrometer (104). The mass spectrometer was operated in data dependent mode, with up to top 15 precursors selected for fragmentation. The full scans were acquired at 120 000 resolution (m/z=200) with up to 3E6 charges accumulated in the C-trap and the HCD fragmentation spectra were recorded at 15

000 resolution with up to 1E5 charges of the precursor ions. The raw data were processed with MaxQuant computation platform (105) version 1.5.2.22 using the Andromeda (106) search engine. Precursor and fragment ions were searched with 4.5 and 20 ppm mass tolerance, respectively, with FDR set to 1% both at the protein and peptide level. Carbamidomethylation of cysteine was set as fixed modification and oxidation of methionine, protein N-terminal acetylation and phosphorylation on serine, threonine and tyrosine were used as variation modifications in the database search.

4.4 Data analysis

4.4.1 DIC microscopy: Melanosome tracking with Particle Tracker (ImageJ)

Quantification of actin-based melanosome transport with granules from the aggregated or dispersed cell state was carried out with the data obtained from the *in vitro* melanosome motility experiments on F-actin.

Melanosome transport events were defined as a sequence of one-directional, uninterrupted, linear displacement that lasted for 3 seconds and longer. The acquired image sequences were then analyzed by means of ImageJ software and the plugin *ParticleTracker 2D/3D* (107). For tracking, images were adjusted according to the manual and the following parameters were set prior running the program: Kernel radius 5 to 7 pixels (px); cutoff radius 1 to 3 px; percentile 0.1; maximum displacement 50 px; and link range 2 to 3 frames.

Trajectories that met all of the criteria above were analyzed by converting the tracking-coordinates into travelled distances applying Pythagoras' theorem.

4.4.2 DIC microscopy: Velocity and run-length measurements

For the biophysical characterization of melanosome transport under various conditions, the following parameters were determined: (i) *run length (r)* was defined as the total distance that was covered by an individual melanosome during one transport event on F-actin; and (ii) *transport velocity (v)* for a given melanosome was calculated from the total run length the melanosome of interest traveled in a given time. Single values for velocity and run length of individual transport events were plotted as a histogram. In the case of *v*, a single Gaussian was fitted to the data according to Equation 1.

$$y = a * \exp[-(\frac{x-x0}{b)^2}] \quad \text{Equation 1}$$

Based on the obtained Gaussian fit curve for the obtained velocity histogram, the mean velocity was determined. As previously described (108), mean values for *r* were obtained from a single-exponential fit to the histogram plots that derived from the respective measured single values.

Kymographs of representative image-sequences from the performed *in vitro* motility assays on F-actin were generated with the MultipleKymograph macro for ImageJ.

4.4.3 Statistical analysis of motile melanosomes

To determine the fraction of motile versus non-motile melanosomes, according to the criteria described above, all surface-adhered melanosomes recorded, were checked for potential displacements. Subsequently, based on the total number of surface-bound melanosomes, the fraction of moving melanosomes was calculated. The thereby obtained values from each isolation of the respective condition were averaged and SD, as well as SEM was calculated.Data plotting and

fitting, but also the statistical analysis was performed with IgorPro software (WaveMetrics Inc., Portland, U.S.A.).

4.4.4   Analysis of time course phosphorylation assays

Digital images of scanned phosphor storage screens were analyzed using ImageJ software. The mean gray value of each band representing an individual time point was measured using the polygonal selection tool with constant area. For background subtraction, the mean gray value of four different parts of the gel with identical area as for the time points were averaged and subtracted from mean gray values of time points. Obtained values were divided by 1×10^6 and plotted against time with means of the Origin software. The resulting curve was fitted with a single-exponential function.

4.4.5   Analysis of the stoichiometry of Mlph ABD phosphorylation

Digital images of scanned phosphor storage screens were analyzed using ImageJ software. The mean gray value of each band representing wild type or point mutated Mlph was measured using the polygonal selection tool with constant area. For background subtraction, the mean gray value of four different parts of the gel with identical area as for the Mlph proteins were averaged and subtracted from mean gray values of the different Mlph proteins. The acquired values were corrected for applied protein amounts determined with the corresponding Coomassie-stained SDS-PAGE. The value obtained for wild type Mlph was set to 100% and values of different Mlph point mutants were compared to the wild type Mlph value.

4.4.6   Quantification of filament decoration assays with Mlph proteins and F-actin

For quantification of the Mlph-actin interaction, 400 nM of phosphatase-treated, Alexa Fluor 488-labeled Rab27a/Mlph complex and PKA-treated, Alexa Fluor 647-labeled Rab27a/Mlph complex (or complexes with swapped fluorescent dyes) were perfused into the flow chamber with surface-attached Atto565-labeled actin filaments. The color swap on the Rab27a/Mlph protein controlled for inherent intensity differences of the Alexa Fluor 647 and Alexa Fluor 488 fluorophores. Association of dephosphorylated or phosphorylated Mlph to actin filaments was evaluated using a co-localization analysis script implemented in MATLAB. The filament images were binarized using a common threshold algorithm (109). The available binding area of actin filaments was determined after crossing or overlapping sections of filaments were deleted from the binary images. The background in each Rab27a/Mlph image was calculated as the mean of the image without the actin area and subtracted from the images. A normalization parameter was introduced in order to account for differences in the imaging parameters for the two Rab27a/Mlph channels (488 and 647 channel). The images were normalized ignoring a percentage of pixels that was given by the parameter. The value was chosen by a parameter space check for the value where both original experiment and color swap experiment resulted in the same (inverse) ratio of decoration. This ratio of bound Rab27a/Mlph was calculated from the intensity observed in the actin area for the phosphorylated channel, divided by the intensity in the dephosphorylated channel. Data from 30 images for the combination of dephosphorylated Alexa Fluor 488- and phosphorylated Alexa Fluor 647-Rab27a/Mlph complexes and 44 images for the combination of phosphorylated Alexa Fluor 488- and dephosphorylated Alexa Fluor 647-Rab27a/Mlph complexes were analyzed. Errors are given as SD between ratios for the single images analyzed for each experiment.

4.4.7   Data analysis of single-molecule TIRF assays with tripartite complex on F-actin

Movies were recorded at a cycle time of 238 ms and analyzed using a custom routine implemented in the MATLAB development environment. Spots were selected automatically according to their brightness compared to the mean brightness in each frame. The position of the spots was determined with sub-pixel accuracy using a radial center approach. A list of spots for each frame was generated and the distances of spots between each subsequent frame was compared. The connection of each spot to the closest one in the next frame (with a cutoff maximal distance) resulted in tracking traces for each spot. The distance to the first position of each spot over time was fitted with a linear model. Smooth runs that resulted in a linear fit with a r^2-value higher than 97% and had a length of at least 10 frames were chosen for speed and run length measurements. For run length measurements an additional threshold of 1 μm was applied. The speed was calculated from the slope of the performed fit and the run length was calculated from the maximal distance of the spot from its original position. Missing run lengths were accounted for in the histogram fit by truncating the single exponential model.

4.4.8   Analysis of MT cosedimentation assays with Mlph proteins

Digital images of total, supernatant, and pellet of each reaction on Coomassie-stained SDS gels were analyzed with ImageJ and MATLAB, respectively. In order to calculate the relative degrees of MT-bound protein fraction, a semi-automatic routine was implemented using MATLAB. The area containing the peak of interest was chosen manually from an intensity lane profile of the gel created with ImageJ. Binning the intensity for a histogram and using the upper limit of the heaviest populated bin as a threshold, the peak data was separated from the baseline. To account for a linear variation of the base line, a straight line was fitted to the separated baseline data. The peak area was calculated integrating the intensity data between the first interceptions of this line with the profile data before and after the peak. Resulting area values were used and percentages of MT-bound protein to total protein were calculated. The relative degree of MT-bound *Mm*Mlph ΔABD fraction was not determinable because of the close proximity of protein and tubulin peaks.

4.4.9   Quantification of filament decoration assays with Mlph proteins and MTs and F-actin

Competitive Mlph binding to MTs and actin filaments was evaluated using a co-localization analysis script implemented in MATLAB as described in 4.4.6 (page 57). The available binding area for each filament type was determined as detailed previously. The channel for Mlph-associated fluorescence was also thresholded in order to avoid influence of the background intensity on the data. The sum of Mlph-associated intensity in the area of filaments detected before was normalized to the total binding area of this filament type, yielding a binding parameter B_filament. The binding proportion for each filament was then calculated as B_filament1/(B_filament1 + B_filament2). Data from 17 images for the dephosphorylated Rab27a/Mlph complex and 29 images for the phosphorylated Rab27a/Mlph complex were analyzed. The ratio of the binding area (actin : MTs) for the competition experiments with the dephosphorylated Rab27a/Mlph complex was 4.87 ± 1.58. The ratio of the binding area (actin : MTs) for the competition experiments with the phosphorylated Rab27a/Mlph complex was 2.78 ± 1.46. Error bars were calculated from the SD occurring when averaging over data from all images.

5. <u>Results</u>

5.1 <u>PKA directly regulates the MyoVa-mediated melanosome transport on F-actin *in vitro*</u>

To date, the MyoVa-dependent transport has been reconstituted on actin cables from *Nitella* with melanosomes that were purified from uninduced melanophores (15) and with melanosomes purified from mouse melanocytes on bundled F-actin (110). *Xenopus laevis* melanosomes displayed an atypically slow velocity of 0.036 µm s^{-1}, whereas melanosomes derived from mouse cells moved between 0.1 and 0.3 µm s^{-1}. Given the *in vitro* velocities of purified MyoVa motors were reported to be around 0.3 µm s^{-1} (36), the slow velocity displayed by melanosomes from *Xenopus laevis* is surprising.

The cloning of the full length MyoVa motor involved in melanosome transport demonstrated that this motor is indeed capable of supporting movement at 0.13 µm s^{-1} *in vitro* (90). Is the atypically slow MyoVa-dependent movement of melanosomes from *Xenopus laevis* a result of regulation of the MyoVa on the melanosome surface? If so, do melanosomes isolated from dispersed and aggregated cell states behave differently *in vitro*? And lastly, does PKA directly affect the reconstituted melanosome transport *in vitro*? I sought answers to these questions by reconstituting the MyoVa-dependent transport of melanosomes isolated from the distinct cell states on F-actin.

5.1.1   <u>Reconstitution of melanosome motility on F-actin *in vitro*</u>

I achieved to isolate functional pigment granules and reconstitute the transport process on surface-adhered F-actin *in vitro*. To this end, I made use of the previously described melanosome purification method by Gelfand and coworkers (12) and optimized it for motility assays on F-actin. The isolated pigment granules were flowed in flow chambers with previously surface-attached F-actin and motility was acquired using a DIC microscope (Figure 8). All motility assays were performed using the DIC microscope with which fluorescent actin was observable by eye only, but that was not equipped to record corresponding fluorescent images.
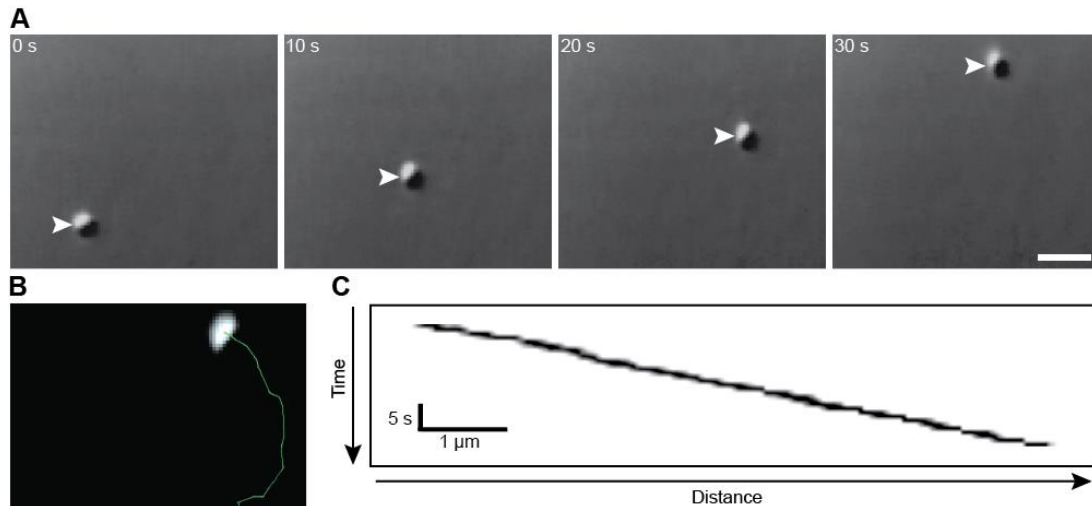
Figure 8: Trajectory of a melanosome from a dispersed cell moving on surface-adhered F-actin *in vitro*. (A) Selected DIC images taken at 10 s intervals. Scale bar: 2 µm. (B) Corresponding trajectory visualized using Particle Tracker 2D/3D. Scale bar: 1 µm. (C) Corresponding kymograph of sequential frames depicting the trajectory of a unidirectionally moving melanosome on F-actin *in vitro*.

To ensure that observed motility was a melanosome moving on an actin filament, a representative motility assay was additionally performed with a fluorescence microscope and Atto488-labeled actin filaments (Figure 9). These fluorescent images were merged with the corresponding phase-contrast images to visualize that the moving pigment organelle indeed used F-actin as a track. Figure 9 clearly illustrates that the movement occurs on the filament, but also that melanosomes appear as blurry black dots in bright field or phase-contrast microscopy. Hence, phase-contrast microscopy is unsuitable for imaging motility of melanosomes and DIC microscopy was employed for high quality acquisition of moving melanosomes.
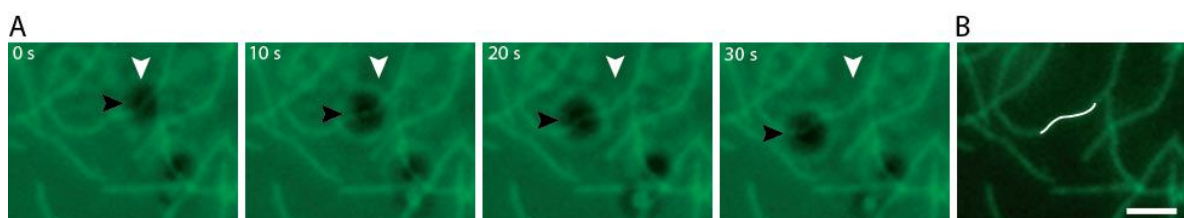
Figure 9: *In vitro* reconstitution of MyoVa-mediated melanosome transport on fluorescently labeled F-actin. (A) Phase contrast images of a moving melanosome derived from the dispersed state merged with corresponding fluorescent images of surface-attached F-actin labeled with Atto488-phalloidin. The black arrowhead depicts the position of the moving melanosome. The white arrowhead indicates the starting point of the trajectory. (B) The trajectory of the melanosome (white line) follows the path of the curved actin filament. Scale bar: 2 µm.

The first obvious step to gain insights into the regulation of MyoVa-dependent transport was to isolate melanosomes from the two different cell states and compare the observed motility. The hormone α-MSH was used to fully disperse the melanosomes within the melanophores prior to cell lysis and granule isolation. These melanosomes are referred to as dispersed melanosomes. Aggregation was induced by addition of melatonin to the melanophore medium. After completion of the aggregation process, melanosomes were purified and are called aggregated melanosomes.

Isolated melanosomes from dispersed and aggregated cells both exhibited unidirectional transport on surface-attached F-actin *in vitro*. The large number of moving melanosomes allowed a statistical analysis of the biophysical parameters of reconstituted melanosome transport (Figure 10, Video 1).
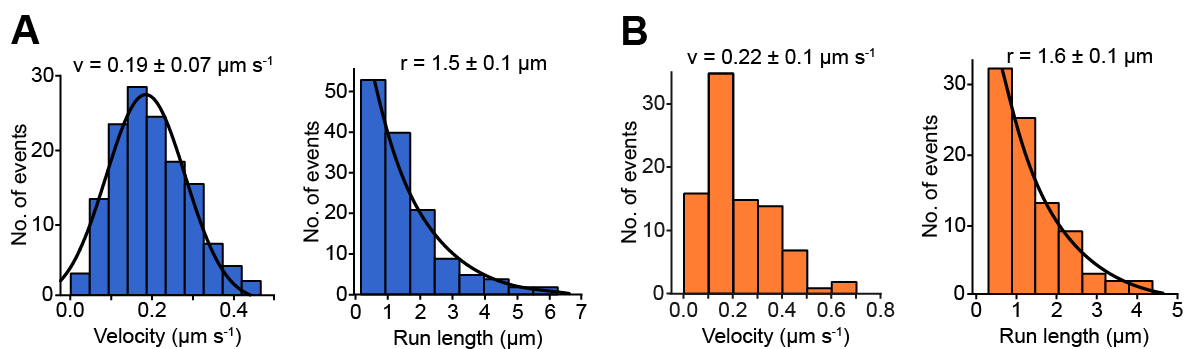
Figure 10: Purified melanosomes display consistent kinetic transport parameters *in vitro.* Motile (A) or dormant melanosomes (B) were purified from the dispersed (dark blue) and aggregated cell states (orange), respectively. Velocities (v) and run lengths (r) are mean values ± SD deduced from the Gaussian (velocities) and single-exponential (run lengths) fit curves (solid lines) to the histogram data, except for (B) for which the mean velocity was calculated.

Table IV: Biophysical parameters of melanosome transport *in vitro*. Melanosomes were purified from the distinct cell states (i.e. active melanosomes from dispersed cells, inactive melanosomes from aggregated cells, respectively). Mean values ± SD were obtained as described in Figure 10.

	Velocity [μm/s] ± S.D.	Run length [μm] ± S.D.	Analyzed runs	Independent isolations
Disp.	0.19 ± 0.07	1.5 ± 0.1	137	2
Aggr.	0.22 ± 0.1	1.6 ± 0.1	90	9

The biophysical parameters of melanosome transport from the distinct cell states do not show considerable differences between the dispersed and aggregated cell states.

Importantly, the observed velocities of melanosomes closely match the *in vitro* velocities of purified MyoVa from *Xenopus laevis* (90) and therefore validate my reconstitution assays with purified melanosomes.

Furthermore, the here obtained run lengths for melanosomes from dispersed and aggregated cell states agree well with the previously published run length for single MyoVa molecules from chicken (85).

5.1.2   Regulation of melanosome transport during dispersion and aggregation

To quantify the efficiency of initiated transport events by melanosomes derived from dispersed and aggregated cell states, only unidirectional melanosome movements that lasted three seconds or longer, covering a distance greater than 0.5 µm were taken into account for later analysis. Due to the sticky surface of isolated melanosomes, numerous melanosomes bound unspecifically to the glass surface. To compare the motility of melanosomes isolated from the distinct cell states, idle and motile melanosomes were counted and the percentage of transport events for each condition was calculated. The percentage of transport events was used as a standard to compare melanosome motility from different cell states.

Acquisition of over 1,300 melanosomes purified from dispersed melanophores yielded in an average motile fraction of 18.3% (Figure 11, Table V, Video 1). In contrast, over 2,000 melanosomes isolated from the aggregated cell state displayed an average percentage of transport events of 4.8% (Figure 11, Table V).
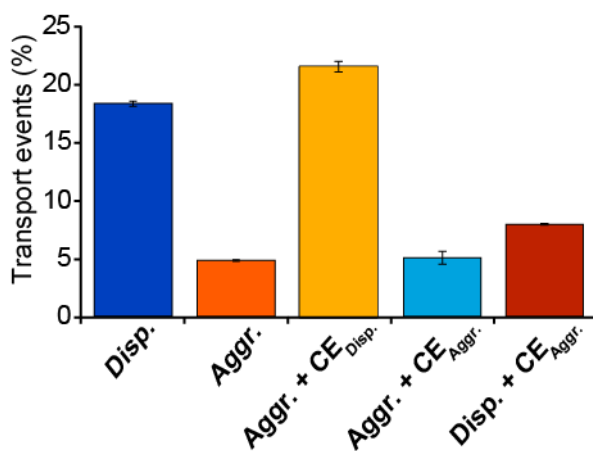
Figure 11: Cell state-dependent *in vitro* reconstitution of melanosome transport on F-actin. Melanosomes purified from the aggregated cell state (Aggr.; orange) display a pronounced decrease in MyoVa-dependent transport events compared to melanosomes purified from the dispersed cell state (Disp.; dark blue). Addition of cytoplasmic extract from dispersed cells ($CE_{Disp.}$; yellow), but not from aggregated cells ($CE_{Aggr.}$; light blue), reactivates dormant melanosomes purified from aggregated cells. Melanosomes derived from the dispersed cell state are rendered dormant by addition of cytoplasmic extract from aggregated cells (red). Error bars show the SEM.

These results show that MyoVa is more active during dispersion and in a rather idle state while melanosomes aggregate. Furthermore, the difference in transport events from dispersed and aggregated melanophores clearly demonstrates that this experimental setup enables the observation of regulated melanosome transport *in vitro*.

The observed differences in MyoVa-dependent transport between dispersion and aggregation raise the question what factor accounts for this effect. Is this activating factor present in the cytoplasm of dispersed cells? To test this hypothesis, melanosomes from aggregated cells were incubated with cytoplasmic extract from dispersed melanophores and vice versa (i.e. supernatant after second centrifugation step of purification, for details see section 4.3.3, page 46). Strikingly, melanosomes from the aggregated cell state that were incubated with dispersed cytoplasmic extract exhibited a significantly increased number of transport events of 21.5% (Figure 11, yellow bar, Table V, Video 2). In contrast, incubation of dispersed melanosomes with aggregated cytoplasmic extract reduced the mean transport events from 18.3% to 7.9% (Figure 11, red bar, Table V). Aggregated melanosomes were incubated with aggregated cytoplasmic extract to exclude any effects by the centrifugation and incubation procedure. As expected, the number of transport events remained unchanged at 5% (Figure 11, Table V).

Table V: Transport events from the dispersed and aggregated cell state incubated with aggregated or dispersed cytoplasmic extract. Transport event numbers represent the average of all isolations under identical conditions ± SD.

	Transport events ± S.D.	Independent isolations	Number of moving melanosomes	Total melanosomes
Disp.	18.3 ± 7.2%	11	257	1385
Aggr.	4.8 ± 1.5%	11	97	2023
Disp. + aggr. CE	7.9 ± 0.7%	3	24	292
Aggr. + aggr. CE	5.0 ± 4.2%	3	14	321
Aggr. + disp. CE	21.5 ± 10.7%	8	140	775

Thus cytoplasm from dispersed melanophores can reactivate dormant melanosomes derived from aggregated melanophores. The activating and inactivating factor(s) is/are indeed present in the cytoplasm.

5.1.3   PKA directly regulates MyoVa-driven melanosome transport *in vitro*

It is long known that cAMP and PKA play important roles in signal transduction for melanosome dispersion in *Xenopus laevis* melanophores, as well as in other pigment cells (9, 11, 52, 57, 81). With my experimental setup I was able to directly test whether PKA accounts for the increased activity of melanosomes from the dispersed cell sate. To this end, I made use of the constitutively active PKA and its specific inhibitor H-89 (111-113). Incubation of aggregated melanosomes with dispersed cytoplasmic extract that was supplemented with the PKA-specific inhibitor H-89 markedly suppressed the reactivation of the dormant melanosomes (Figure 12, yellow vs. green bar; Table VI).
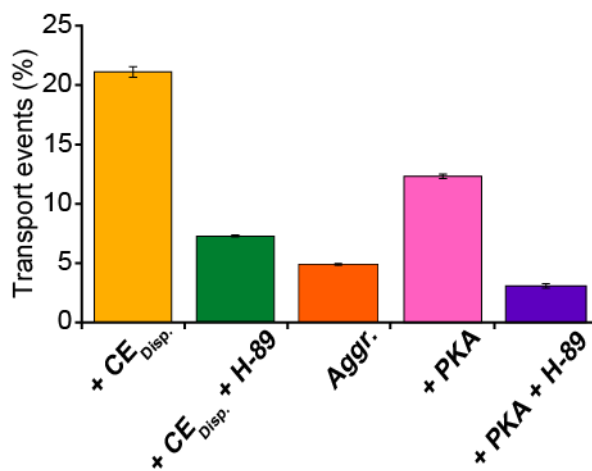
Figure 12: PKA reactivates dormant melanosomes *in vitro*. The reactivation of melanosomes from the aggregated cell state with dispersed cytoplasmic extract (yellow, replotted from Figure 11) was prevented by the PKA-specific inhibitor H-89 (green). Dormant melanosomes derived from the aggregated cell state (orange, replotted from Figure 11) were noticeably reactivated by purified PKA (magenta). PKA-dependent reactivation can be fully prevented by H-89 (purple). Error bars show the SEM.

Table VI: Reactivation and reinhibition of melanosomes purified from the aggregated cell state using exogenous PKA and its inhibitor, respectively. Transport event numbers represent the average of all isolations under identical conditions ± SD.

	Transport events ± SD	Independent isolations	Number of moving melanosomes	Total melanosomes
Aggr. + PKA	12.3 ± 3.8%	6	109	949
Aggr. + PKA + H-89	3.0 ± 1.5%	3	16	595
Aggr. + disp. CE + H-89	7.2 ± 1.1%	3	52	714

These results indicate the involvement of PKA in regulation of actin-based melanosome transport. To test whether PKA directly regulates melanosome transport, I isolated melanosomes from the aggregated cell state in the presence of commercially available, exogenous, and constitutively active PKA (catalytic subunit from bovine heart). In fact, I observed a significant increase in transport events from 5% (aggregated state, Figure 12,

orange bar) to 12.3% in the presence of PKA (Figure 12, magenta bar; Table VI, Video 3). The commercially available PKA-specific inhibitor H-89 reversed this effect by PKA (Figure 12, purple bar; Table VI).

Taken together, I observed that the frequency of MyoVa-mediated transport events was higher with melanosomes from dispersed cells than with melanosomes from aggregated cells, pointing to a stronger involvement of MyoVa-transport in the dispersion process than in the aggregation process. Even more importantly, I showed that PKA is directly involved in regulation of MyoVa activity between more active during dispersion and lower activity during aggregation and this regulation occurs directly on the melanosome surface.

In contrast, the biophysical parameters of reactivated melanosome transport with dispersed cytoplasmic extract and exogenous PKA were again very similar (Figure 13, Table VII), suggesting that the transport properties of the motor do not alter between the respective cell states.
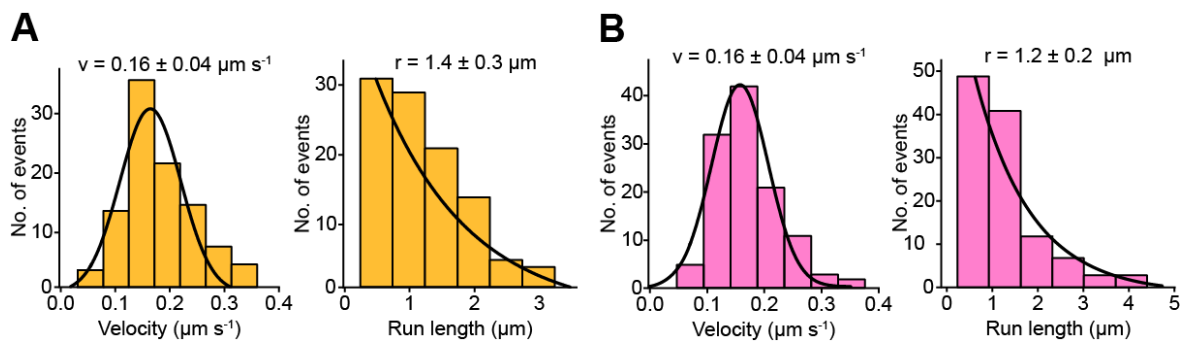
Figure 13: Reactivated melanosome transport exhibits similar kinetic transport parameters *in vitro* as active transport. Dormant melanosomes from aggregated cell states were purified and incubated with dispersed cytoplasmic extract (A, yellow) or constitutively active PKA (B, magenta), respectively. Velocities (v) and run lengths (r) are mean values ± SD deduced from the Gaussian (velocities) and single-exponential (run lengths) fit curves (solid lines) to the histogram data.

Table VII: Biophysical parameters of reactivated melanosome transport *in vitro*. Melanosomes were purified from the aggregated cell state and incubated with dispersed cytoplasmic extract or constitutively active PKA, respectively. Mean values ± SD were obtained as described in Figure 13.

	Velocity [μm/s] ± S.D.	Run length [μm] ± S.D.	Analyzed runs	Independent isolations
Aggr. + disp. CE	0.16 ± 0.04	1.4 ± 0.3	101	6
Aggr. + PKA	0.16 ± 0.04	1.2 ± 0.2	116	5

5.2 The tripartite MyoVa receptor complex is present on purified melanosomes from *Xenopus laevis*

The organelle receptor complex for MyoVa in mouse melanocytes has been identified more than 10 years ago (39-44, 114-117). The membrane-bound small GTPase Rab27a recruits Mlph in a GTP-dependent manner that in turns binds MyoVa. For *Xenopus laevis* melanosomes it is not known yet whether MyoVa is bound to the organelle in a similar way. To show that a similar complex is formed also on the melanosomes from *Xenopus*, I performed immunoblots with purified melanosomes and commercially available antibodies against Rab27a, Mlph, and MyoVa. Figure 14 A depicts the presence of the entire MyoVa tripartite transport complex, as identified in mouse melanocytes, on *Xenopus laevis* melanosomes. Further, the catalytic subunit of PKA is bound to melanosomes (Figure 14 A), which directly regulates MyoVa-driven melanosome transport on actin *in vitro* (Figure 12). PKA was previously shown to be present on melanosomes and form complexes with motor proteins on *Xenopus* melanosomes (51, 52).
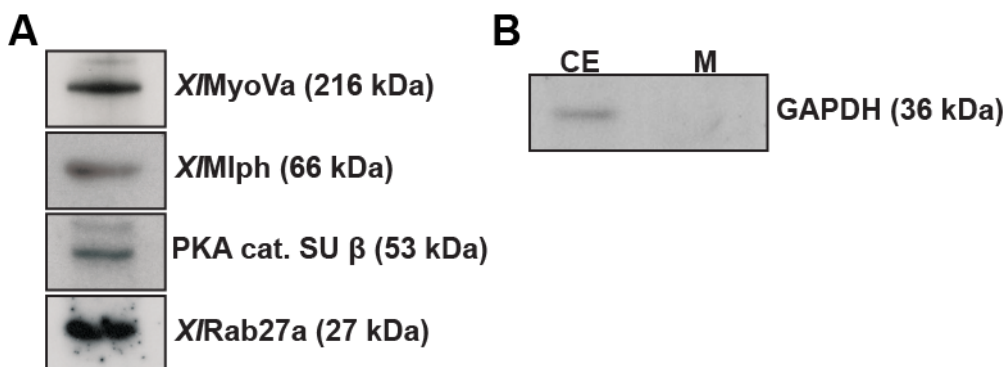
Figure 14: Rab27a, Mlph, MyoVa, and the catalytic subunit β (cat. SU β) of PKA are present on purified melanosomes. (A) Immunoblots of a purified melanosome fraction demonstrate that Rab27a, Mlph, and MyoVa presumably build the tripartite complex in *Xenopus* as well and compounds stay attached during isolation procedure. Furthermore, PKA, which orchestrates actin-based transport, is bound to melanosomes. (B) Glyceraldehyde 3-phosphate dehydrogenase (GAPDH) is detected in the cytoplasmic extract (CE), but not in the purified melanosome fraction (M). The absence of the housekeeping protein GAPDH from melanosome fraction demonstrates that cytosolic components are separated from melanosomes and melanosomes do not contain cytoplasmic contaminations.

To test for cytosolic contaminations, melanosomes were blotted with an antibody against glyceraldehyde 3-phosphate dehydrogenase (GAPDH), which is stably and constitutively expressed at high levels in the cytosol. GAPDH is detected in the cytoplasmic extract (i.e. melanophore cytoplasm), but not in purified melanosomes, indicating that cytosolic components are well separated from melanosomes during the purification procedure.

Collectively, these results indicate for the first time that in *Xenopus laevis* – as shown previously in mouse melanocytes – MyoVa is recruited to the melanosome via Rab27a and Mlph.

5.3 Building the tripartite MyoVa receptor complex *in vitro*

The here presented reconstitution of the MyoVa-based transport of *Xenopus laevis* melanosomes revealed that PKA directly regulates MyoVa-driven transport. So far, it is known that PKA orchestrates the direction of melanosome transport (57), but the molecular mechanism is entirely ambiguous and the downstream target(s) of PKA remain unidentified. As PKA directly affects transport driven by MyoVa, one possibility could be that MyoVa or one of the adaptor proteins (Rab27a or Mlph) is phosphorylated by PKA. To examine whether a member of the MyoVa receptor complex is a direct target of PKA, I recombinantly expressed the three proteins from *Xenopus* – Rab27a, Mlph, and MyoVa – to investigate them *in vitro*. Additionally, I also expressed Rab27a, Mlph, and MyoVa from *Mus musculus* to additionally check possible (PKA) phosphorylation in a distantly related species. Figure 15 A depicts the tripartite MyoVa receptor complex and its melanosome association. Domain structures of Rab27a, Mlph, and MyoVa are illustrated in Figure 15 B.
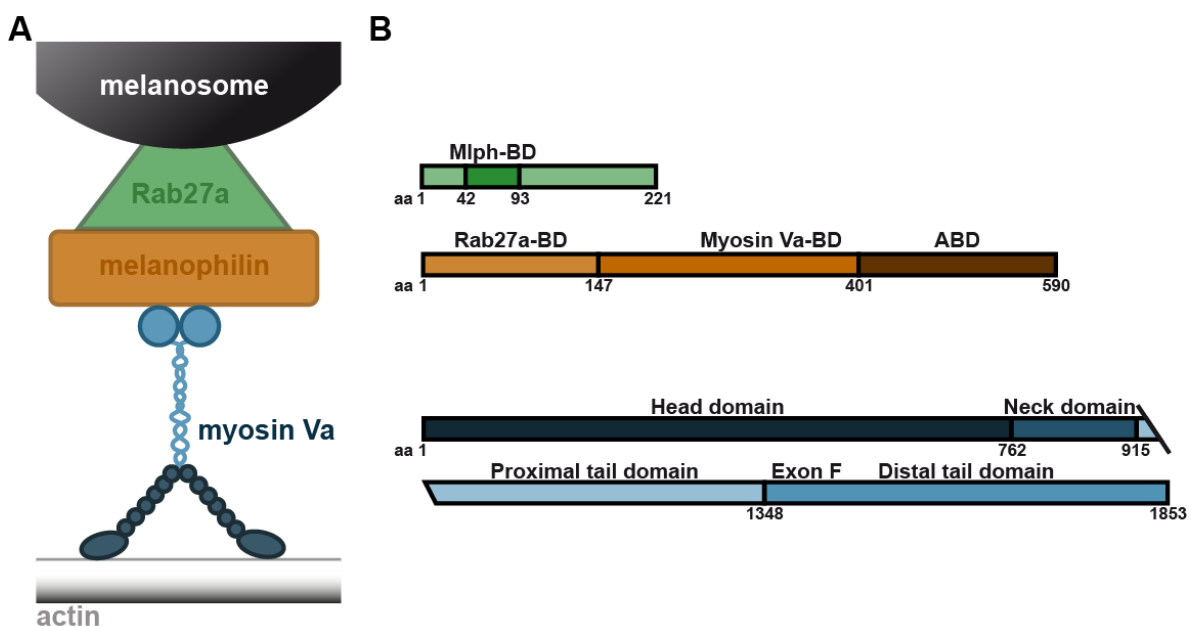
Figure 15: Schematic illustration of the MyoVa receptor complex on melanosomes in mouse melanocytes. (A) MyoVa is attached to the melanosome via the adaptor protein Mlph, which in turn binds to the membrane-bound Rab27a. (B) Schematic diagram of protein domain structures of Rab27a, Mlph, and MyoVa. The small GTPase Rab27a, which consists of 221 aa (27 kDa), resides in the melanosome membrane and binds to Mlph via its N-terminal effector binding domain (Mlph-BD). The 66 kDa large Mlph contains an N-terminal Rab27a-binding domain (Rab27a-BD), followed

by a MyoVa-binding domain (MyoVa-BD). The C-terminal part of Mlph (actin-binding domain: ABD) interacts with actin filaments and EB1 (48-50) but also with MTs as demonstrated in this work. MyoVa is a large 216 kDa protein that homodimerizes to build the double-headed actin-based motor protein. It consists of a head domain that binds to actin and hydrolyzes ATP, a neck domain with six IQ motifs, a proximal tail domain that forms coiled-coils for dimerization, and the C-terminal distal tail domain that forms the globular tail domain and is thought to mediate cargo binding. Exon F, which is essential for Mlph binding, is located in the distal tail domain.

Previous work on mouse melanocytes and mouse proteins has uncovered detailed information about the protein interactions within the MyoVa receptor complex (43, 45, 46, 49, 118, 119). It has been shown that Mlph binds to Rab27a's N-terminal effector binding domain in a GTP-dependent manner. The Mlph-MyoVa interaction occurs between Mlph's MyoVa-binding domain and the globular tail domain of MyoVa at its C-terminus. This interaction is dependent on exon F, a short sequence specific for the melanocyte isoform of MyoVa (47), which is located in the globular tail domain of MyoVa. Until now, molecular details of the MyoVa receptor complex in amphibians await clarification.

5.3.1   Generation of constructs

For individual expression and subsequent coexpression and assembly of the entire tripartite complex, as well as for *in vitro* experiments, all three subunits were expressed using the baculovirus system. Differently tagged constructs used in this study were either generated by PCR (for details see section 4.2.1.1; overview of *Xenopus* constructs is shown in Figure 16) or commercially synthesized (for details see section 4.2.1.8). All constructs were cloned into the baculovirus-compatible transfer vector plasmid pFastBac^{TM}1 downstream of the Polyhedrin promoter (P$_{PH}$) via restriction enzyme-mediated cloning.

An overview of generated constructs from *Xenopus* is presented in Figure 16. *Xl*Rab27a was used with a C-terminal FLAG-tag for purification. Furthermore, a GDP-mimic (*Xl*Rab27a-T23N) and a GTP-mimic (*Xl*Rab27a-Q78L) of Rab27a (46) with a FLAG-tag at the C-terminus were employed in this study. For the purpose of assembling the tripartite complex, a C-terminally SNAP- and 6XHis-tagged GTP-mimic Rab27a was generated.
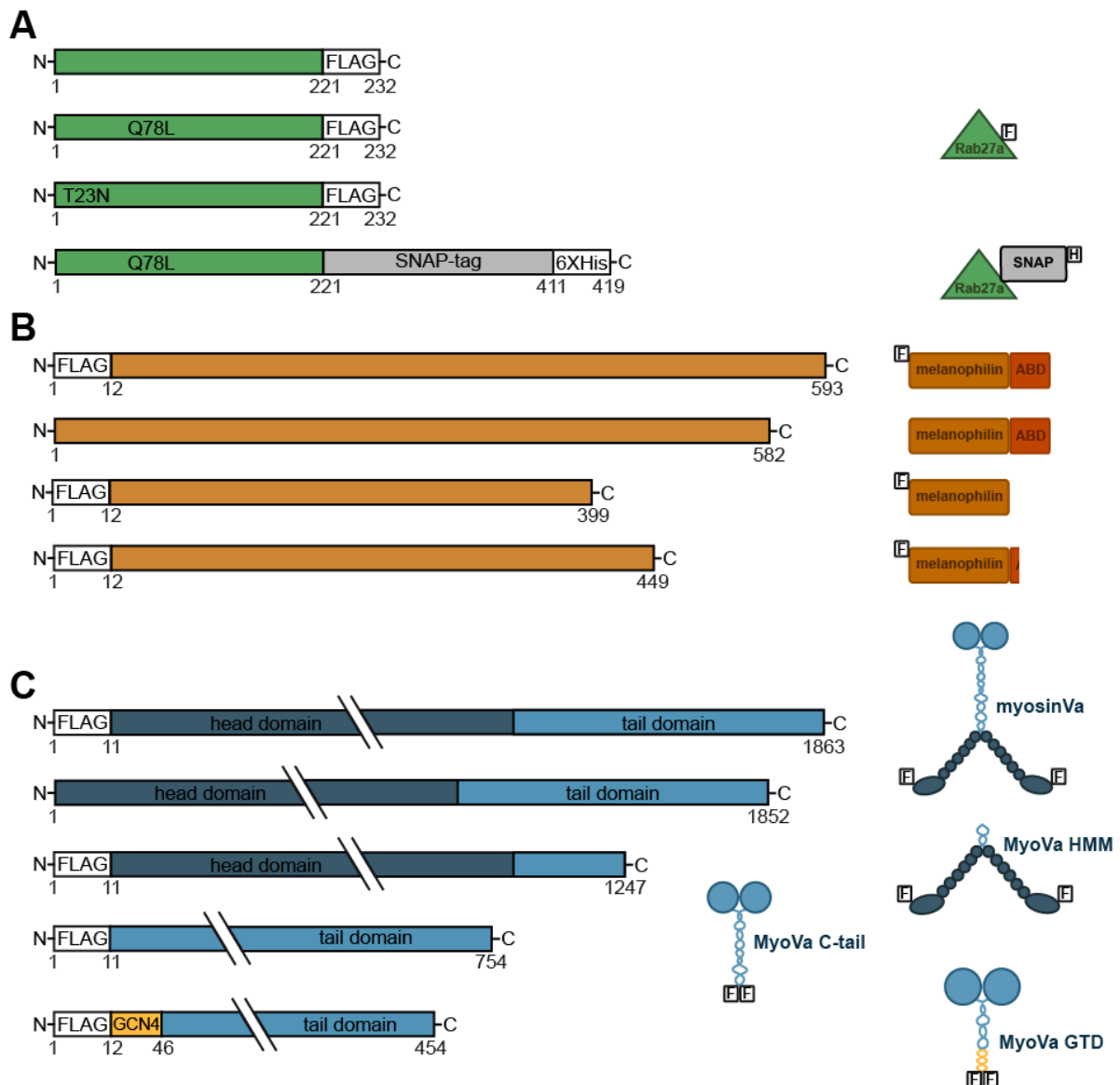
Figure 16: Overview of generated constructs from *Xenopus laevis/tropicalis* employed in this study. (A) Rab27a from *Xenopus laevis* was C-terminally tagged with FLAG, or SNAP-6XHis. The point mutated Rab27a-Q78L or Rab27a-T23N constructs were used as GTP- or GDP-bound mimic, respectively. (B) Mlph was used untagged or N-terminally FLAG-tagged. C-terminally truncated Mlph constructs containing amino acids 1-388 (Mlph ΔABD) or 1-438 were generated via PCR and FLAG-tagged at the N-terminus. (C) Full length MyoVa was used untagged or N-terminally FLAG-tagged. The C-terminally truncated construct MyoVa HMM (residues 1-1237), the N-terminally truncated constructs MyoVa C-tail (residues 1110-1852) and MyoVa GTD (residues 1445-1852) with a N-terminal GCN4 leucine zipper for dimerization were employed in this thesis.

Untagged and N-terminally FLAG-tagged wild type *Xt*Mlph constructs were obtained by PCR with custom-made primers (for details see section 3.7.1 and 4.2.1). N-terminally FLAG-tagged *Xt*Mlph constructs lacking the C-terminal ABD (*Xt*Mlph ΔABD (1-388) and *Xt*Mlph 1-438) were generated by PCR with custom-made primers. *Xl*MyoVa was used with a N-terminal FLAG-tag. *Drosophila melanogaster* calmodulin was always coexpressed with *Xl*MyoVa to ensure motor functionality. The N-terminally FLAG-tagged truncation

constructs *Xl*MyoVa HMM (aa 1-1237) and *Xl*MyoVa C-tail (aa 1110-1852) were generated by PCR with custom-made primers. N-terminally FLAG-tagged *Xl*MyoVa GTD (aa 1445-1852) that only contains the globular tail domain of MyoVa without exon F was fused to the molecular zipper GCN4 to ensure dimerization and commercially synthesized.

*Mm*Rab27a and *Mm*Rab27a-Q78L with a C-terminal SNAP tag followed by a 6XHis-tag, wild type *Mm*Mlph with a N-terminal FLAG-tag, *Mm*MyoVa with an N-terminal FLAG-tag, and untagged *Mus musculus* calmodulin were commercially synthesized and used for respective experiments. The C-terminally truncated *Mm*Mlph constructs *Mm*Mlph ΔABD (1-400) and *Mm*Mlph 1-440 with an N-terminal FLAG-tag were obtained by performing PCR with custom-made primers. The C-terminally truncated construct *Mm*MyoVa HMM (aa 1-1109) was generated by PCR. As *Xenopus* and mouse Rab27a, Mlph, and MyoVa share the same domain organization and exhibit only minor differences in residues number please refer to Figure 16 as a construct overview.

5.3.2   Purification of *Xl*Rab27a, *Xt*Mlph, and *Xl*MyoVa

All proteins were expressed in Sf9 cells and purified as described in section 4.3.5. *Xl*Rab27a-Q78L^{S-H} was further purified with ion exchange chromatography (see section 4.3.9.1). Eluted proteins are depicted in Figure 17. Immediately after purification, purified proteins were aliquoted, flash-frozen in liquid nitrogen, and stored at -80° C. For experiments, protein aliquots were quickly thawed, kept on ice and used within a few hours.

A

B

C

D

E
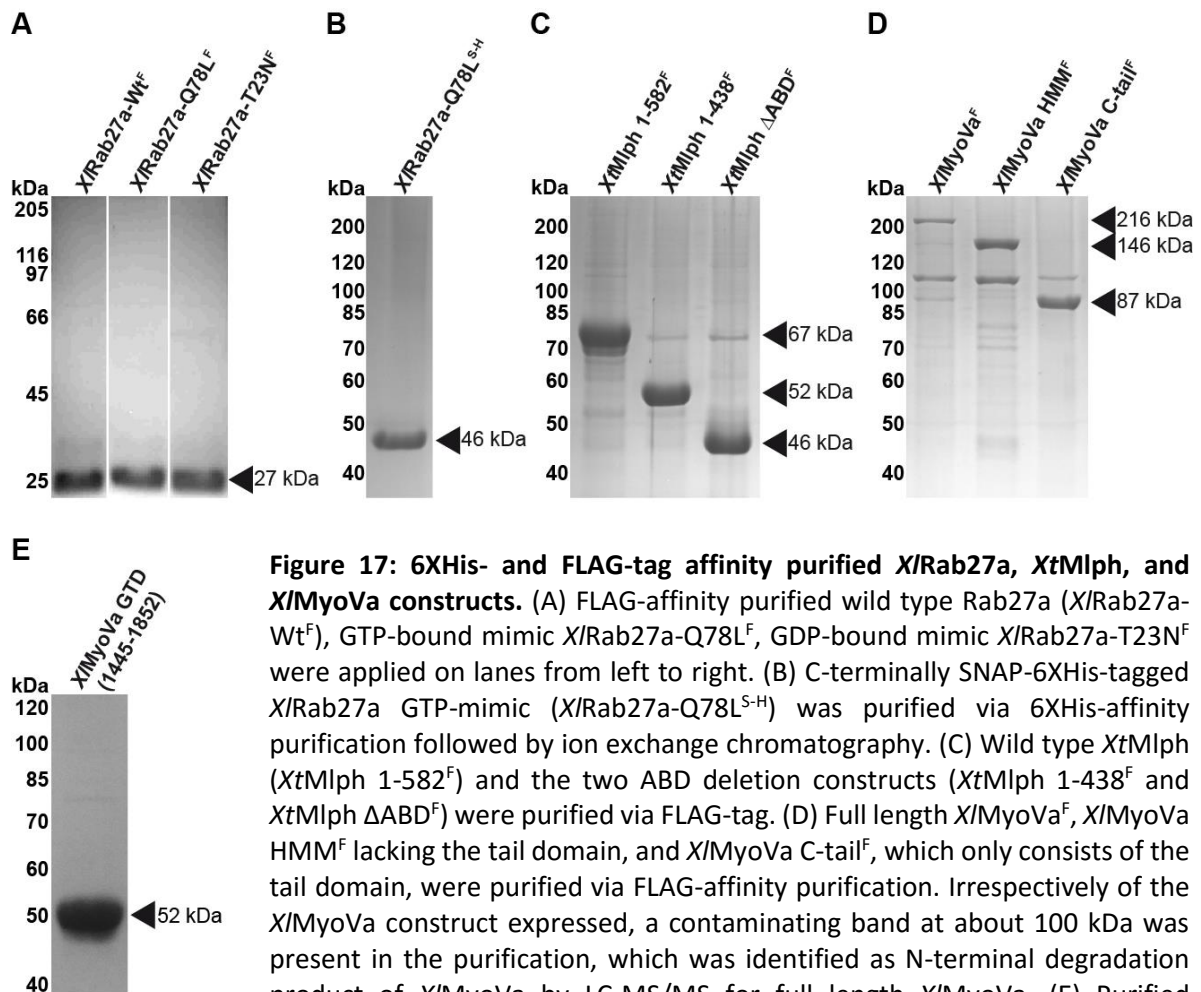
Figure 17: 6XHis- and FLAG-tag affinity purified *Xl*Rab27a, *Xt*Mlph, and *Xl*MyoVa constructs. (A) FLAG-affinity purified wild type Rab27a (*Xl*Rab27a-Wt[F]), GTP-bound mimic *Xl*Rab27a-Q78L[F], GDP-bound mimic *Xl*Rab27a-T23N[F] were applied on lanes from left to right. (B) C-terminally SNAP-6XHis-tagged *Xl*Rab27a GTP-mimic (*Xl*Rab27a-Q78L[S-H]) was purified via 6XHis-affinity purification followed by ion exchange chromatography. (C) Wild type *Xt*Mlph (*Xt*Mlph 1-582[F]) and the two ABD deletion constructs (*Xt*Mlph 1-438[F] and *Xt*Mlph ΔABD[F]) were purified via FLAG-tag. (D) Full length *Xl*MyoVa[F], *Xl*MyoVa HMM[F] lacking the tail domain, and *Xl*MyoVa C-tail[F], which only consists of the tail domain, were purified via FLAG-affinity purification. Irrespectively of the *Xl*MyoVa construct expressed, a contaminating band at about 100 kDa was present in the purification, which was identified as N-terminal degradation product of *Xl*MyoVa by LC-MS/MS for full length *Xl*MyoVa. (E) Purified *Xl*MyoVa GTD containing the globular tail domain without exon F and N-terminally fused GCN4 zipper for dimerization. Images show 10% SDS-PAGE gels. Approximate molecular weights of the constructs are indicated on the right side of each gel image.

Under our laboratory conditions, *Xt*Mlph 1-583[F] appeared at a higher molecular weight as the theoretically calculated molecular weight, as noticed before for mammalian Mlph by others (117, 118, 120).

5.3.3 Purification of *Mm*Rab27a, *Mm*Mlph, and *Mm*MyoVa

Proteins from *Mus musculus* were essentially purified as described for *Xenopus laevis* proteins (section 5.3.2) and representative purifications are presented in Figure 18. The discrepancy between the theoretical molecular weight of all Mlph constructs from mouse and the molecular weight apparent from SDS-PAGE was pronounced.
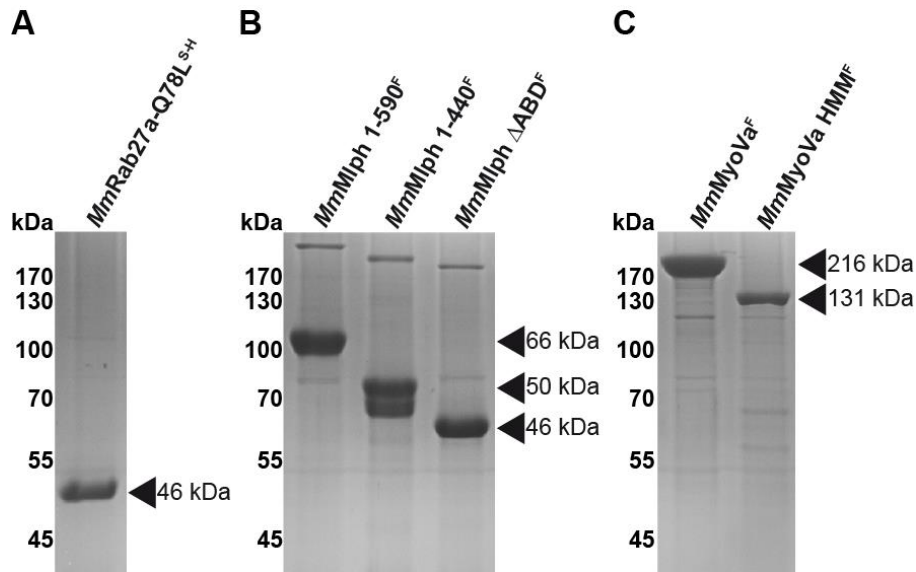
Figure 18: 6XHis- and FLAG-tag affinity purified Rab27a, Mlph, and MyoVa from *Mus musculus*.
(A) *Mm*Rab27a^{S-H} was purified via 6XHis-tag followed by ion exchange chromatography. (B) Wild type *Mm*Mlph (*Mm*Mlph 1-590^F) and the two ABD deletion mutants (*Mm*Mlph 1-440^F and *Mm*Mlph ΔABD^F) were purified via FLAG-tag affinity purification. (C) Full length *Mm*MyoVa^F and the construct lacking the tail domain *Mm*MyoVa HMM^F were purified via the N-terminal FLAG-tag. Images show 10% SDS-PAGE gels. Approximate molecular weights of the constructs are indicated on the right side of each gel image.

*Mm*MyoVa is purified in very high quantities compared to MyoVa from *Xenopus laevis.*

5.3.4   Recombinantly expressed *Xl*MyoVa forms a dimeric motor

I used the full length MyoVa from *Xenopus laevis* that was previously cloned and characterized by Dennis Zimmermann (90).
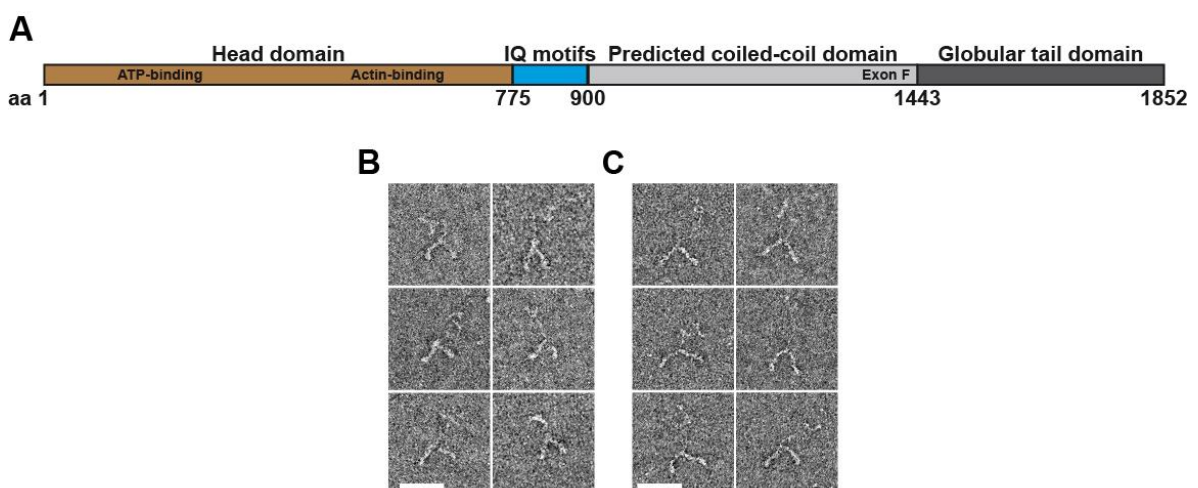
Figure 19: Recombinantly expressed full length *Xl*MyoVa forms a dimeric motor. (A) Predicted domain organization of *Xl*MyoVa. The N-terminal catalytic head domain containing the ATP- and actin-binding sites is followed by six IQ motifs. The stalk is composed of a predicted coiled-coil region, whereas the C-terminus forms the globular tail domain that mediates cargo binding. (B)

Negative-staining transmission electron micrographs of *Xl*MyoVa motor proteins revealed the typical appearance of a motor protein with two motor heads and a stalk domain that appears as a slender rod (n=394). (C) Negative-staining electron micrographs of the dimeric *Mm*MyoVa motor are shown for comparison (n=804). Scale bar: 50 nm.

As *Xl*MyoVa is expressed in small quantities and object to protein degradation, it was not possible to employ size exclusion chromatography to confirm homodimerization of *Xl*MyoVa. Therefore, negative-staining transmission electron microscopy in cooperation with Evi Meier and Hendrik Dietz (Technische Universität München, Munich, Germany) was chosen to examine whether MyoVa from *Xenopus laevis* assembles into a dimeric motor. Figure 19 B clearly demonstrates the formation of *Xl*MyoVa homodimers that closely resemble the appearance of the well characterized homodimeric motor protein *Mm*MyoVa (Figure 19 C).

5.3.5   *Xt*Mlph binds to *Xl*Rab27a in a GTP-dependent manner

The adaptor protein Mlph that links MyoVa to Rab27a was the last member of the MyoVa receptor complex to be discovered in the mouse system 2002 (40-44, 49, 115). To date, the Mlph sequence is only known for *Xenopus tropicalis* (NCBI Reference Sequence: NP_001120194.1), a close relative to *Xenopus laevis*. As sequence information on *Xl*Mlph is not yet available, I worked with Mlph from *Xenopus tropicalis*.

The first step toward building the tripartite complex was to establish the binding between Rab27a and Mlph. After successful single expressions of both proteins (Figure 17 A and C), the Rab27a/Mlph protein complex could be obtained by simply coexpressing FLAG-tagged wild type Rab27a and untagged Mlph in Sf9 cells and subsequent FLAG-tag affinity purification (Figure 20, lane I). Coimmunoprecipitations with GTP- and GDP-mimicking point mutants of *Xl*Rab27a (*Xl*Rab27a-Q78L[F] and *Xl*Rab27a-T23N[F]) and untagged *Xt*Mlph revealed the GTP-dependence of this interaction (Figure 20, lane II and III).
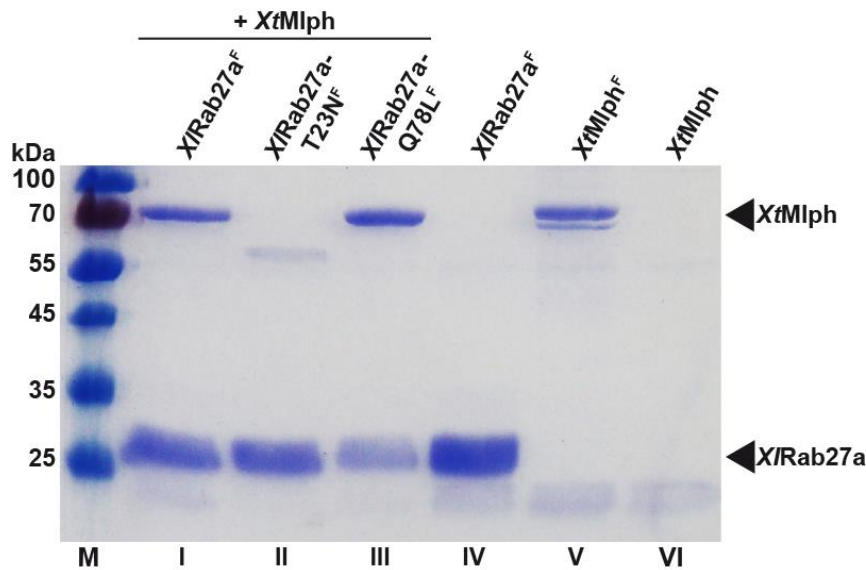
Figure 20: GTP-dependent binding of *Xt*Mlph to *Xl*Rab27a. Untagged, wild type *Xt*Mlph coprecipitates with FLAG-tagged wild type *Xl*Rab27a[F] (I) and with a constitutively active Rab27a mutant (*Xl*Rab27a-Q78L[F]; III), but not with the mutant mimicking the GDP-bound state (*Xl*Rab27a-T23N[F]; II). Lanes IV and V show FLAG-tag purified *Xl*Rab27a[F] and *Xt*Mlph[F] proteins, respectively, for comparison. To control for unspecific binding to the FLAG affinity resin, untagged *Xt*Mlph was expressed and subjected to FLAG-tag affinity purification as above (VI). M: molecular weight marker.

*Xl*Rab27a and *Xt*Mlph are able to interact *in vitro* and this interaction is exclusively GTP-dependent, similar to results obtained in *Mus musculus* (11, 42, 45, 121). Thus *Xl*Rab27a and *Xt*Mlph can be used for building the tripartite complex *in vitro*.

5.3.6 Reconstitution of the tripartite MyoVa receptor complex *in vitro*

Until today, no direct biochemical data (i.e. SDS-PAGE) has been published showing the reconstituted tripartite complex, consisting of Rab27a, Mlph, and MyoVa subunits.

As the most straightforward way of assembling the entire tripartite MyoVa receptor complex, I coexpressed the three subunits Rab27a, Mlph, and MyoVa that were differently tagged or untagged, respectively. Subsequent FLAG-tag affinity purification only yielded in Rab27a and Mlph for the *Xenopus* proteins and Mlph and MyoVa for the proteins from mouse.
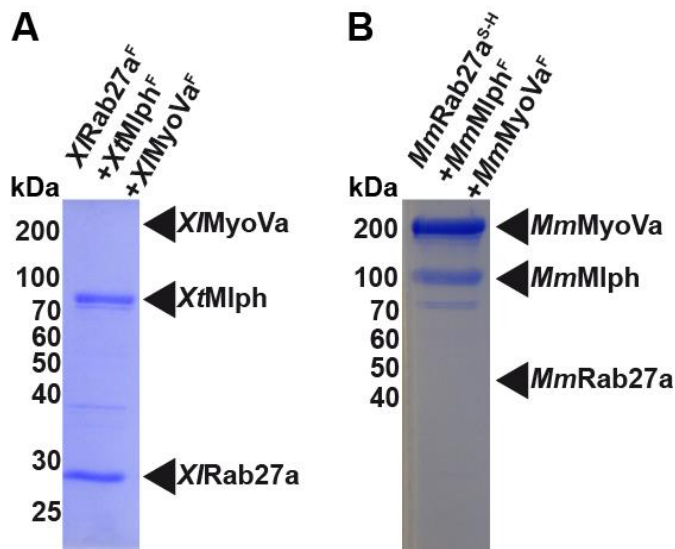
Figure 21: Coexpression of all three members of the tripartite complex from *Xenopus* and mouse only yields in expression of two subunits. (A) Coexpression of *Xl*Rab27a[F], *Xt*Mlph[F], and *Xl*MyoVa[F] that were all equipped with a FLAG-tag and subsequent FLAG-affinity purification resulted in the purification of only *Xl*Rab27a and *Xt*Mlph. (B) SNAP- and 6XHis-tagged *Mm*Rab27a[S-H] was coexpressed with FLAG-tagged *Mm*Mlph[F] and *Mm*MyoVa[F] and FLAG-affinity purified. Only *Mm*Mlph and *Mm*MyoVa were present in the elution.

Even coexpression of all three subunits with a FLAG-tag underscored the result that *Xl*MyoVa was not coexpressed together with *Xl*Rab27a and *Xt*Mlph (Figure 21 A). *Mm*Rab27a is not expressed when it was coexpressed with *Mm*MyoVa (Figure 21 B). Next, I attempted to purify the Rab27a/Mlph complex and subsequently add separately purified MyoVa like Wu et al. who successfully formed the tripartite complex *in vitro* (115) by mixing preassembled Rab27a/Mlph complex with separately purified MyoVa. They observed movement of the fluorescently labeled Rab27a subunit on actin filaments indicating the presence of both Mlph and MyoVa. It turned out to work best when 6XHis-tagged Rab27a and FLAG-tagged Mlph were coexpressed and tandem purified via Ni-NTA-affinity purification followed by FLAG-tag affinity purification (Figure 22, lane I). This preformed complex was reattached to Ni-NTA beads and separately FLAG-tag affinity purified MyoVa (Figure 22, lane II) was incubated with Rab27a/Mlph-covered beads. This way it was possible to elute the entire MyoVa receptor complex and analyze it with SDS-PAGE (Figure 22, lane III). Mlph and MyoVa are present in substoichiometric amounts compared to Rab27a.
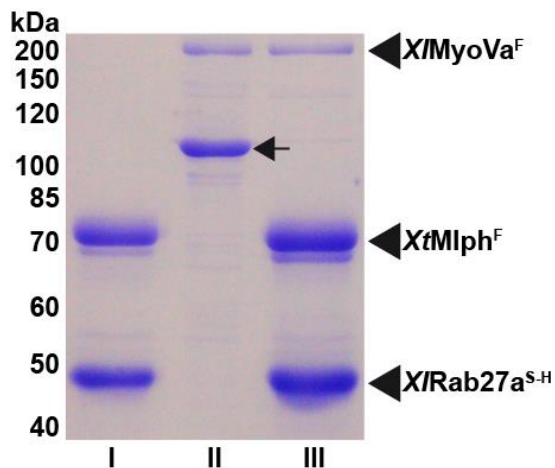
Figure 22: Reconstitution of the tripartite complex from recombinantly expressed full length *Xl*Rab27a, *Xt*Mlph, and *Xl*MyoVa proteins. (I) Tandem purification of SNAP-6XHis-tagged *Xl*Rab27a^{S-H} and FLAG-tagged *Xt*Mlph^F complex via Ni-NTA and FLAG affinity resin. (II) FLAG affinity purified full length *Xl*MyoVa^F. A lower molecular weight band (arrow) corresponds to an N-terminal degradation product of *Xl*MyoVa as assessed by LC-MS/MS. (III) A tripartite complex, reconstituted from a preformed *Xl*Rab27a^{S-H}/*Xt*Mlph^F complex and *Xl*MyoVa^F, could be purified by Ni-NTA affinity purification. Note that the N-terminal degradation product of *Xl*MyoVa^F seen in lane II (arrow) did not corporate into the complex.

To my knowledge, this is the first direct evidence that a tripartite MyoVa transport complex is also formed in amphibians and that MyoVa attachment to pigment granules is evolutionary conserved between amphibians and mammals.

5.3.7   Exon F is essential for the interaction between *Xt*Mlph and *Xl*MyoVa

Extensive investigations on the connection between Mlph and the motor protein MyoVa have been carried out in mouse. In mouse, MyoVa binds with its globular tail domain and exon F to the middle domain of Mlph. For this interaction, exon F is absolutely required *in vivo* in mouse melanocytes (33, 122, 123). Sequence alignment between *Mm*MyoVa and *Xl*MyoVa revealed that *Xl*MyoVa presumably contains exon F as the mouse protein does. The highly conserved region of exon F between *Xl*MyoVa and *Mm*MyoVa is shown in yellow (Figure 23 A). To test the potential exon F-dependence of the Mlph-MyoVa interaction in *Xenopus*, I used the purified Rab27a/Mlph complex and incubated it with either the purified *Xl*MyoVa C-tail (residues 1110-1852) that includes exon F or the purified *Xl*MyoVa GTD (residues 1445-1852) that excludes exon F, respectively.

A

```
              1 3 9 0     1 4 0 0     1 4 1 0     1 4 2 0     1 4 3 0     1 4 4 0
XlMyoVa  RIEASLQHEITRLTNENLFFEELYADEPMKYQSYRISLYRRIIDLMEQLEKQDKTVRKLK
MmMyoVa  RIEASLQHEITRLTNENLYFEELYADDPKKYQSYRISLYKRMIDLMEQLEKQDKTVRKLK
MmMyoVb  QVEFGVQQEISRLTNENLDFKEL----------------------VEKLEKNERKLK
Consensus ::* .:*:**:******* *:**                      :** :*. ****
```

B
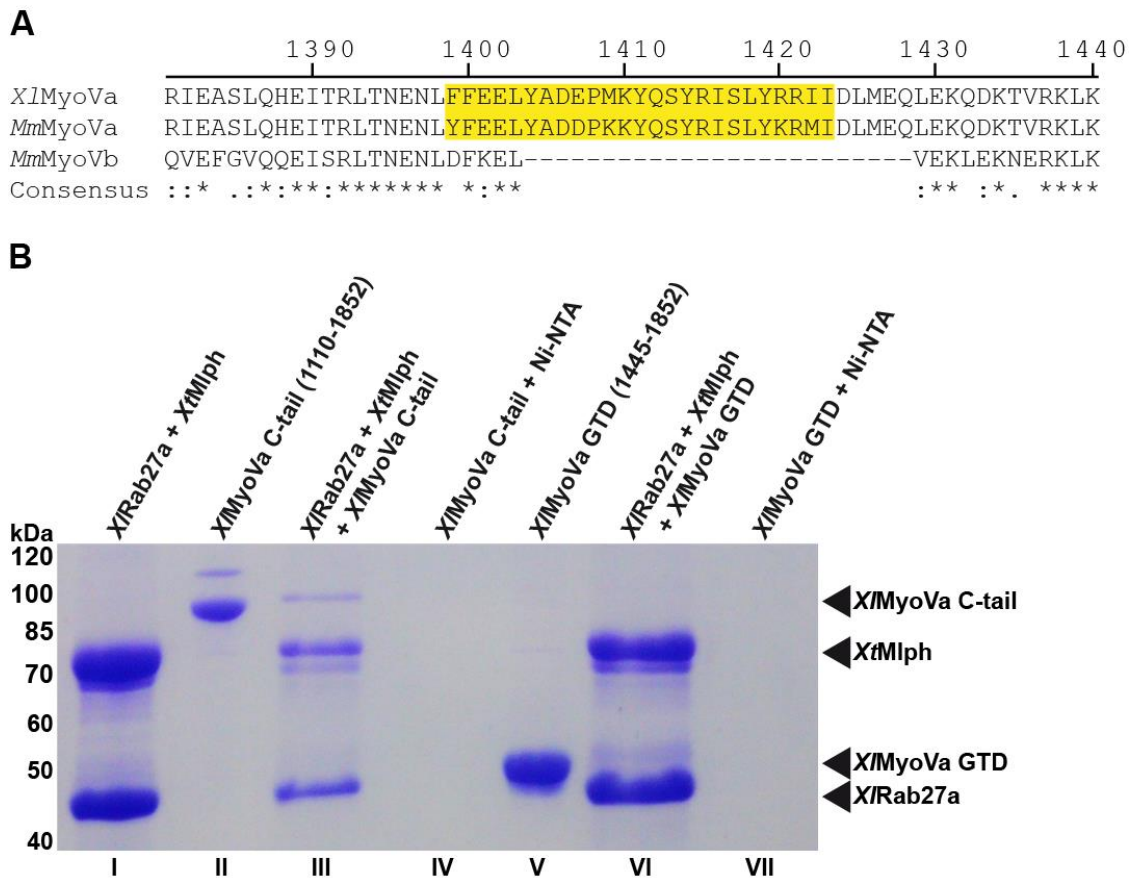
Figure 23: Sequence alignment of *Xl*MyoVa, *Mm*MyoVa, and *Mm*MyoVb proteins. Exon F in the *Mm*MyoVa and in the *Xl*MyoVa is highlighted in yellow. *Mm*MyoVb has a deletion of large parts of this region. Asterisks, colons and dots indicate positions that are fully, partially or weakly conserved, respectively. **(B)** ***Xl*MyoVa binds to the *Xl*Rab27a/*Xt*Mlph complex in an exon F-dependent manner.** Lane I shows the tandem purified *Xl*Rab27a/*Xt*Mlph complex. Lane II contains FLAG-purified *Xl*MyoVa C-tail possessing the exon F sequence. Lane III demonstrates that *Xl*MyoVa C-tail is able to bind to the preformed *Xl*Rab27a/*Xt*Mlph complex. Lane IV shows the purification of the FLAG-tagged *Xl*MyoVa C-tail via Ni-NTA resin as a control. Lane V shows the purified *Xl*MyoVa GTD via FLAG-tag. Lane VI demonstrates that the GTD that is devoid of exon F can no longer interact with *Xl*Rab27a/*Xt*Mlph complex. Lane VII contains a purification of the FLAG-tagged *Xl*MyoVa GTD via Ni-NTA resin as a control.

The *Xl*MyoVa C-tail construct containing exon F was capable of binding to the preformed Rab27a/Mlph complex (Figure 23, lane III), whereas *Xl*MyoVa GTD that lacks exon F did not interact with Mlph (Figure 23, lane VI).

Taken together, the interaction between Mlph and MyoVa in the amphibian *Xenopus laevis* takes place in the same way as shown for the mammalian system mouse, where exon F is essential for binding of MyoVa to Mlph.

5.4 The adaptor protein Mlph is the target of PKA

It is well established that PKA plays an important role in signal transduction governing intracellular melanosome transport in amphibian melanophores. Additionally, proteomic analyses of mouse melanoma cells identified numerous phosphorylated residues in all three subunits of the tripartite complex (124, 125). In particular, several conserved serine/threonine residues within Mlph's ABD that also represent potential cAMP-dependent protein kinase consensus sites were found to be phosphorylated *in vivo* (Figure 24) (126).

```
                380         390         400               410         420
           |...|....|....|....|....|....|....|....|....|....|....|....|....|....|
MmMlph     SADTEEETLRRRLEELTSNISGSSTS-SEDETKPD-----------GTFLGGSPKVCTDTG
HsMlph     EADVEEEALRRKLEELTSNVSDQETS-SEEEEAKDEKAEPNRDKSVGPLPQADPEVGTAAH
FdMlph     DADREEETLRRKLEELTCRVSDQDAS-SEEAGSEEEGSDLARSPSSQDLPGAAPEVCAAAG
ClMlph     DADVEEAALKRKLEELTSHISDQGVSSAEEEEGTDAGAEMGRSKTIEDHPGATWEVRTAAG
OaMlph     EADLEEERLRRKLQALTSGLSDQGAS-SEEEAARDAAA-----------GPSAEVCTAAG
XtMlph     DADIEEETLKRKLGELASNISDKGGSSDEEKISKPKSSHK------EPQTTETQKVYMAAE
Consensus  .** **  *:*:*  *:. :*..  *  *:                          :*   :

                430         440         450         460         470         480
           |...|....|....|....|....|....|....|....|....|....|....|....|....|....|
MmMlph     HMETQERNPRSPGNPARPTKSTDEELSEMEDRVAMTASEVQQAESEISDIQSRIAALRAAG
HsMlph     QTNRQEKSPQDPGDPVQYNRTTDEELSELEDRVAVTASEVQQAESEVSDIESRIAALRAAG
FdMlph     QTHGRDTTPWGPQDLVQPGRTTDEELLQLEDRVALTACEVQQVESEVSNIKSKIAALQAAG
ClMlph     QTPSWGKDLLSPGDPEQPSRTTEAELVELEGQVAATTREVRRTESQVSNIKSRIAALQAAG
OaMlph     RMDAWDSSPLGPGAPTVPRRTTDEALSELEDRVAAAASEVQQAESEVSDIESRIAALRAAG
XtMlph     KAYTLDKNLRDLEEHARQSGTTDSELSELEVSVASAIAQVQQTESEVSDIESRIAALSAAG
Consensus  :              .    :|*:  *  ::*   **  :   :*::.**::*:*:*:**** ***

                490         500         510         520         530         540
           |...|....|....|....|....|....|....|....|....|....|....|....|....|....|
MmMlph     LTVKPSGKPRRKSGIPIFLPRVTEKLDRIPKTPPADPDDQAKMPKATTAVPSLLRRKYSPS
HsMlph     LTVKPSGKPRRKSNLPIFLPRVAGKLGKRPEDPNADPSSEAKA----MAVPYLLRRKFSNS
FdMlph     LTVKPSGKPRRKSNLPIFLPRLAGSYDQRPKDPNAEPSDE------VTAPYLLRRKFSNS
ClMlph     LTVRPSGKPQRKSNLPIFLPRLVRKSDQSLKDPHADPSDEAKV----EAVPCLVRRKLSNY
OaMlph     LTVKPSVRPRRKSNLPIFLPRVARTPGKRLEGQNADPAEEGKA----AAAPCLLRGKYS--
XtMlph     MTVSPVDKAKRKSSSRVFAPAISRSTEPFQESTPDMYSMSSPSDAKILAMQQALRKKFNID
Consensus  :** *  :.:**|*|.  :* * :  .    :          :       :   :* * |*|

                550         560         570         580         590
           |...|....|....|....|....|....|....|....|....|....|....|
MmMlph     --SQGVDSGSFD-RKSVYRGSLTQRNPNGRRGTARHIFAKPVMAQQP
HsMlph     LKSQGKDDDSFD-RKSVYRGSLTQRNPNARKGMASHTFAKPVVAHQS
FdMlph     PKSQGRAADSARPSASAYRGSLTQRNPNSRKGVAAHSFAKPVMTQQP
ClMlph     PKSQEKDDDSFS-RKSMYRGSLTQRNPNGRKRAANHSFAKPVMTHQP
OaMlph     PKAHGKDQESLE-QKSLYRGSLTQRSPSSRRGMARHIFAKPVMAQQP
XtMlph     PDAIDLPVEKSA----LYRGSLTQRNPNGKNRKADRIFSKPIVNQR-
Consensus  :        .     ********.*..:.  * : *:**:: ::
```
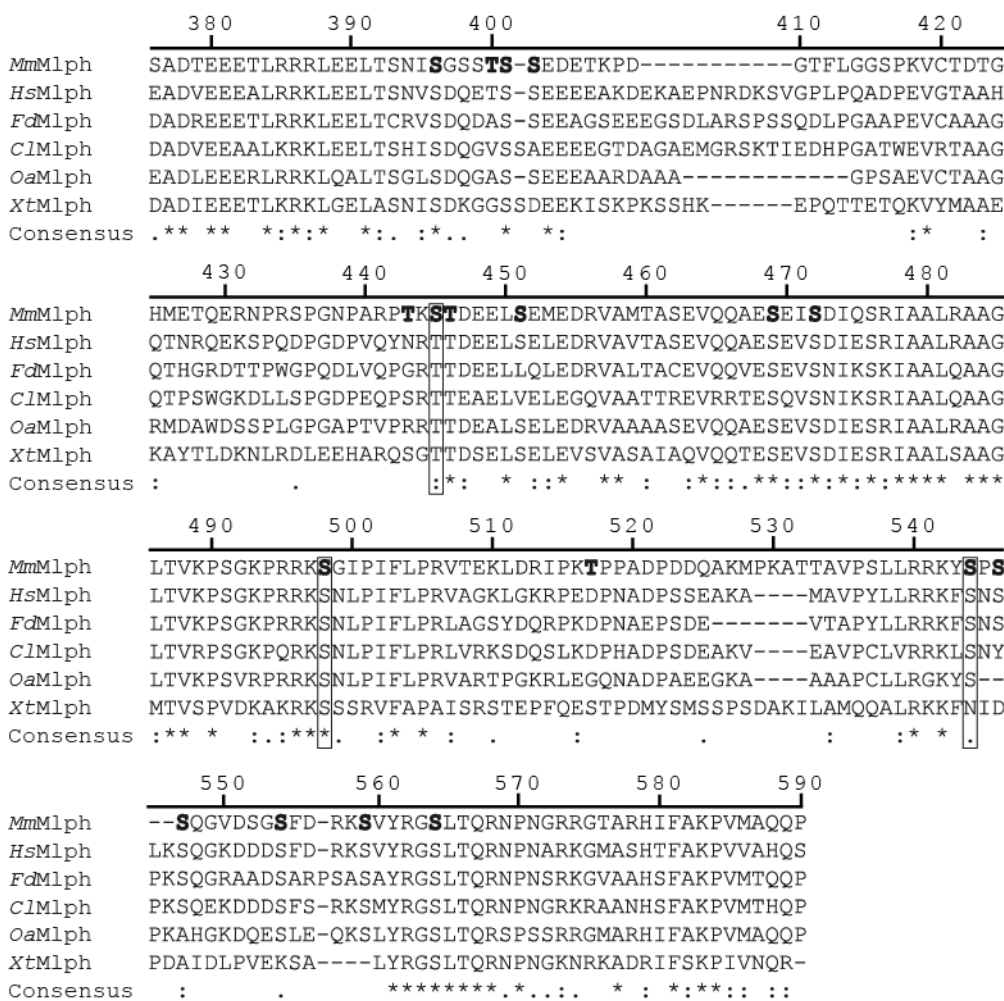
Figure 24: Alignment of Mlph ABDs from mouse (*Mm*), human (*Hs*), Fukomys (*Fd*), dog (*Cl*), sheep (*Oa*), and Xenopus (*Xt*). Sequence alignment of selected Mlph ABDs revealed numerous conserved serine/threonine residues that represent potential PKA targets. Serine and threonine residues that were found to be phosphorylated *in vivo* are in bold. Boxes indicate conserved phosphorylatable serine residues. Numbers represent the residue numbers according to *Mm*Mlph. Asterisks, colons and dots indicate positions that are fully, partially, or weakly conserved, respectively.

5.4.1   The ABD of Mlph is negligible for the interaction between Mlph and MyoVa

To investigate the functional importance of Mlph's ABD *in vitro*, I generated C-terminally truncated Mlph constructs that either lacked the entire or partial ABD. Both *Xenopus* and mouse wild type and truncated Mlph proteins were capable of reconstituting the tripartite complex *in vitro* (Figure 25) (127).
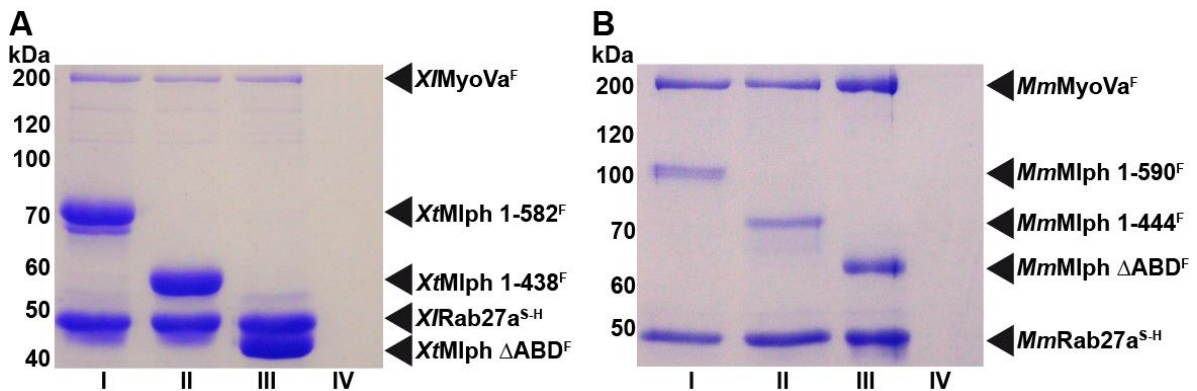

Figure 25: The ABD of Mlph is not involved in formation of the MyoVa receptor complex *in vitro*.
(A) Tripartite complexes reconstituted with *Xenopus* proteins. SNAP-6XHis-tagged *Xl*Rab27a^{S-H}, FLAG-tagged *Xl*MyoVa^F and FLAG-tagged full length (lane I) or C-terminally truncated *Xt*Mlph^F (lanes II, III) purified by Ni-NTA affinity purification as in Figure 22. As a control for non-specific binding, FLAG-tagged *Xl*MyoVa^F was also subjected to Ni-NTA affinity purification (lane IV). (B) Reconstitution of the tripartite complex from mouse as in (A) using the full length SNAP-6XHis-tagged *Mm*Rab27a^{S-H}, FLAG-tagged *Mm*MyoVa^F, and FLAG-tagged full length (I) or truncated (II-III) *Mm*Mlph^F subunits. As a control for non-specific binding, FLAG-tagged *Mm*MyoVa^F was subjected to Ni-NTA affinity purification (lane IV).

Taken together, removal of the ABD does not interfere with Mlph's protein structure and truncated Mlph proteins are still able to link MyoVa to Rab27a to fulfill their function as adaptor protein. Furthermore, the *in vitro* reconstitution of the tripartite complexes from *Xenopus* and mouse demonstrates that Rab27a, Mlph, and MyoVa are sufficient to form the MyoVa receptor complex in two distantly related species, arguing for a conserved mechanism of MyoVa recruitment to the melanosome.

5.4.2   *In vitro* phosphorylation assays with MyoVa receptor complex subunits

To test whether Mlph's ABD along with the other members of the tripartite complex are phosphorylated by PKA, a number of truncation constructs were used in addition to the wild type proteins. The two Mlph C-terminal truncation constructs that were still capable of recruiting MyoVa (Figure 25) were included to assess phosphorylation of the ABD. MyoVa is known to adapt an autoinhibited and folded conformation that might prevent effective phosphorylation (128-131). Therefore, I generated C-terminal (*Xl*MyoVa HMM,

residues 1-1237, and *Mm*MyoVa HMM, residues 1-1109) and N-terminal truncations of MyoVa (*Xl*MyoVa C-tail, residues 1110-1852) to exclude potential effects on phosphorylation.
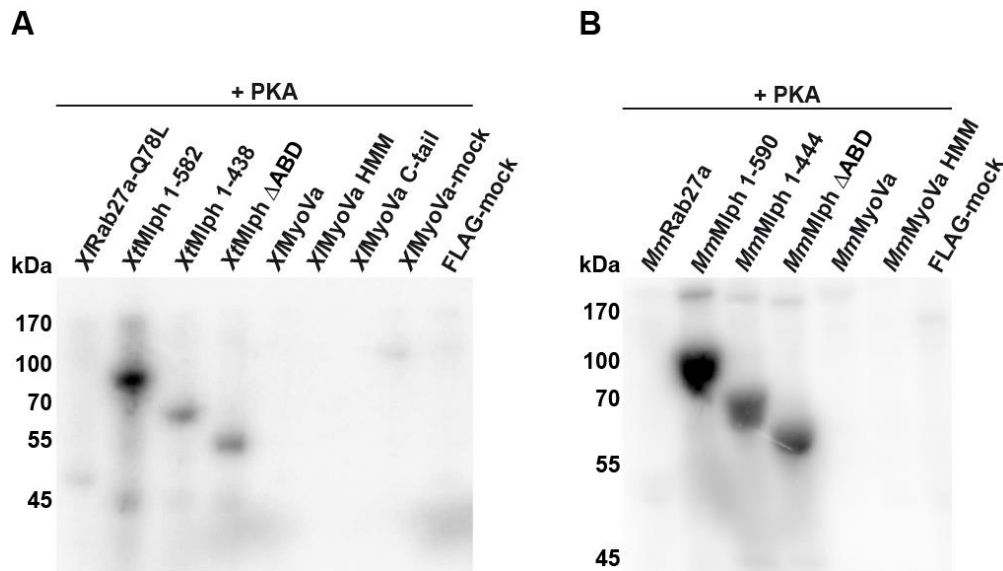

Figure 26: The Mlph subunit of the tripartite complex from *Xenopus* and mouse is specifically phosphorylated by PKA. (A) The subunits of the tripartite complex were treated with PKA and radiolabeled ATP. Autoradiography showed specific phosphorylation of *Xt*Mlph. Deletion of the C-terminus of Mlph decreased phosphorylation levels significantly. (B) Phosphorylation of the respective mouse subunits yielded in equivalent results.

In vitro phosphorylation assays with all individually expressed proteins described above, revealed that Mlph and its truncation constructs were the sole target of PKA (Figure 26) (127). In addition, I have assayed the MyoVa transport complex from mouse because there was no C-terminal portion (i.e. C-tail) available. Cargo (here: Mlph) binding was previously shown to release MyoVa from its folded inhibited conformation (120, 132).
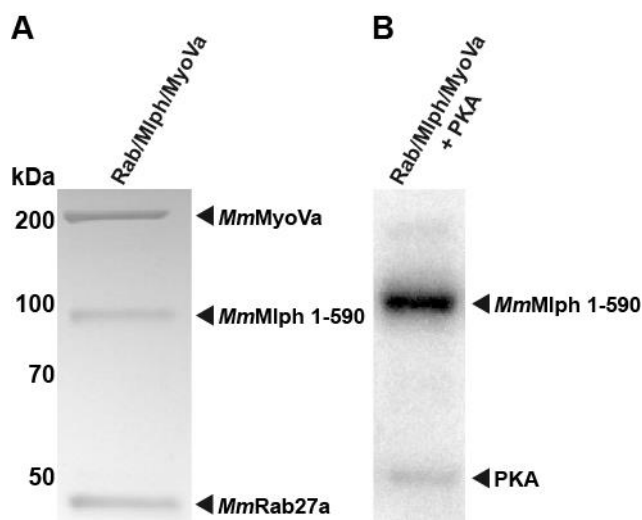

Figure 27: Mlph is the sole phosphorylation target of the reconstituted tripartite complex. (A) Coomassie-stained SDS-PAGE image of the reconstituted Rab27a/Mlph/MyoVa transport complex that was subjected to *in vitro* phosphorylation. (B) PKA specifically phosphorylated Mlph in the presence of Rab27a and MyoVa (autoradiograph).

Again, Mlph was phosphorylated by PKA, whereas Rab27a and MyoVa remained untargeted (127).

Importantly, the adaptor protein Mlph is the only target of PKA in both *Xenopus* and mouse, strongly indicating that this mechanism is evolutionary conserved. Furthermore, phosphorylation levels significantly dropped when the ABD was removed (Figure 26). Collectively, kinase assays with all subunits of the tripartite complex and PKA demonstrate that Mlph is specifically and directly targeted by PKA, especially its C-terminal ABD.

5.4.3   Mlph is an effective substrate of PKA

Time course experiments of PKA-dependent phosphorylation of Mlph demonstrated that Mlph, from both *Xenopus* and mouse, is an effective substrate for PKA and phosphorylation occurs fast (Figure 28). Saturation is reached within less than five minutes.
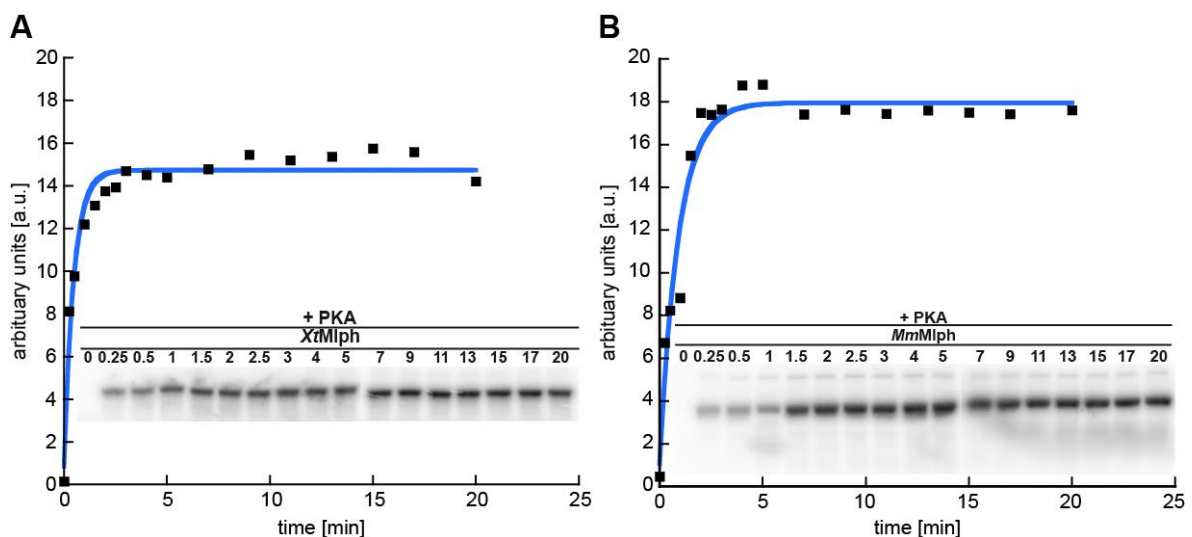

Figure 28: Time-dependent phosphorylation of *Xt*Mlph and *Mm*Mlph by PKA. (A) Phosphorylation time course of the recombinantly expressed *Xt*Mlph by PKA demonstrates that *Xt*Mlph is an effective substrate of PKA ($k = 2.1$ min^{-1}). (B) Phosphorylation time course as in (A) but with *Mm*Mlph ($k = 1.1$ min^{-1}). Both proteins show similar phosphorylation kinetics (A: 15.5 a.u. and B: 16.9 a.u.). Time courses were fitted to a single-exponential function.

Therefore, phosphorylation of Mlph by PKA takes place in a similar way in distantly related organisms.

5.4.4   *In vitro* phosphorylation resembles *in vivo* phosphorylation pattern

To identify phosphorylated residues and compare *in vivo* and *in vitro* phosphorylation patterns, I employed quantitative mass spectrometry analysis. The *in vitro* phosphorylation

by PKA resembled the previously known *in vivo* phosphorylation pattern remarkably well

(124, 125) (Table VIII).

Table VIII: Identification of phosphorylated residues and their quantification in the ABD of wild type *Mm*Mlph *in vitro*. The residues found to be phosphorylated in proteomic analyses are highlighted in bold letters as in Figure 24. The highly conserved residue S498 that also represents the most conserved cAMP-dependent protein kinase consensus site was quantitatively phosphorylated *in vitro*.

Modified amino acid	Localization probability	Phospho (STY) probabilities	Score	Occupancy
400	0.708	I**S**GSST(0.708)**SS**EDE	183	18.1%
401	0.949	**S**GSST**S**(0.949)**S**EDET	208	37.1%
416	0.999	TFLGGS(0.999)PKVCT	186	51.1%
435	1.00	ERNPRS(1.00)PGNPA	128	60.9%
443	0.386	NPARP**T**(0.386)K**ST**DE	51	ND
445	0.989	ARP**T**K**S**(0.989)**T**DEEL	122	18.9%
446	0.988	RP**T**K**ST**(0.988)DEEL**S**	92	8.46%
451	0.999	**T**DEEL**S**(0.999)EMEDR	214	26.9%
491	0.999	LTVKPS(0.999)GKPRR	145	ND
498	1.00	KPRRK**S**(1.00)GIPIF	150	99.7%
517	1.00	DRIPK**T**(1.00)PPADP	137	22.2%
537	0.999	TTAVPS(0.999)LLRRK	49	ND
544	0.999	LRRKY**S**(0.999)P**SS**QG	185	49.2%
546	0.836	RKY**S**P**S**(0.836)**S**QGVD	126	ND
554	0.994	GVDSG**S**(0.994)FDRK**S**	143	ND
559	0.972	**S**FDRK**S**(0.972)VYRG**S**	100	ND
564	0.982	**S**VYRG**S**(0.982)LTQRN	89	ND

ND, not detected.

The conserved and strong PKA-consensus site S498 contributed most to the overall phosphorylation within the ABD (Figure 24, Table VIII) (127). The close resemblance of the phosphorylation patterns *in vitro* and *in vivo* enabled me to test the functional consequences of Mlph phosphorylation *in vitro*. The following experiments were carried out employing the proteins from *Mus musculus*, because there is no *in vivo* phosphorylation pattern available for *Xt*Mlph or *Xl*Mlph.

5.5 PKA-dependent phosphorylation of Mlph does not interfere with MyoVa activity, actin binding or complex assembly

What function does Mlph phosphorylation serve? The following five scenarios are conceivable: (I) the phosphorylation alters MyoVa's activity and thereby regulates melanosome transport on F-actin, (II) the interaction between Mlph's ABD and actin is modulated by phosphorylation to bias transport direction, (III) motor protein (here: MyoVa) recruitment is changed in response to Mlph phosphorylation or in other words: phosphorylation of Mlph influences the stability of the tripartite transport complex, (IV) a yet unknown element is involved in regulation or (V) a combination of the possible scenarios described above accounts for the observed transport regulation.

The different motor proteins are indeed regulated as MyoVa was previously shown to be downregulated by ca. 50% and dynein is upregulated during aggregation in amphibian melanophores (73). How this is achieved is only partially known to date. The here performed *in vitro* motility assays with purified melanosomes (see section 5.1.3 PKA directly regulates MyoVa-driven melanosome transport *in vitro*) point to a mechanism different from motor activity regulation, because all biophysical transport parameters from active, inactive, and reactivated transport are similar.

5.5.1 Mlph phosphorylation does not affect MyoVa-based transport on F-actin *in vitro*

The first scenario posits that Mlph phosphorylation might alter the activity of the actin-based motor MyoVa. Single-molecule TIRF assays on surface-attached actin filaments were employed to test this hypothesis. For this purpose, the tripartite complex was assembled with Mlph lacking its ABD (Mlph ΔABD), phosphorylated (Mlph Phos) and dephosphorylated Mlph (Mlph Dephos) and fluorescently labeled on the Rab27a subunit. Velocities and run lengths of all three assembled complexes were determined on fluorescently labeled actin filaments in a TIRF microscope.

The velocities and run lengths of the respective MyoVa transport complex were independent of the presence or absence of the ABD (Figure 29 A-C) (127). Likewise, the transport parameters of the complexes assembled with phosphorylated or dephosphorylated Mlph were indistinguishable (Figure 29 B and C).

To conclude, phosphorylation of Mlph does not impact MyoVa-driven transport parameters like velocity and run length on actin filaments *in vitro*.
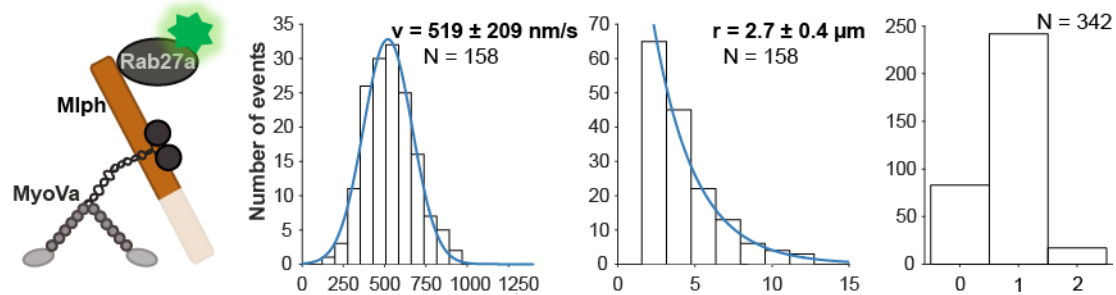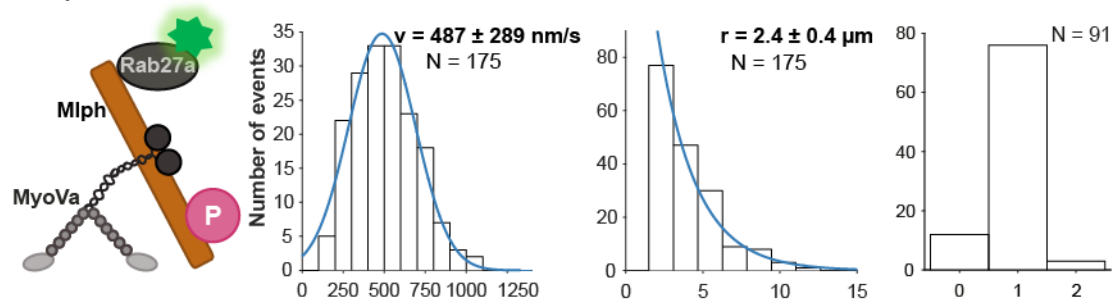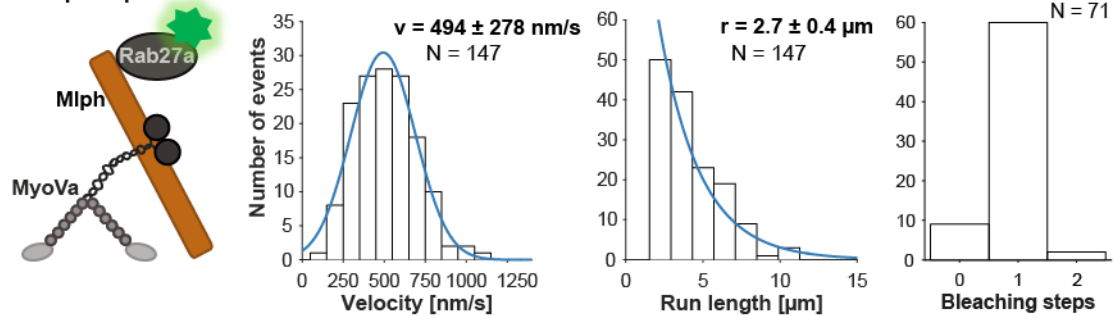

Figure 29: Transport parameters of the tripartite complex on surface-attached actin filaments in single-molecule TIRF assays. The tripartite complex assembled with Mlph that lacked its ABD (A) and the complexes assembled with phosphorylated (B) and dephosphorylated (C) Mlph, respectively, all moved at consistent velocities. The absence of ABD (A) or the phosphorylation state of the Mlph (B vs. C) did not interfere with the velocities and run lengths of the respective complexes. The majority of the complexes displayed a single-step photobleaching of the SNAP-tagged Rab27a subunit as shown in the right panels of A to C, demonstrating that the transport parameters are derived from single molecules of Rab27a.

5.5.2   Mlph phosphorylation does not impact actin binding

In 2002, it was first reported that Mlph is capable of binding to actin via its C-terminal ABD (49). Further studies supported this result and broadened the knowledge by demonstrating that a cluster of positively charged amino acids (K493, R495, R496, K497) is responsible for this interaction (37, 48). It was suggested that the positively charged residues in the ABD

interact with the negatively charged N-terminus of actin through electrostatic interactions (37). The here presented finding that Mlph is phosphorylated – in particular Mlph's ABD (Figure 26) – might suggest a phosphorylation-dependent regulation of this electrostatic interaction by reducing the net positive charge on Mlph's C-terminus. To test this hypothesis, fluorescently labeled *Mm*Rab27a-Q78L^{S-H} in complex with either dephosphorylated or phosphorylated *Mm*Mlph^F was subjected to *in vitro* filament decoration assays. Briefly, *Mm*Rab27a^{S-H} was coexpressed with *Mm*Mlph^F and tandem purified. Fluorescent labeling of the Rab27a subunit was performed while the complex was bound to Ni-NTA-beads, whereas dephosphorylation or phosphorylation was performed while protein complex was FLAG-resin bound. Phosphatase- or PKA-treated and fluorescently labeled Rab27a/Mlph complex (Alexa 647) was flushed into a flow chamber with surface-immobilized and fluorescently labeled actin filaments (Atto488) and decoration was imaged by TIRF microscopy.

Intriguingly, dephosphorylated as well as phosphorylated Mlph in complex with Rab27a decorated F-actin to an equivalent extent (Figure 30 A) (127). Mlph that lacked its ABD (*Mm*Mlph ΔABD) was no longer capable of interacting with actin filaments, regardless of its phosphorylation state (Figure 30 B).
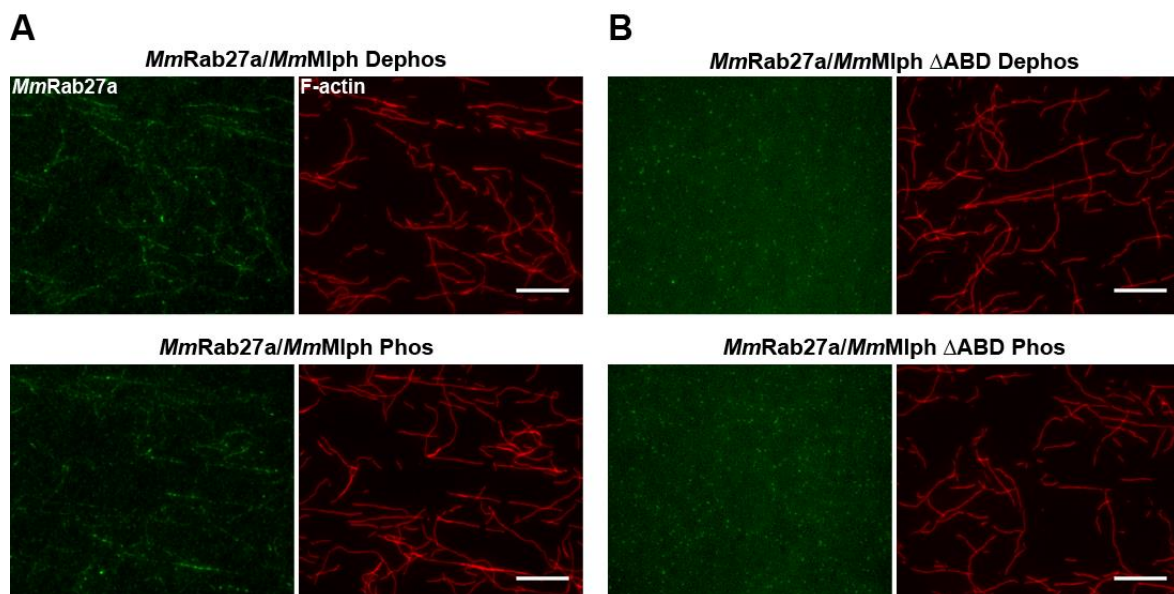

Figure 30: Mlph interacts with F-actin, but not in a phosphorylation-dependent manner. (A, B) Actin decoration experiments in which surface-immobilized fluorescently labeled F-actin (red channel) was incubated with a complex formed between Mlph and fluorescently labeled Rab27a (green channel). (A) Both the phosphorylated (Phos) and dephosphorylated (Dephos) Mlph

decorated F-actin similarly well. (B) Removal of the C-terminal ABD of Mlph inhibited this interaction regardless of the phosphorylation state. Scale bar: 10 μm.

To further verify that phosphorylation of Mlph did not impact its association with actin filaments, I performed decoration assays to quantify the intensities of the dephosphorylated and phosphorylated Rab27a/Mlph complexes associated with actin filaments in one flow chamber. For this purpose, the dephosphorylated Rab27a/Mlph complex was labeled with Alexa Fluor 488 and the phosphorylated complex was labeled with Alexa Fluor 647. Equal amounts of the differentially labeled, dephosphorylated and phosphorylated complexes were flowed into a single flow chamber with surface-adhered Atto565-labeled actin filaments and three-color TIRF microscopy was employed (Figure 31 A). Quantification of the actin-associated fluorescent intensities of the dephosphorylated and phosphorylated complex, respectively, demonstrated that both complexes bound to very similar extents to actin (Figure 31 A, right panel) (127). To exclude any effects of protein labeling, I swapped the colors of the complexes (i.e. dephosphorylated complex was labeled with Alexa Fluor 647 and the phosphorylated complex was labeled with Alexa Fluor 488, respectively) and the quantification yielded similar results (Figure 31 B).

Collectively, the phosphorylation state of Mlph does not influence its association with actin filaments *in vitro*.
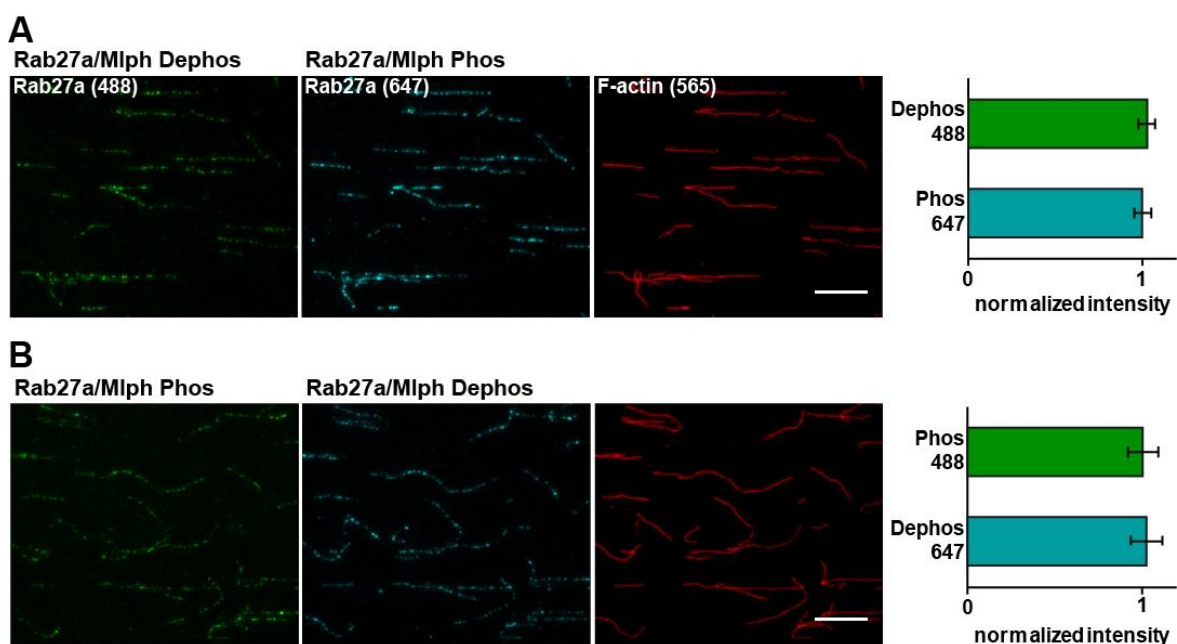

Figure 31: Quantification of Mlph's interaction with actin filaments *in vitro*. (A) Dephosphorylated, Alexa Fluor 488-labeled Rab27a/Mlph complex was mixed in equal amounts with phosphorylated, Alexa Fluor 647-labeled Rab27a/Mlph complex and incubated with surface-attached, Atto565-

labeled actin filaments. The quantification of the actin-associated fluorescence signals from the respective PKA- and phosphatase-treated Rab27a/Mlph complexes showed that the phosphorylation state of Mlph did not substantially interfere with actin actin binding (right panel). (B) Same experiment as in panel A for which the fluorescent labels on the Rab27a/Mlph complexes were swapped. Error bars represent SD. Scale bar: 10 µm.

5.5.3 Phosphorylation of Mlph does not alter complex assembly

Is MyoVa specifically recruited to the pigment granule at the onset of dispersion? *In vitro* reconstituting the tripartite complex with Rab27a, MyoVa and dephosphorylated Mlph or phosphorylated Mlph, respectively, demonstrated that both, dephosphorylated and phosphorylated, Mlph proteins assemble the complex with comparable amounts of Rab27a and MyoVa proteins (Figure 32). Additionally, single-molecule data could be collected with both the dephosphorylated and the phosphorylated MyoVa transport complexes indicating that both complexes assemble similarly well.
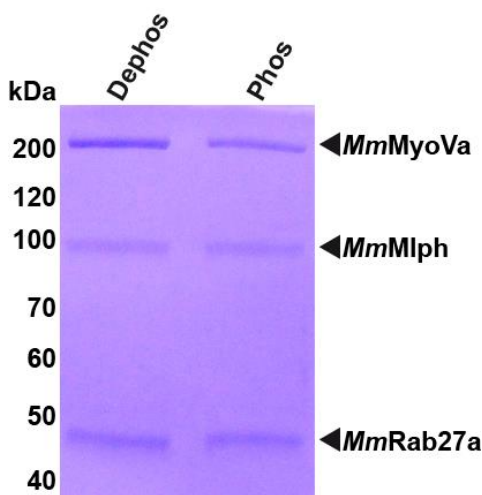
Figure 32: The tripartite complex from mouse can be assembled from full length subunits with both phosphatase-treated (left lane) and PKA-treated Mlph (right lane).

5.6 **Phosphorylation regulates Mlph's binding to MTs**

Not only actin filaments serve as tracks for melanosome transport *in vivo*, but melanosomes are transported on MTs as well. However, no information on a possible interaction between the MyoVa adaptor protein Mlph and MTs has yet been reported. Nevertheless, employing microtubule filaments in the filament decoration assay, as performed with actin filaments described above, was a fairly easy way of testing this possibility. Surprisingly, Mlph in its dephosphorylated state exhibited strong decoration of surface-attached MTs (Figure 33 A, upper panel) (127). In addition, phosphorylated Mlph barely showed an interaction with MTs (Figure 33 A, lower panel). This novel interaction

between Mlph and MTs was again dependent on the C-terminal ABD of Mlph (Figure 33 B) (127).

Figure 33: Mlph interacts with MTs via its ABD in phosphorylation-dependent manner. Microtubule decoration experiments in which fluorescently labeled MTs (red) were incubated with the labeled complex (green) as described in Figure 30. (A) Decoration of MTs was strictly dependent on the phosphorylation st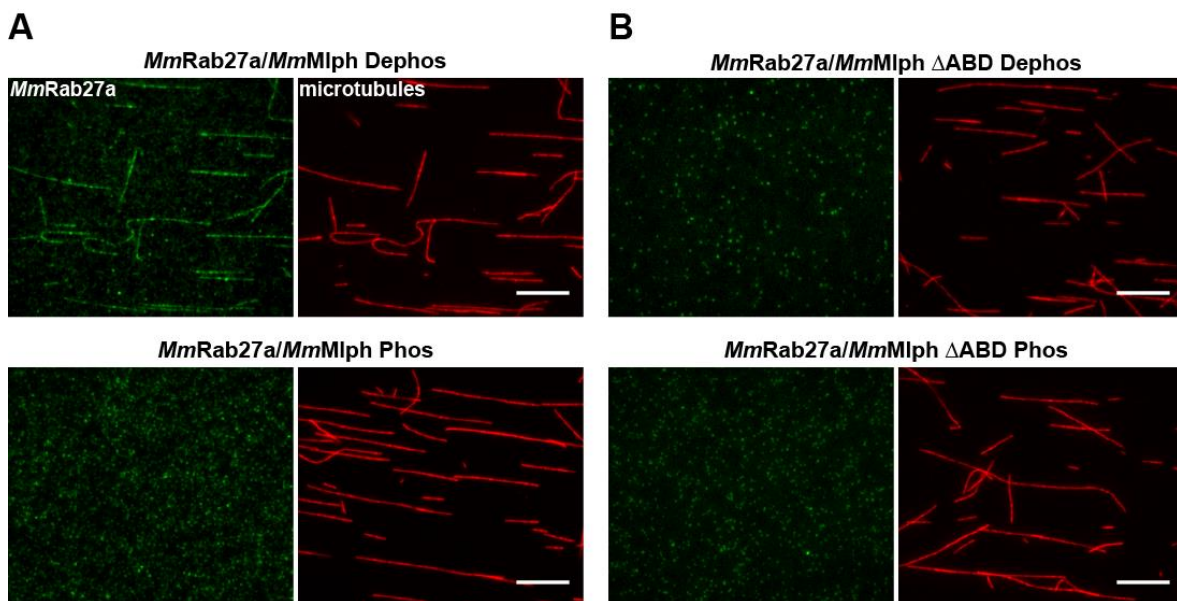ate of Mlph. The fluorescent background from the phosphorylated and dephosphorylated Rab27a/Mlph complex seen in the green channel was comparable indicating similar protein amounts. (B) Removal of the ABD inhibited the interaction of Mlph with MTs. Scale bar: 10 µm.

To conclude, Mlph associates with MTs in a strictly phosphorylation-dependent manner – namely only in the dephosphorylated state – and this interaction is mediated by the previously described C-terminal ABD of Mlph.

5.6.1   Point mutations in the ABD rescue MT binding

If association of Mlph with MTs is indeed phosphorylation-dependent, mutation of the involved residues into alanines, mimicking the dephosphorylated state, will lead to microtubule decoration even in the presence of PKA. Alignment of several ABD domains of Mlph from distinct species (Figure 24) revealed three conserved serine residues that also contained the known PKA consensus site R-R-X-S/T (126). To test whether one or more of these residues are involved in microtubule association, I generated the following unphosphorylatable alanine mutations of the conserved residues and additional neighboring serine or threonine residues: T443/S445/T446, S491/S498, and S544/S546/S547 (Figure 34) (127).

```
                    MmMlph Dephos control mutant
      380           390           400           410           420           430
       |             |             |             |             |             |
SADTEEETLRRRLEELTSNISGSSTSSEDETKPDGTFLGGSPKVCTDTGHMETQERNPRSPGN

MmMlph T443A/S445A/T446A                                    MmMlph S491/498A
 440           450           460           470           480           490           500
  |             |             |             |             |             |             |
PARPTKSTDEELSEMEDRVAMTASEVQQAESEISDIQSRIAALRAAGLTVKPSGKPRRKSGIP

                                            MmMlph S544/546/547A
      510           520           530           540           550           560
       |             |             |             |             |             |
IFLPRVTEKLDRIPKTPPADPDDQAKMPKATTAVPSLLRRKYSPSSQGVDSGSFDRKSVYRGS

      570           580           590
       |             |             |
LTQRNPNGRRGTARHIFAKPVMAQQP
```

Figure 34: Mutated serine and threonine residues in conserved regions within the ABD of Mlph.
Serine and threonine residues in three conserved regions (see Figure 24) were mutated to alanines to mimic the dephosphorylated state. Mutated residues are shown in bold letters. A serine- and threonine-rich stretch outside the ABD was mutated as a negative control (*Mm*Mlph Dephos control mutant).

S498 is the most conserved residue and possesses a strong PKA recognition site, making it the most promising candidate. The other regions (T443/S445/T446, S544/S546/S547) are only partially conserved and possess weak PKA consensus sites, respectively. Additionally, an exceptionally serine- and threonine-rich stretch at the very N-terminus of the ABD that is conserved, but contains no PKA recognition motif, was mutated as a negative control (T392A/S393/396/398/399A/T400A/S401A, Figure 34) and is termed *Mm*Mlph Dephos control mutant.

Wild type and mutated *Mm*Mlph[F] constructs in complex with *Mm*Rab27a-Q78L[S-H] were tandem purified side-by-side, fluorescently labeled with Alexa Fluor 647, and dephosphorylated with antarctic phosphatase (wild type *Mm*Mlph) and phosphorylated

with PKA (wild type and mutant *Mm*Mlphs, Figure 35). Fluorescent labeling with SNAP-
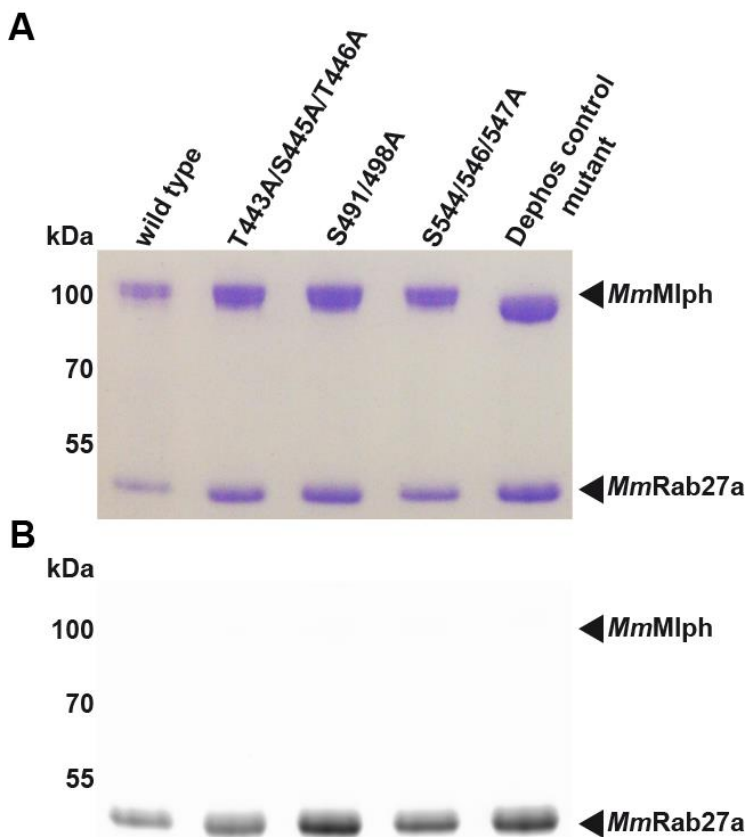
Surface

Figure 35: Purified *Mm*Rab27a in complex with wild type and mutant *Mm*Mlph (T443A/S445A/T446A, S491/498A, S544/546/647A, and Dephos control mutant) analyzed with SDS-PAGE and Coomassie-staining (A) and fluorescence scanning (B).

Alexa 647 specifically occurred on the SNAP-tagged Rab27a subunit (Figure 35 B).These

proteins were employed in MT decoration assays as performed for dephosphorylated and

phosphorylated wild type Mlph (Figure 33). Mutant *Mm*Mlph T443A/S445A/T446A,

S491/498A, and S544/546/547A associated with MTs even in the presence of PKA (Figure

36 A-C) (127). In contrast, the *Mm*Mlph Dephos control mutant failed to decorate MTs

(Figure 36 D). In parallel, wild type *Mm*Mlph treated with phosphatase or PKA decorated

MTs or was not capable of interacting with MTs, respectively (Figure 36 E-F).
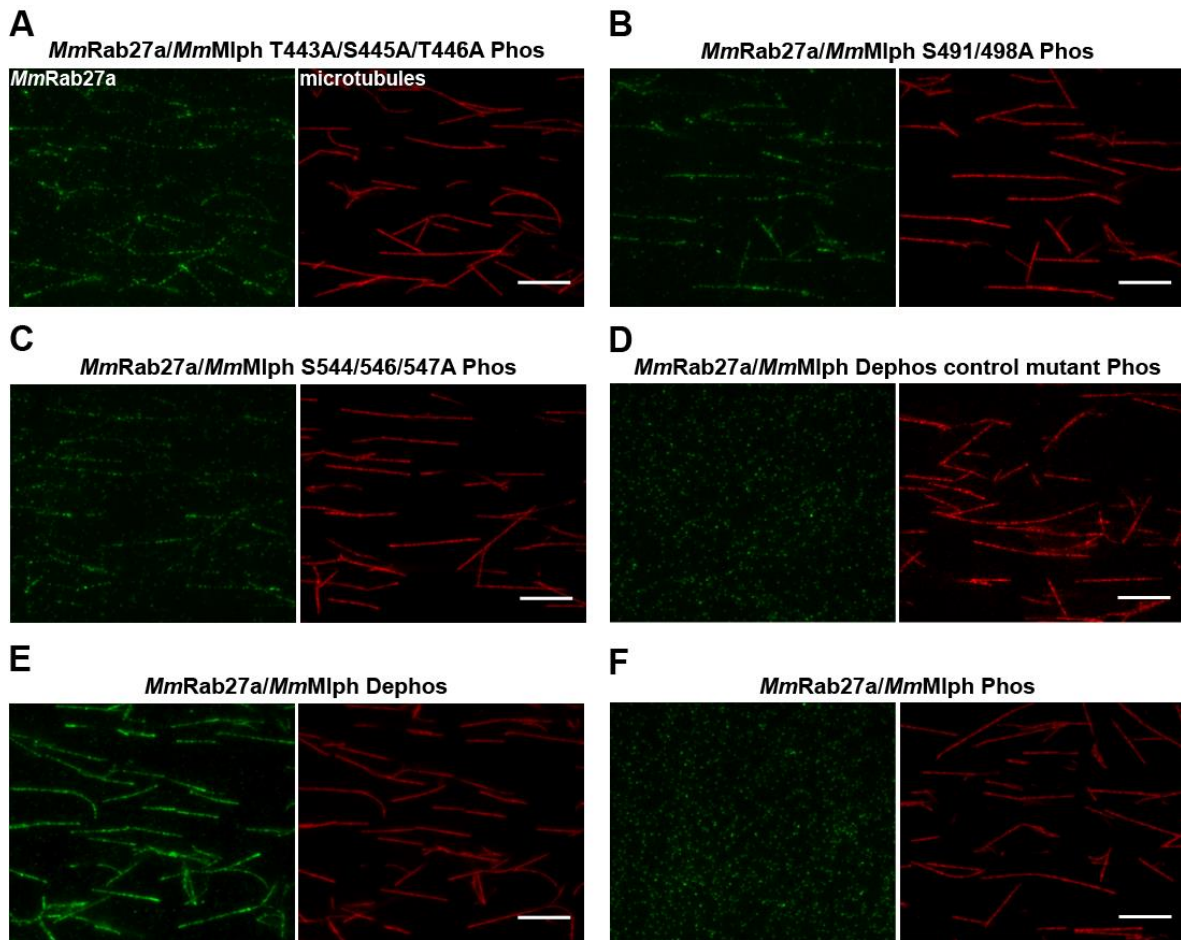
Figure 36: Mutations in candidate phosphorylation sites of Mlph prevent PKA-induced dissociation of Mlph from MTs. MT decoration experiments were performed as in Figure 33. (A-C) PKA-treated Mlph mutants T443A/S445A/T446A, S491/498A, and S544/546/547A all decorated MTs, but not the Dephos control mutant (D). The wild type Mlph decorated MTs in its dephosphorylated state (E), but not in its phosphorylated state (F) as in Figure 33 A. Scale bar: 10 µm.

Collectively, all three mutated regions rescued MT binding even though the proteins were fully phosphorylated. The fact that the *Mm*Mlph Dephos control mutant with mutations outside the ABD is not capable of interacting with MTs additionally demonstrates that the interaction specifically occurs via the ABD. These results strongly support the phosphorylation-dependence of the interaction between Mlph's ABD and MTs.

To verify that the actin association of Mlph is not affected by the introduced mutations, actin decoration assays with F-actin and wild type and mutant *Mm*Mlph constructs were performed. In line with the results obtained with dephosphorylated and phosphorylated wild type *Mm*Mlph in actin decoration assays (Figure 30), all mutant *Mm*Mlph constructs as well as phosphorylated wild type *Mm*Mlph decorated F-actin to a comparable extent (Figure 37) (127).
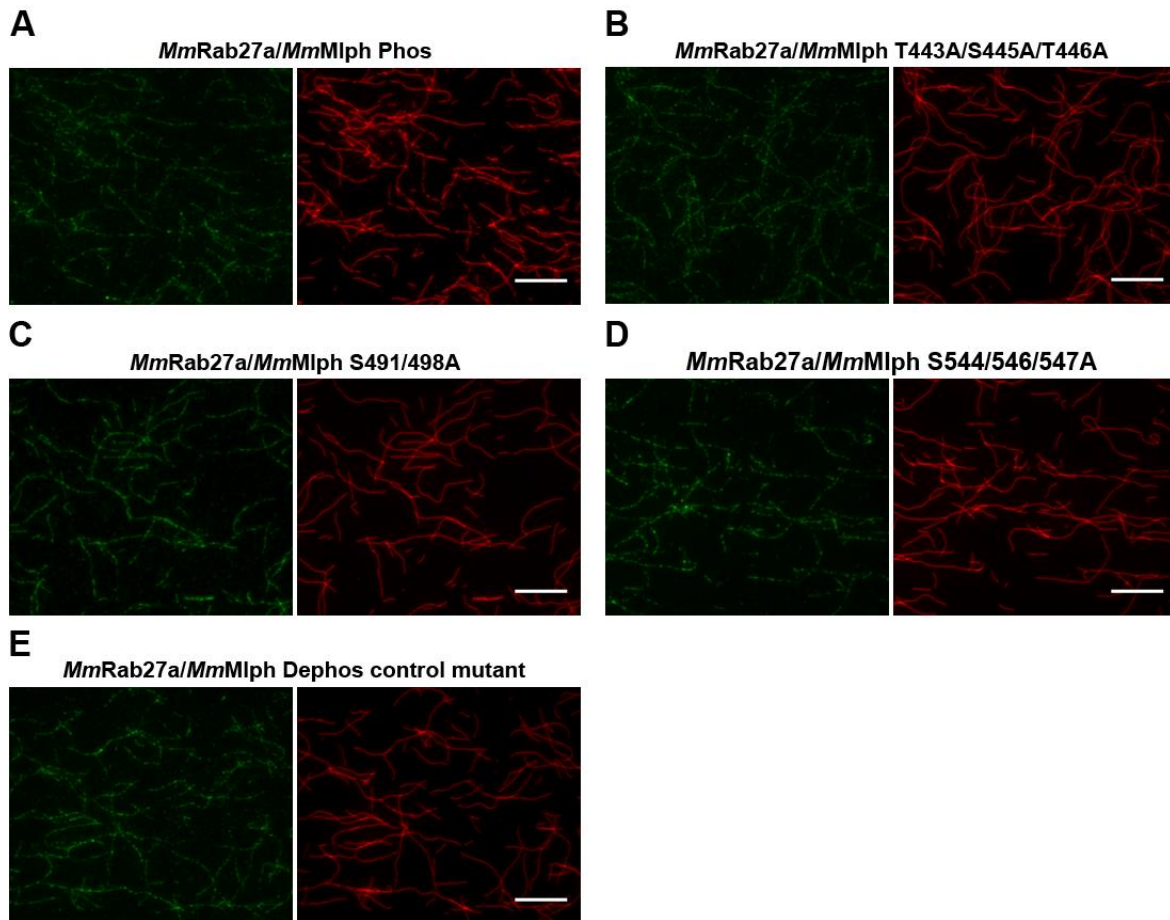
Figure 37: Mutations in candidate phosphorylation sites of Mlph do not interfere with F-actin binding. (A-E) Decoration of fluorescently labeled F-actin (red channel) with the wild type and mutant *Mm*Mlph constructs (green channel) as in Figure 36. All mutant complexes interacted with F-actin as efficiently as the wild type. Scale bar: 10 µm.

5.6.2   S491/498 is the main contributor to MT association

The here performed filament decoration assays only allowed a qualitative statement about the involvement of individual mutated regions in MT association. To obtain more quantitative results different experimental approaches were used. On the one hand, *in vitro* phosphorylation assays are suitable to gather information on how each mutated region influences overall phosphorylation levels. Wild type Mlph and its three rescue mutants were therefore phosphorylated by PKA using radiolabeled ATP and the resulting signals corresponded to the different phosphorylation levels for wild type and mutant Mlphs. On the other hand, quantitatively comparable results on the extent of interaction between different mutated regions and MTs might indicate the importance of one/more site(s) over the others. For this purpose, MT cosedimentation assays were performed. In this experiment, MTs are incubated with the protein of interest followed by

ultracentrifugation through a sucrose cushion. Thereby, MT-bound proteins pellet with MTs and are separated from unbound proteins that remain in the supernatant.

In vitro phosphorylation assays with wild type and mutant *Mm*Mlph demonstrated that the *Mm*Mlph S491/498A mutant could not be phosphorylated efficiently anymore (Figure 38) (127). The phosphorylation level reached 26% compared to wild type *Mm*Mlph, whose phosphorylation level was set to 100%. The phosphorylation of T443A/S445A/T446A was only modestly reduced to 76% and S544/546/547A reached a phosphorylation level of 57% compared to wild type *Mm*Mlph.
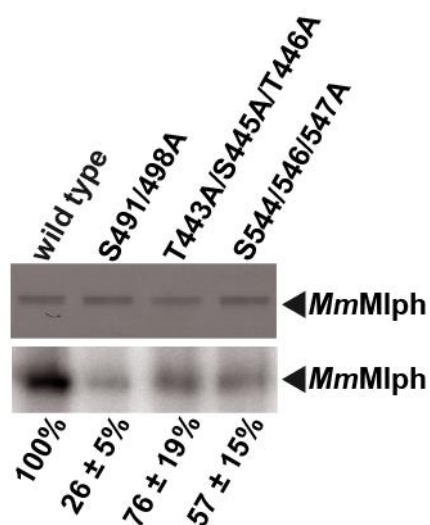

Figure 38: Non-phosphorylatable alanine mutations in the three predicted phosphorylation sites reduce PKA-dependent phosphorylation. *In vitro* phosphorylation assays (lower panel: autoradiograph, upper panel: corresponding Coomassie-stained SDS-PAGE as loading control) with wild type *Mm*Mlph and its mutants showed that the S491/498A mutant suppressed the PKA-dependent phosphorylation of Mlph most efficiently (26%) when compared to wild type (100%), T443A/S445A/T446A (76%), and S544/546/547A mutants (57%), where weaker and less conserved PKA recognition sites were mutated. Percentages are mean values obtained from two independent assays ± SD.

For quantifying the Mlph-MT interaction, wild type and mutant *Mm*Mlph proteins were treated with PKA for phosphorylation. In parallel, *Mm*Mlph lacking its ABD (ΔABD) and phosphatase-treated wild type *Mm*Mlph were prepared. MT cosedimentation assays were performed side-by-side with identical concentrations of all proteins described above. Equal volumes of the total reaction, supernatant, and pellet were analyzed with Coomassie-stained SDS-PAGE. *Mm*Mlph lacking its ABD did not interact with MTs (Figure 39, I) and only 4% of the applied phosphorylated wild type *Mm*Mlph interacted with MTs (Figure 39, II). In contrast, 27% of the applied dephosphorylated wild type *Mm*Mlph bound to MTs (Figure 39, III), further supporting the results from decoration assays that demonstrated that dephosphorylated Mlph associates with MTs and phosphorylated Mlph does no longer interact with MTs. All mutant Mlph constructs displayed a significantly higher extent of interaction with MTs than phosphorylated wild type Mlph (Figure 39, IV-VI), with S491/498A showing the most pronounced rescue of interaction (127).
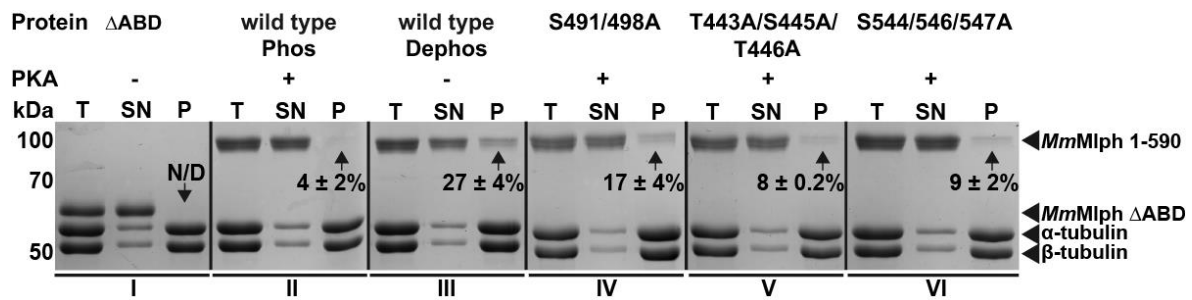
Figure 39: S491/498A is the main contributor to the phosphorylation-dependent release of Mlph from MTs. MT cosedimentation assays were performed side-by-side with the truncated Mlph that lacked its ABD (I, ΔABD), phosphorylated wild type Mlph (II, wild type Phos), dephosphorylated wild type Mlph (III, wild type Dephos), and along with phosphorylated Mlph that carried the respective nonphosphorylatable alanine mutations (IV-VI). The total reaction (T), supernatant (SN), and pellet (P) were analyzed with Coomassie-stained SDS-PAGE. As expected from results shown in Figure 33, Mlph that lacked its ABD and the phosphorylated wild type Mlph failed to display a pronounced interaction with MTs (N/D and 4%, I-II). In line with results from Figure 36, the dephosphorylated wild type Mlph and all rescue mutants displayed significant pelleting with MTs (8%-27%, III-VI). The S491/498A mutant containing the strong and most conserved PKA consensus site S498 also demonstrated the most pronounced effect of rescue (17%, IV). Percentages are mean values obtained from two independent assays ± SD. N/D, not determinable.

To summarize, the quantitative characterization of the *Mm*Mlph rescue mutants using *in vitro* phosphorylation assays and MT cosedimentation assays revealed that the most conserved serine residue 498, which possesses the strong PKA consensus site, suppressed phosphorylation most efficiently and rescued MT binding best. Taken together, these results implicate that S498 is the key site in regulating MT association of Mlph through PKA-dependent phosphorylation.

5.7 Dephosphorylated Mlph predominantly associates with MTs in the presence of both filaments

What is the *in vivo* implication of the results presented so far? I demonstrated that the MyoVa adaptor protein Mlph is not only capable of binding to actin filaments, but is also able to interact with MTs *in vitro*. Importantly, the association of Mlph to MTs is strictly dependent on Mlph's phosphorylation status. Dephosphorylated Mlph bound to MTs, whereas phosphorylated Mlph did not. To approach the cellular scenario for melanosome transport further with *in vitro* tools at hands, I built so-called mixed networks, containing both actin filaments and MTs. With this experimental setup, I wanted to test which interaction was stronger under competitive conditions with both filaments present.
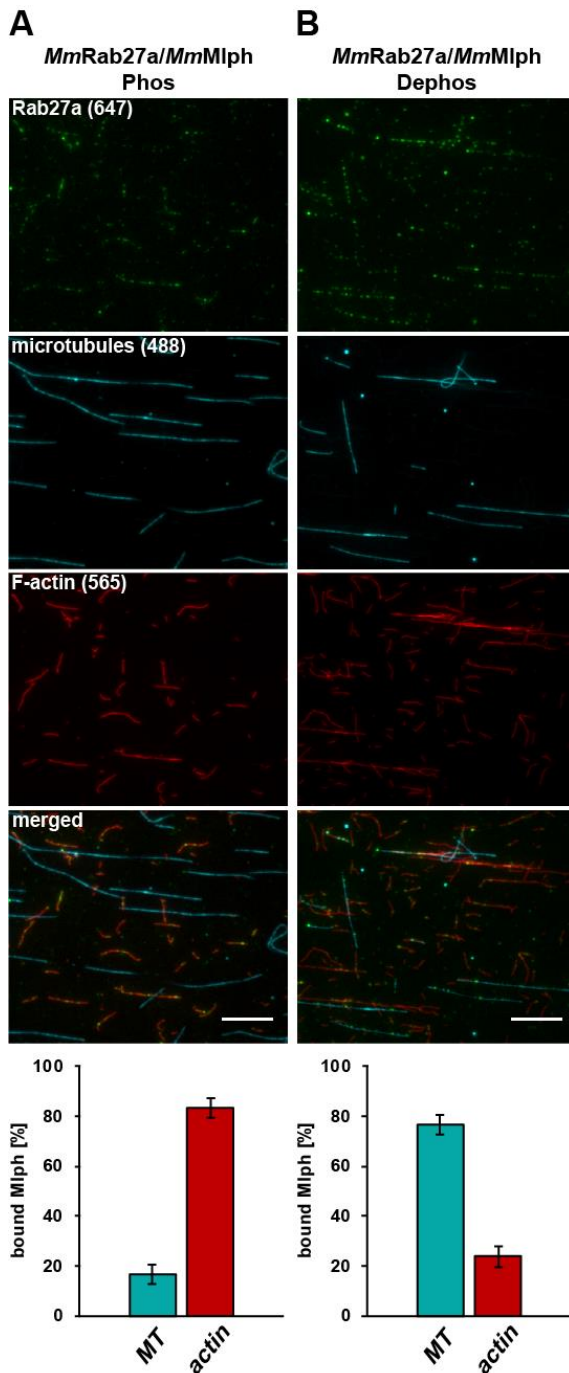
Figure 40: Dephosphorylation sufficiently relocates Mlph from actin filaments to MTs *in vitro*. (A) Surface-immobilized and Atto488-labeled MTs and Atto565-labeled actin filaments were incubated with phosphorylated complex formed between Mlph and Alexa Fluor 647-labeled Rab27a. Under these competitive conditions, the binding of the phosphorylated Rab27a/Mlph complex to actin dominated (83 ± 4%) over MT binding (17 ± 4%). (B) Upon dephosphorylation, the behavior of the Rab27a/Mlph complex was reversed and the MT binding clearly dominated (76 ± 4%) over actin binding (24 ± 4%). Error bars represent SD. Scale bar: 10 µm.

To build the actin/MT networks *in vitro*, Atto488-labeled MTs and Atto565-labeled actin filaments, both biotinylated, were attached to the biotin-streptavidin-coated flow chamber surface. Dephosphorylated or phosphorylated Rab27a/Mlph complex labeled with Alexa Fluor 647 was subsequently added and the chamber was imaged using three-color TIRF microscopy. The actin and MT area was determined using a custom MATLAB tool. The fluorescence intensity associated with each filament type was quantified and the percentage of Mlph bound to each filament type was calculated for each image.

Intriguingly, phosphorylated Rab27a/Mlph complex preferentially associated with actin filaments (Figure 40 A) in the presence of both filament types (127). In stark contrast, MT binding clearly dominated in the case of dephosphorylated Rab27a/Mlph complex (Figure 40 B). This experiment suggests that the interaction between MTs and Mlph might to be stronger than Mlph's association with actin filaments.

In conclusion, MTs efficiently compete for Mlph binding in the presence of actin filaments *in vitro.* Phosphorylation is sufficient to relocalize Mlph from MTs onto the actin network.

5.8 The ABD of Mlph enforces track selection on the MT and actin networks *in vitro*

I showed that MyoVa's adaptor protein Mlph in complex with Rab27a interacts with both actin filaments and MTs *in vitro*. On cytoskeletal networks composed of MTs and actin filaments, Mlph's phosphorylation state dictated to which filament Mlph primarily binds. Dephosphorylated *Mm*Rab27/Mlph complex predominantly associated with MTs, whereas phosphorylated *Mm*Rab27a/Mlph complex preferred to bind to actin filaments. What are the functional consequences of Mlph phosphorylation on the physiologically relevant MyoVa transport complex Rab27a/Mlph/MyoVa? To answer this question *in vitro*, single-molecule TIRF assays with the tripartite complex assembled with dephosphorylated or phosphorylated Mlph on networks built with actin filaments and MTs were performed. As expected from an actin-based motor protein, the MyoVa transport complex with phosphorylated Mlph incorporated mainly exhibited directional movement on actin filaments (Video 4) (127). In stark contrast, the MyoVa transport complex built with dephosphorylated Mlph showed diffusional movement on MTs to a significant extent besides directional transport on actin filaments (Video 5) (127).

Remarkably, Mlph was able to dictate filament association of the tripartite complex even in the presence of the actin-based motor protein MyoVa. The tripartite complex switched between actin filaments and MTs at inter-filament intersections (Figure 41, Video 6, Video 7) (127).
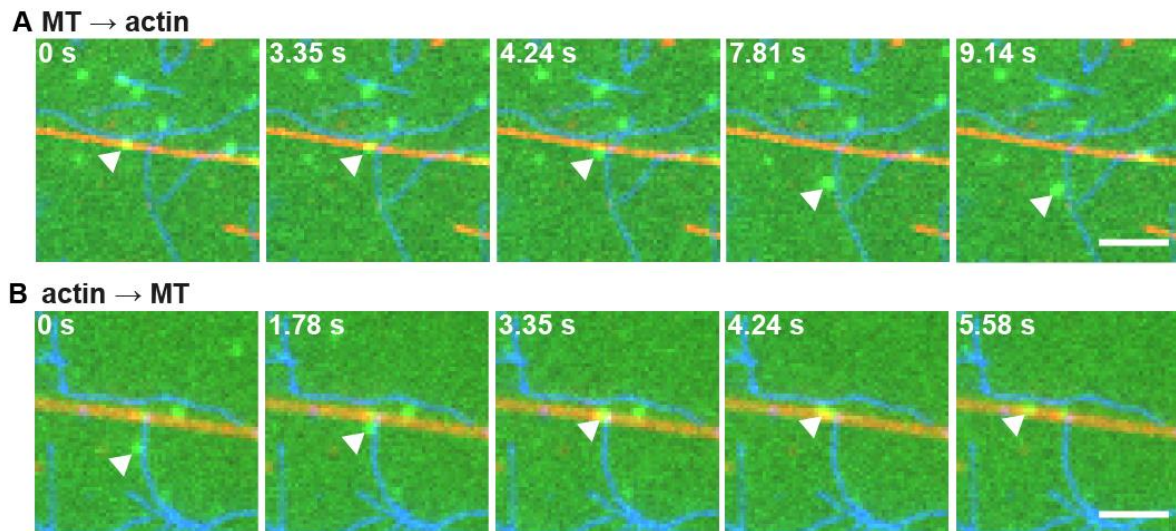
Figure 41: Examples of switching events at actin-MT intersections. (A) Example of a tripartite complex (green) that diffused on MTs (red) and switched to an intersecting actin filament (blue) (Movie S3) and (B) of a tripartite complex that moved directionally on the actin filament and switched to an intersecting MT (Movie S4). Scale bar: 3 μm.

To assess the influence of the phosphorylation state of Mlph's ABD on the switching behavior of the tripartite complex, only complexes that were in close proximity to an actin-MT intersection and either passed the intersection without changing filament type or switched filament type at the intersection were taken into account. The percentages of passing and switching complexes were calculated for each switching direction (from actin to MTs and vice versa). One third of the complexes assembled with dephosphorylated Mlph switched from actin onto MTs (Figure 42 A) (127). Complexes exhibited directional movement on actin filaments that was interrupted by diffusion on MTs. Opposed to this, the propensity to switch from actin to MTs was completely abolished when the tripartite complex was reconstituted with phosphorylated Mlph (Figure 42 B). In fact, complexes with phosphorylated Mlph rarely interacted with MTs (reflected in the low N number of switching events from MTs to actin filaments for the complex with phosphorylated Mlph) and mostly displayed uninterrupted directional movement on actin filaments (Video 4).

MyoVa was previously shown to interact with MTs on its own. Specifically, MyoVa diffuses on MTs (84, 85). What is MyoVa's contribution to the interaction between MTs and the tripartite complex? Tripartite complexes with dephosphorylated or phosphorylated Mlph lacking the ABD (Mlph ΔABD) were reconstituted and tested on actin and MT networks *in vitro*. Independent of the phosphorylation state, tripartite complexes assembled with Mlph ΔABD exhibited a probability of around 7% to switch from actin to MTs and around 65% to

switch from MTs to actin filaments (Figure 42 C and D). Importantly, phosphorylation of Mlph outside the ABD did not influence the switching behavior of the assembled complexes.
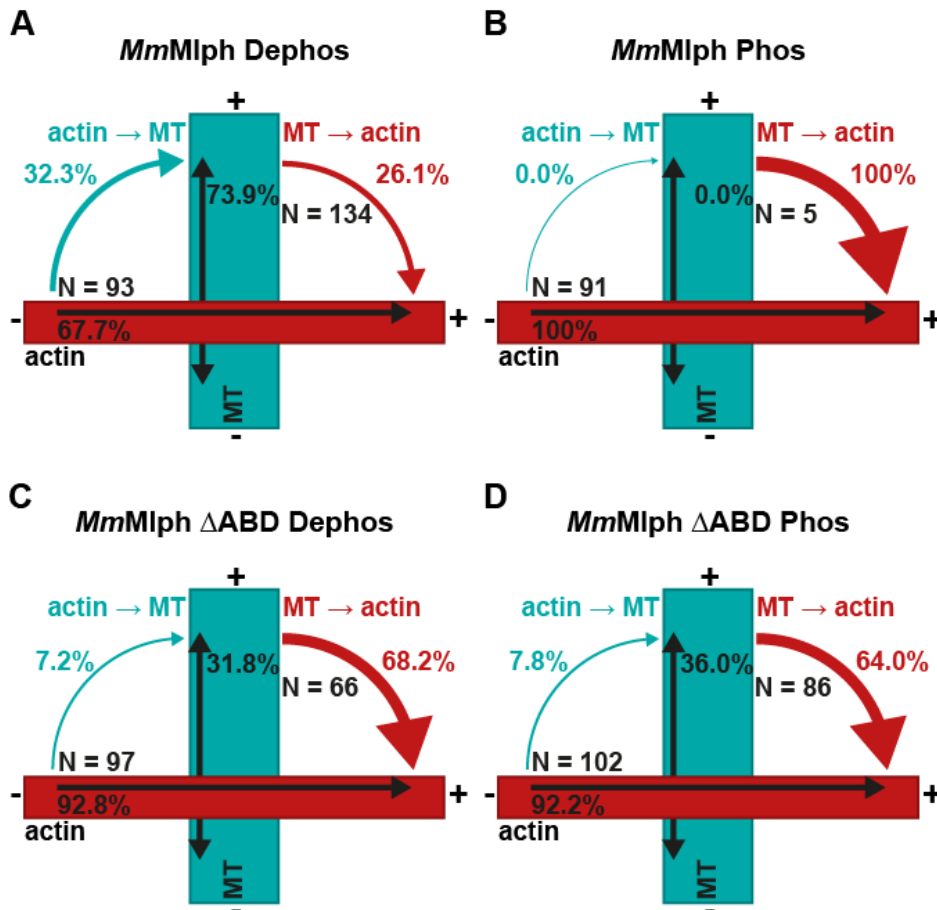

Figure 42: Phosphorylation state of Mlph's ABD dictates the directionality of switching at the actin-MT intersections. Movement of the tripartite complex on actin and MTs is represented by single- and double-headed black arrows, respectively. Cyan arrows depict switching from actin to MTs, red arrows indicate switching from MTs to actin. (A) The tripartite complex reconstituted with dephosphorylated Mlph displayed a significantly higher probability to switch from actin to MTs at the inter-filament intersections. Whereas 32.3% of complexes switched from actin to MTs (67.7% continued directional movement on actin, A), (B) the propensity of switching from actin to MTs was abolished when the tripartite complex was assembled with phosphorylated Mlph. The phosphorylated complex completely ignored the inter-filament intersections (0% switching) and continued its directional movement on the actin (100%, B). Conversely, dephosphorylated Mlph significantly suppressed the switching probability of the complex from MTs to actin (26.1%, A) when compared to the complex built with phosphorylated of Mlph (100%, B). Indeed, the phosphorylated complex rarely interacted with the MTs substantially decreasing the probability of switching events from MTs to actin (Video 4). (C, D) In contrast, tripartite complexes assembled with dephosphorylated Mlph ΔABD (C) and phosphorylated Mlph ΔABD (D) displayed similar probabilities to switch between the two filament types confirming that phosphorylation outside of Mlph's ABD did not interfere with the switching behavior of the tripartite complex. N indicates the number of events for each switching direction.

Taken together, the phosphorylation state of Mlph's ABD dictates the track selection of the MyoVa transport complex on actin filaments and MTs. Phosphorylation of Mlph's ABD is sufficient to locate the MyoVa transport complex onto actin filaments. Dephosphorylation of Mlph's ABD, on the other hand, enhances the interaction of the complex with MTs.

6. **Discussion**

For intracellular transport, eukaryotes often employ a set of distinct motor types that unite their efforts to achieve proper cargo delivery within the cell. This motor ensemble commonly consists of two MT-based molecular motors with opposing transport direction and an actin-based motor protein. As these motor proteins work together, a tight regulation of motor activity is needed to ensure an effective overall transport of cargo. Despite the prevalence of this concept to join efforts of different types of motors to transport one single cargo, only very limited insights have been obtained about mechanisms that functionally link the two cytoskeletal systems.

Using melanosomes from the amphibian *Xenopus laevis*, a well-studied model system for intracellular transport, I set out to shed light onto the molecular mechanisms governing coordination of MT- and actin-based motor proteins. MT-based and actin-based motility of melanosomes was reconstituted previously *in vitro* (12, 15). For MT-based motility, it was shown that the regulated cell states (i.e. dispersed and aggregated cell state) were retained after the purification procedure (12), enabling the investigation of motor regulation during melanosome transport *in vitro*. In contrast, it remained to be shown that the regulated states for the actin-based transport that were observed *in vivo* (50% downregulation of MyoVa during aggregation (73)) are also preserved *in vitro*. Therefore, I reconstituted melanosome motility on actin filaments *in vitro* and compared the motility of melanosomes from the dispersed and aggregated cell states regarding the number of transport events, but also the kinetic transport parameters (e.g. velocity and run length). The here obtained velocity and run lengths values were well in line with published parameters from actin motility of melanosomes isolated from mouse melanocytes, *in vivo* tracking (110, 133), or recombinantly expressed full length *Xl*MyoVa (90), supporting that the purification procedure and assay conditions did not interfere with melanosome motility. However, the first published reconstitution of melanosome motility on actin cables from *Nitella* reported a significantly slower average velocity of 36 nm s^{-1} (15). Since there are several reports of a MyoVa velocity of approximately 100-200 nm s^{-1} *in vitro*, including the velocity displayed by recombinantly purified *Xl*MyoVa, it seemed that the slow velocity might be caused by the *Nitella* actin cables or other assay conditions and did not reproduce the actual MyoVa-driven melanosome velocity.

I observed a higher frequency of runs on F-actin for melanosomes purified from dispersed cells than from aggregated cells, though melanosomes from both cell states exhibited similar biophysical transport parameters. Thus, actin-based transport is regulated during the two cell states and the regulation seems to occur on the melanosome surface alike the MT-based melanosome motility. Motor protein activity did not seem to be primarily modulated, because the biophysical transport parameters did not differ between dispersion and aggregation. Moreover, cytoplasmic extract from the dispersed cell state was sufficient to reactivate 'dormant' melanosomes from aggregated melanophores, indicating that the activating factor for actin-dependent transport of melanosomes was present in the cytoplasm of dispersed melanophores. Is it possible to identify the cytoplasmic factor responsible for this regulation? Intracellular cAMP levels were demonstrated to influence the switching from MT to actin filaments in fish melanophores (81) and it is long known that PKA activity plays a key role in the signaling cascade for dispersion (57, 58). However, so far signaling cascades have not been linked to the motor proteins that conduct the transport of melanosomes. Applying constitutively active PKA on purified melanosomes revealed that the frequency of actin-based melanosome transport events was directly regulated by PKA and this regulation directly occurred on the melanosome surface. For the first time, the downstream target(s) of PKA were pinpointed to be present directly on the melanosome surface. Furthermore, the reconstituted actin-based melanosome motility assays suggested that PKA was involved in the coordination between both transport systems by upregulating the actin-based motility during dispersion. Molecular details of this coordination mechanism by PKA or the identity of PKA target protein(s), however, remain elusive. In contrast, it was suggested earlier that MyoVa is mainly regulated via detachment (aggregation) and recruitment (dispersion) to the melanosome (73). The here presented result that addition of PKA is sufficient to reactivate aggregated melanosomes in the absence of any cytosolic MyoVa strongly contradicts a regulation mechanism solely by motor recruitment.

The most obvious target of PKA is the motor protein MyoVa itself, followed by one of the two adaptor proteins linking MyoVa to the melanosome surface (i.e. Rab27a or Mlph). To directly test this hypothesis, I opted for recombinantly expressing the three proteins from *Xenopus laevis* and *Mus musculus*. Both, *Xt*Mlph and *Mm*Mlph, proved to be difficult in handling (e.g. abnormal running behavior in SDS-PAGE and tendency to aggregate) and

could not be objected to size-exclusion chromatography as the protein was absorbed to the column material to a high extent. Elution profiles of the Mlph fraction that did not bind to the column suggested that the Mlph protein by itself was not homogenous. Mlph ran higher on SDS gels than its calculated molecular mass from the amino acid sequence as reported earlier (117, 118, 120). This might be caused by posttranslational modifications or a unique amino acid sequence (Mlph possesses a high number of serine and threonine residues). In complex with Rab27a, Mlph seemed to be more homogenous, because no aggregates were observed when fluorescently labeled Rab27a/Mlph complex was visualized via TIRF microscopy. By coexpressing Rab27a and Mlph proteins and subsequent incubation of the dimeric complex with MyoVa it was possible to reconstitute the tripartite complex from both organisms *in vitro*. This has been achieved with mouse proteins before (117), however the tripartite complex was reconstituted by mixing Rab27a/Mlph complex with MyoVa and the assembled tripartite complex was never directly shown by SDS-PAGE. For amphibians, it is the first evidence that MyoVa attachment occurs in the same way as in the distantly related species mouse. In particular, it has not been demonstrated that Mlph binds Rab27a in a GTP-dependent manner and that exon F is absolutely essential for the Mlph-MyoVa interaction in the amphibian *Xenopus laevis*. This is homologous to the mouse tripartite complex (44-47), implying that the anchorage of MyoVa to the melanosome is evolutionary conserved.

In vitro phosphorylation assays with radiolabeled ATP and various constructs of the MyoVa transport complex revealed that Mlph was the specific and sole target of PKA. Especially, Mlph's ABD is target of phosphorylation. Moreover, the PKA target is conserved from amphibians to mammals, as *Xt*Mlph and *Mm*Mlph are both specifically phosphorylated *in vitro*. This is the first identification of a substrate for PKA and expands the knowledge on signal transduction in melanosome transport to an element downstream of PKA, in particular in mouse where signaling pathways are not well explored and involvement of PKA has not been demonstrated. Importantly, these results collectively demonstrate that PKA directly acts on the melanosome surface by phosphorylating Mlph. Remarkably, the *in vitro* phosphorylation pattern of *Mm*Mlph ABD closely resembled the previously published *in vivo* phosphorylation pattern (124, 125), validating this candidate approach with the kinase PKA to investigate the function of this phosphorylation with mouse proteins *in vitro*. Three conserved regions for phosphorylation in the ABD were identified. Mass

spectrometry analysis of recombinantly expressed and purified Rab27a/Mlph complex confirmed the phosphorylation of all conserved regions in the *in vitro* phosphorylation assays performed during this study.

Surprisingly enough, PKA's target is the adaptor protein Mlph of the actin-based motor MyoVa and not the motor itself. How is actin-based transport regulated by phosphorylation of Mlph and, further, how is transport coordination achieved by Mlph phosphorylation in the cell? Mlph has previously been implicated by different studies to play a role in coordinating the two different transport systems (37, 45, 46, 50, 83). How can phosphorylation of the adaptor protein Mlph govern coordination of both transport systems? Motor activity was not altered between dispersion and aggregation as implied by similar kinetic transport parameters obtained from *in vitro* motility assays with melanosomes from the distinct cell states (see section 5.1.1, page 59). In addition, transport parameters of tripartite complexes assembled with dephosphorylated or phosphorylated Mlph, respectively, were indistinguishable (5.5.1).

Does the phosphorylation modulate the previously discovered interaction between Mlph and actin and thereby bias transport direction? To investigate a potential role for ABD phosphorylation in modulating Mlph's affinity for actin filaments, I performed *in vitro* decoration experiments with the dephosphorylated and phosphorylated Rab27a/Mlph complex on actin filaments. Unexpectedly, the phosphorylation state of Mlph did not alter the interaction between Mlph and actin filaments in decoration assays *in vitro* (see section 5.5.2, page 84). Regardless of the phosphorylation state, both dephosphorylated and phosphorylated Mlph decorated actin filaments similarly well, which was supported by quantification of the actin-associated fluorescence intensities for dephosphorylated and phosphorylated Mlph. Furthermore, the stability of the tripartite complex is not affected by the phosphorylation of Mlph (see section 5.5.3, page 87).

The findings that Mlph suppressed dynein activity during dispersion in zebrafish melanophores (83) and Mlph tracked MT plus-ends via the +TIP EB1 (50) imply a potential connecting function of Mlph between both cytoskeletal transport systems. *In vitro* decoration assays with MTs could easily reveal whether Mlph was additionally capable of directly interacting with MTs. Indeed, Mlph interacted with MTs strictly dependent on its phosphorylation state. Only dephosphorylated Mlph bound to surface-attached MTs via

the ABD, whereas phosphorylated Mlph barely interacted with MTs *in vitro* (see section 5.6, page 87). Alanine mutations of the serine or threonine residues in the three conserved regions that mimic the dephosphorylated state rescued binding to MTs even in the presence of active PKA (see section 5.6.1, page 88). Quantitative phosphorylation assays and MT cosedimentation assays demonstrated that the most conserved serine 498, which possesses a strong PKA recognition site, was the main contributor to Mlph's association with MTs. Nevertheless, the other two regions were able to rescue MT binding to a significant extent as well, pointing to bulk electrostatics that collectively contribute to the phosphorylation-dependent release of Mlph from MTs. This is the first report of a direct interaction between Mlph and MTs via Mlph's C-terminal ABD. Importantly, the interaction between Mlph and MTs is strictly phosphorylation-dependent.

To further resemble the situation in the cell *in vitro*, I built mixed networks with actin filaments and MTs in flow chambers to test Mlph localization in the presence of both filaments. Using the fluorescently labeled dephosphorylated or phosphorylated Rab27a/Mlph complex, I could demonstrate that dephosphorylation of Mlph was sufficient to relocate Mlph from actin filaments onto MTs. In other words, localization of Mlph on actin filaments and MTs was regulated via phosphorylation of Mlph's ABD. Specifically, phosphorylation released Mlph from MTs and led to Mlph association to actin filaments. Vice versa, dephosphorylation of Mlph localized Mlph mainly to MTs.

How might phosphorylation of Mlph be involved in biasing melanosome transport direction in the cell? Foremost, transport direction is determined by the activity of the motor proteins. As previously demonstrated, dynein is upregulated during melanosome aggregation and downregulated during dispersion, whereas MyoVa activity is higher during dispersion and decreased during melanosome aggregation (73). Additionally, switching between MTs and actin filaments is essential to achieve correct intracellular melanosome distribution. Slepchenko et al. discovered that the switching of melanosomes is determined by the regulation of the MT-based transport in fish melanophores (82). Specifically, they found that the switching rate from actin filaments onto MTs was significantly increased during melanosome aggregation, while the switching rate from MTs to actin filaments remained unchanged. Therefore, they postulated that, in addition to motor protein activity, another layer of regulation might be involved in determining the transport direction of

melanosomes. The here presented finding of the phosphorylation-dependent binding of Mlph to MTs could reasonably explain the regulated switching rate from actin filaments to MTs, assuming that melanosome transport in mouse melanocytes follows similar mechanisms. The prerequisite would certainly be that association of Mlph to actin filaments or MTs was dominant over MyoVa binding to either actin or MTs. Single-molecule TIRF assays with the tripartite complex Rab27a/Mlph/MyoVa on networks of actin and MTs *in vitro* demonstrated that the phosphorylation state of Mlph's ABD enforced track selection on actin and MT networks *in vitro*. To my knowledge, this is the first direct demonstration of the regulatory dominance of an adaptor protein over its associated motor protein. Furthermore, these results highlight the function of an adaptor protein in crosstalk between the actin- and MT-based transport systems besides linking motor proteins to cargo.

How can phosphorylation of Mlph's ABD bias intracellular melanosome transport on actin and MTs *in vivo*? To disperse melanosomes in amphibian melanophores, both phosphorylation by PKA and switching of melanosomes from MTs onto actin filaments are required. During dispersion, MyoVa activity is increased to favor switching onto actin filaments and thereby actin-based transport is promoted (73). In mouse melanocytes, signal transduction governing intracellular melanosome transport remains largely elusive. Nevertheless, it has been shown that the MyoVa transport complex is essential for delivering melanosomes to the cell periphery. As presented in this work, Mlph, in particular its ABD, is phosphorylated by PKA (127). Thereby, the affinity of the melanosome is lowered for MTs (Figure 43 A), supporting the transfer of melanosomes from MTs onto actin filaments and favoring MyoVa-driven transport on actin filaments.

Oppositely, aggregation is characterized by increased dynein activity, lowered MyoVa activity and increased phosphatase activity. Consequently, Mlph is mainly present in its dephosphorylated state that favors binding to MTs (127) and aids dynein-dependent switching from actin filaments to MTs (Figure 43 B).
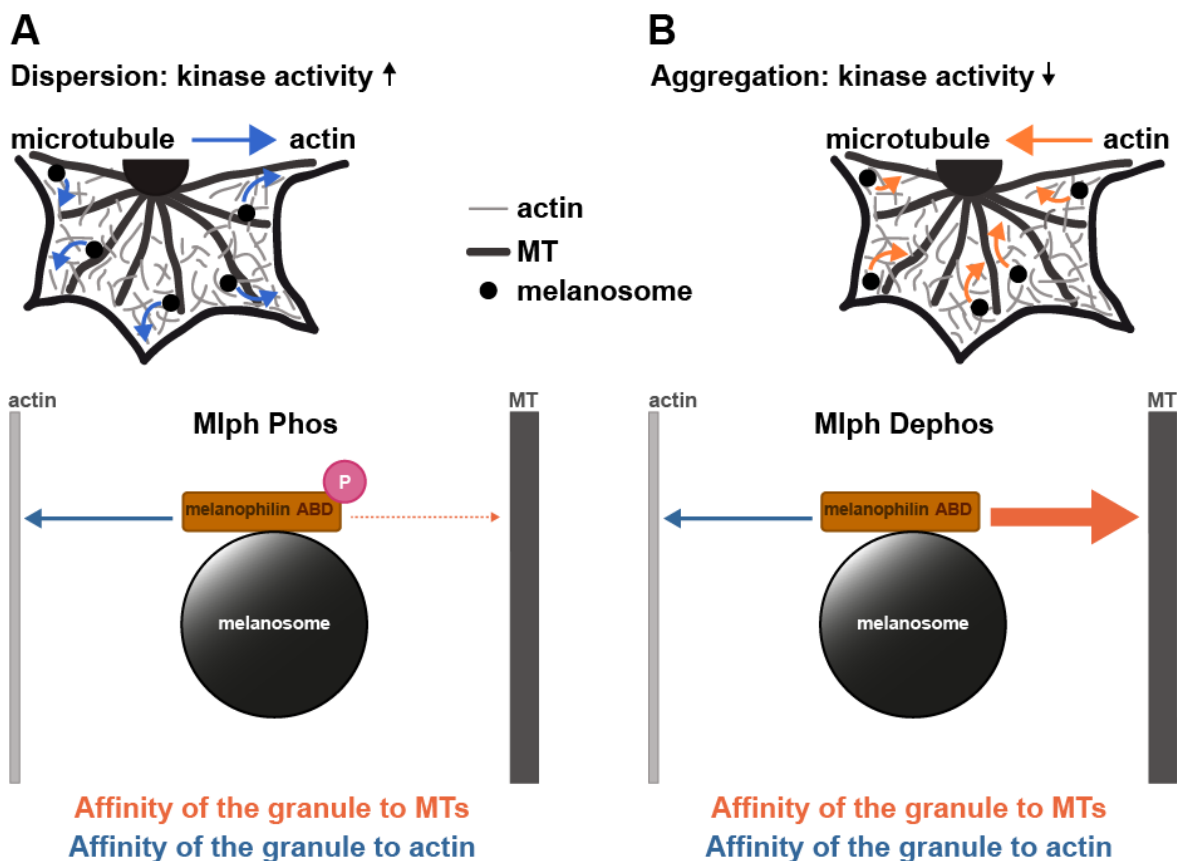
A

Dispersion: kinase activity ↑

B

Aggregation: kinase activity ↓

Figure 43: Tuning the affinity of melanosomes to the MT network through specific targeting of Mlph. (A) During dispersion, kinase activity is increased and phosphorylation events occur (e.g. in amphibian melanophores, cAMP levels increase that activate PKA). The resulting phosphorylation of Mlph within its ABD decreases the affinity of Mlph for MTs. Release from MTs in turn supports the transfer of the organelles to actin filaments by an increased activity of MyoVa. (B) At the onset of aggregation, kinase activity declines, phosphatase activity is increased (e.g. PP2A in Xenopus melanophores) and Mlph loses its phosphorylation. The affinity of Mlph toward MTs thereby increases, promoting the transfer of the organelles onto the MT network for aggregation (arrow diagrams are adapted from (82)) as an additional mechanism to assist dynein-mediated transport that is upregulated during the aggregation process.

The phosphorylation state of Mlph's ABD dictates the track selection on actin and MTs of the entire tripartite complex, even when the actin-based motor protein MyoVa is present. Specifically, phosphorylation of Mlph's ABD favors uninterrupted directional movement on actin filaments and the complex largely ignores MTs (Figure 44 A) (127). In stark contrast, dephosphorylation of Mlph's ABD is sufficient to interrupt directional movement on actin filaments and significantly increase the interaction of the complex with MTs (Figure 44 B).
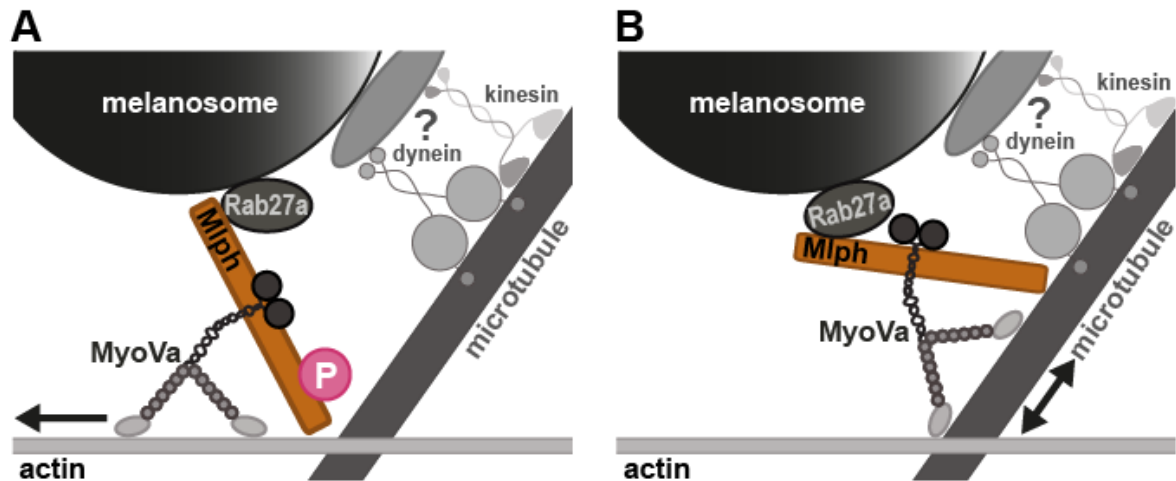
Figure 44: Proposed model for regulating the affinities of the moving organelles on the MT and actin networks *in vivo*. The mechanistic dissection unmasked the regulatory dominance of the adaptor protein Mlph over its associated motor. Even though MyoVa is an actin-associated motor, the dephosphorylation of Mlph's ABD was sufficient to redirect the MyoVa from directional movement on the actin network to MTs for diffusive movement. Consequently, the phosphorylation state of Mlph's ABD regulated the probability of directional switching of MyoVa between the MT and actin networks. Based on these findings, I propose that Mlph serves to bias the transport of organelles on the MT or actin networks *in vivo*. (A) Specifically, phosphorylation of Mlph's ABD promotes MyoVa-dependent motility on the actin network by suppressing the affinity of the tripartite complex towards MTs. (B) To reverse this process, Mlph is dephosphorylated to increase the affinity of the tripartite complex for the MT network (B).

Taken together, the *in vitro* dissection of the actin-based MyoVa transport complex revealed the regulatory dominance of the adaptor protein Mlph over its motor protein MyoVa that biases the transport complex towards either actin or MTs via phospho-targeting of Mlph's ABD.

7. Outlook

The novel findings presented in this thesis open up several exciting research directions to gather a more detailed knowledge on the mechanisms governing intracellular melanosome transport. As the understanding of principles underlying intracellular transport advances, it becomes clear that the concept of using a team of distinct motor proteins for the transport of a single cargo (e.g. vesicle or organelle) is widely employed. How melanosome transport is regulated might therefore also be applicable to other intracellular transport processes and consequently be of general interest.

The reconstitution of actin-based motility of melanosomes from *Xenopus laevis* on actin filaments *in vitro* provides an experimental setup to test the effects of further kinases or inhibitors on MyoVa-driven transport of pigment granules. Other kinases (e.g. PKC or MAPK kinase) are implied to also regulate dispersion in amphibian melanophores and can be tested with the *in vitro* motility assays. The question how crosstalk and coordination between the actin- and MT-system is achieved in cells can be addressed by application of inhibitory substances specific for one motor protein. Observation of possible effects on the other motor proteins might point to a coordinated action or rather a tug-of-war between the motors.

Secondly, the recombinant expression and *in vitro* reconstitution of the tripartite complex paves the way for a detailed *in vitro* dissection of MyoVa in complex with both adaptor proteins. So far, only few studies investigated MyoVa in the presence of one or both adaptor proteins. The drawback of these studies was, however, that proteins were mixed without removing excess subunits from the assays. The optimized strategy to assemble the MyoVa transport complex *in vitro* presented in this thesis now allows a detailed mechanistic investigation of the functional and physiologically relevant complex. Further conceivable experiments involve building an 'artificial' melanosome *in vitro* by linking the tripartite complex to silica beads and investigate its behavior on 2D or even 3D built networks of actin filaments and MTs. Binding kinesin-2 and/or dynein to the MyoVa-covered artificial melanosome would lend the setup a further layer of complexity and make it ideal to study motor coordination *in vitro*. This *in vitro* reconstituted melanosome would allow to test potential regulators and their impact on overall transport under defined and precisely controllable conditions. Precise manipulation of distinct motor proteins or

specific protein domains would expand our understanding of the mechanisms coordinating MyoVa, kinesin, and dynein that join forces to correctly deliver melanosomes within the cell.

Most importantly, further data will be needed to provide evidence that Mlph phosphorylation modulates Mlph's affinity for MTs and thereby biases melanosome transport direction in cells. Specifically, *in vivo* experiments are of fundamental importance to support this hypothesis. Several residues involved in the MT-Mlph interaction were identified during the course of this study. Different combinations of these residues should be point-mutated to mimic the dephosphorylated (mutation of serine/threonine residues to alanines) or phosphorylated state (mutation of serine/threonine residues to aspartic or glutamic acids) of Mlph's ABD. These mutants should be transfected into the mouse melanocyte cell line lacking endogenous Mlph that are called leaden melanocytes (134). These melanocytes exhibit defects in melanosome transport to the dendritic tips and melanosomes are clustered in the perinuclear region. According to the model, dephosphorylation of Mlph's increases the affinity of melanosomes for MTs. Therefore, dephos-mimetic versions of Mlph are predicted to at least partially inhibit melanosome transport to the dendritic tips, because melanosomes prefer to stay on MTs. As switching from MT onto actin is a prerequisite for melanosome dispersion, the dephos-mimetic Mlph mutants are expected to impair dispersion. On the other hand, transfection of the phos-mimetic versions of Mlph is expected not to interfere with the dispersion of pigment granules (switching from MT to actin filaments), but switching melanosomes from actin filaments onto MTs should be affected.

Collectively, this study offers novel and unexpected mechanistic insights into how cells might bias the direction of a moving organelle that deserve further attention in the future.

8. **Supporting information**
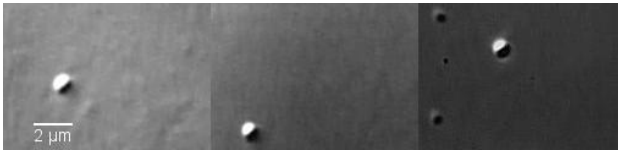
Video 1: Examples of MyoVa-dependent melanosome transport derived from the dispersed cell state on F-actin *in vitro*. Movie is displayed at 4X speed.


Video 2: MyoVa-dependent melanosome transport derived from the aggregated cell state and reactivated with cytoplasmic extract from the dispersed cell state. Movie is displayed at 4X speed.

Video 3: MyoVa-dependent melanosome transport derived from the aggregated cell state and reactivated with exogenous, purified PKA. Movie is displayed at 4X speed.
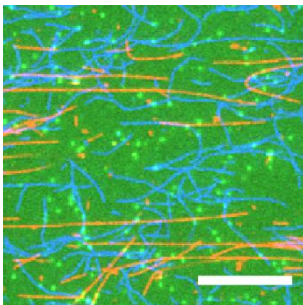
Video 4: Tripartite complex assembled with phosphorylated Mlph (green) assayed on a surface-attached network of MTs (red) and actin filaments (blue) *in vitro*. The transport complex largely ignores the MTs and displays directional movement on the actin network. Scale bar: 10 μm. Movie is displayed at 7.4X speed.
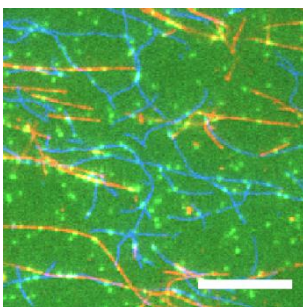
Video 5: Tripartite complex reconstituted with dephosphorylated Mlph assayed on a surface-attached network of MTs and actin filaments *in vitro*. Colors are the same as in Video 4. Dephosphorylation of Mlph is sufficient to redirect the MyoVa-dependent transport complex from the actin to the MT network. Scale bar: 10 μm. Movie is displayed at 7.4X speed.
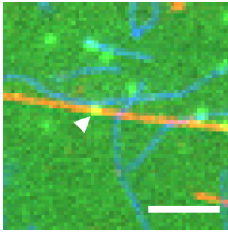
Video 6: MyoVa transport complex switching from a MT onto a crossing actin filament *in vitro*. MTs are shown in red, actin filaments in blue, and the protein complex in green color. Scale bar: 3 μm. Movie is displayed at 2.2X speed.
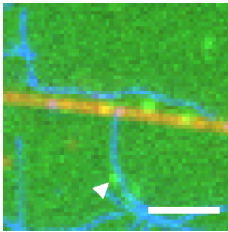
Video 7: Tripartite complex switching from an actin filament onto a crossing MT *in vitro*. Colors are the same as in Video 6. Scale bar: 3 μm. Movie is displayed at 2.2X speed.

9. <u>References</u>

1.   Wordeman L (2010) How kinesin motor proteins drive mitotic spindle function: Lessons from molecular assays. *Semin Cell Dev Biol* 21 (3):260-8, 10.1016/j.semcdb.2010.01.018.

2.   Heald R (2000) Motor function in the mitotic spindle. *Cell* 102 (4):399-402,

3.   Sharp DJ, Rogers GC, Scholey JM (2000) Microtubule motors in mitosis. *Nature* 407 (6800):41-7, 10.1038/35024000.

4.   Goldstein LS, Philp AV (1999) The road less traveled: emerging principles of kinesin motor utilization. *Annu Rev Cell Dev Biol* 15:141-83, 10.1146/annurev.cellbio.15.1.141.

5.   Allan VJ, Schroer TA (1999) Membrane motors. *Curr Opin Cell Biol* 11 (4):476-82,

6.   Lane J, Allan V (1998) Microtubule-based membrane movement. *Biochim Biophys Acta* 1376 (1):27-55,

7.   Wasmeier C, Hume AN, Bolasco G, Seabra MC (2008) Melanosomes at a glance. *J Cell Sci* 121 (Pt 24):3995-9, 10.1242/jcs.040667.

8.   Nascimento AA, Roland JT, Gelfand VI (2003) Pigment cells: a model for the study of organelle   transport.   *Annu   Rev   Cell   Dev   Biol*   19:469-91, 10.1146/annurev.cellbio.19.111401.092937.

9.   Aspengren S, Hedberg D, Skold HN, Wallin M (2009) New insights into melanosome transport in vertebrate pigment cells. *Int Rev Cell Mol Biol* 272:245-302, 10.1016/S1937-6448(08)01606-7.

10.   Mackintosh JA (2001) The antimicrobial properties of melanocytes, melanosomes and melanin and the evolution of black skin. *J Theor Biol* 211 (2):101-13, 10.1006/jtbi.2001.2331.

11.   Daniolos A, Lerner AB, Lerner MR (1990) Action of light on frog pigment cells in culture. *Pigment Cell Res* 3 (1):38-43,

12.   Rogers SL, Tint IS, Fanapour PC, Gelfand VI (1997) Regulated bidirectional motility of melanophore pigment granules along microtubules in vitro. *Proc Natl Acad Sci U S A* 94 (8):3720-5,

13.   Tuma MC, Zill A, Le Bot N, Vernos I, Gelfand V (1998) Heterotrimeric kinesin II is the microtubule motor protein responsible for pigment dispersion in Xenopus melanophores. *J Cell Biol* 143 (6):1547-58,

14.   Rodionov VI, Gyoeva FK, Gelfand VI (1991) Kinesin is responsible for centrifugal movement of pigment granules in melanophores. *Proc Natl Acad Sci U S A* 88 (11):4956-60,

15.   Rogers SL, Gelfand VI (1998) Myosin cooperates with microtubule motors during organelle transport in melanophores. *Curr Biol* 8 (3):161-4,

16.   Frost R, Norstrom E, Bodin L, Langhammer C, Sturve J, Wallin M, et al. (2013) Acoustic detection of melanosome transport in Xenopus laevis melanophores. *Anal Biochem* 435 (1):10-8, 10.1016/j.ab.2012.12.004.

17.   Euteneuer U, McIntosh JR (1981) Polarity of some motility-related microtubules. *Proc Natl Acad Sci U S A* 78 (1):372-6,

18.   Obika M (1986) Intracellular transport of pigment granules in fish chromatophores. *Zool Sci* (3):1-11,

19.   Porter KR (1973) Microtubules in intracellular locomotion. *Ciba Found Symp* 14:149-69,

20.   Schliwa M (1984) Mechanisms of intracellular organelle transport. *Cell Muscle Motil* 5:1-82,403-6,

21.   Schliwa M, Euteneuer U (1978) A microtuble-independent component may be involved in granule transport in pigment cells. *Nature* 273 (5663):556-8,

22.   Rodionov VI, Hope AJ, Svitkina TM, Borisy GG (1998) Functional coordination of microtubule-based and actin-based motility in melanophores. *Curr Biol* 8 (3):165-8,

23.   Koyama YI, Takeuchi T (1980) Differential effect of cytochalasin B on the aggregation of melanosomes in cultured mouse melanoma cells. *Anat Rec* 196 (4):449-59, 10.1002/ar.1091960410.

24.   Vaughan KT, Vallee RB (1995) Cytoplasmic dynein binds dynactin through a direct interaction between the intermediate chains and p150Glued. *J Cell Biol* 131 (6 Pt 1):1507-16,

25.   Karki S, Holzbaur EL (1995) Affinity chromatography demonstrates a direct binding between cytoplasmic dynein and the dynactin complex. *J Biol Chem* 270 (48):28806-11,

26.   Schroer TA (2004) Dynactin. *Annu Rev Cell Dev Biol* 20:759-79, 10.1146/annurev.cellbio.20.012103.094623.

27.   Karki S, Holzbaur EL (1999) Cytoplasmic dynein and dynactin in cell division and intracellular transport. *Curr Opin Cell Biol* 11 (1):45-53,

28.   Gill SR, Schroer TA, Szilak I, Steuer ER, Sheetz MP, Cleveland DW (1991) Dynactin, a conserved, ubiquitously expressed component of an activator of vesicle motility mediated by cytoplasmic dynein. *J Cell Biol* 115 (6):1639-50,

29.   Waterman-Storer CM, Karki SB, Kuznetsov SA, Tabb JS, Weiss DG, Langford GM, et al. (1997) The interaction between cytoplasmic dynein and dynactin is required for fast axonal transport. *Proc Natl Acad Sci U S A* 94 (22):12180-5,

30.   Deacon SW, Serpinskaya AS, Vaughan PS, Lopez Fanarraga M, Vernos I, Vaughan KT, et al. (2003) Dynactin is required for bidirectional organelle transport. *J Cell Biol* 160 (3):297-301, 10.1083/jcb.200210066.

31.   Hammer JA, 3rd, Sellers JR (2012) Walking to work: roles for class V myosins as cargo transporters. *Nat Rev Mol Cell Biol* 13 (1):13-26, 10.1038/nrm3248.

32.   Yildiz A, Forkey JN, McKinney SA, Ha T, Goldman YE, Selvin PR (2003) Myosin V walks hand-over-hand: single fluorophore imaging with 1.5-nm localization. *Science* 300 (5628):2061-5, 10.1126/science.1084398.

33.   Seperack PK, Mercer JA, Strobel MC, Copeland NG, Jenkins NA (1995) Retroviral sequences located within an intron of the dilute gene alter dilute expression in a tissue-specific manner. *EMBO J* 14 (10):2326-32,

34.   Mercer JA, Seperack PK, Strobel MC, Copeland NG, Jenkins NA (1991) Novel myosin heavy chain encoded by murine dilute coat colour locus. *Nature* 349 (6311):709-13, 10.1038/349709a0.

35.   Krendel M, Mooseker MS (2005) Myosins: tails (and heads) of functional diversity. *Physiology (Bethesda)* 20:239-51, 10.1152/physiol.00014.2005.

36.   Mehta AD, Rock RS, Rief M, Spudich JA, Mooseker MS, Cheney RE (1999) Myosin-V is a processive actin-based motor. *Nature* 400 (6744):590-3, 10.1038/23072.

37.   Sckolnick M, Krementsova EB, Warshaw DM, Trybus KM (2013) More than just a cargo adapter, melanophilin prolongs and slows processive runs of myosin Va. *J Biol Chem* 288 (41):29313-22, 10.1074/jbc.M113.476929.

38.   Wilson SM, Yip R, Swing DA, O'Sullivan TN, Zhang Y, Novak EK, et al. (2000) A mutation in Rab27a causes the vesicle transport defects observed in ashen mice. *Proc Natl Acad Sci U S A* 97 (14):7933-8, 10.1073/pnas.140212797.

39.   Matesic LE, Yip R, Reuss AE, Swing DA, O'Sullivan TN, Fletcher CF, et al. (2001) Mutations in Mlph, encoding a member of the Rab effector family, cause the melanosome transport defects observed in leaden mice. *Proc Natl Acad Sci U S A* 98 (18):10238-43, 10.1073/pnas.181336698.

40.   Provance DW, James TL, Mercer JA (2002) Melanophilin, the product of the leaden locus, is required for targeting of myosin-Va to melanosomes. *Traffic* 3 (2):124-32,

41.   Hume AN, Collinson LM, Hopkins CR, Strom M, Barral DC, Bossi G, et al. (2002) The leaden gene product is required with Rab27a to recruit myosin Va to melanosomes in melanocytes. *Traffic* 3 (3):193-202,

42.   Wu XS, Rao K, Zhang H, Wang F, Sellers JR, Matesic LE, et al. (2002) Identification of an organelle receptor for myosin-Va. *Nat Cell Biol* 4 (4):271-8, 10.1038/ncb760.

43.   Fukuda M, Kuroda TS, Mikoshiba K (2002) Slac2-a/melanophilin, the missing link between Rab27 and myosin Va: implications of a tripartite protein complex for melanosome transport. *J Biol Chem* 277 (14):12432-6, 10.1074/jbc.C200005200.

44.   Strom M, Hume AN, Tarafder AK, Barkagianni E, Seabra MC (2002) A family of Rab27-binding proteins. Melanophilin links Rab27a and myosin Va function in melanosome transport. *J Biol Chem* 277 (28):25423-30, 10.1074/jbc.M202574200.

45.   Kuroda TS, Fukuda M, Ariga H, Mikoshiba K (2002) The Slp homology domain of synaptotagmin-like proteins 1-4 and Slac2 functions as a novel Rab27A binding domain. *J Biol Chem* 277 (11):9212-8, 10.1074/jbc.M112414200.

46.   Fukuda M (2002) Synaptotagmin-like protein (Slp) homology domain 1 of Slac2-a/melanophilin is a critical determinant of GTP-dependent specific binding to Rab27A. *J Biol Chem* 277 (42):40118-24, 10.1074/jbc.M205765200.

47.   Au JS, Huang JD (2002) A tissue-specific exon of myosin Va is responsible for selective cargo binding in melanocytes. *Cell Motil Cytoskeleton* 53 (2):89-102, 10.1002/cm.10061.

48.   Kuroda TS, Ariga H, Fukuda M (2003) The actin-binding domain of Slac2-a/melanophilin is required for melanosome distribution in melanocytes. *Mol Cell Biol* 23 (15):5245-55,

49.   Fukuda M, Kuroda TS (2002) Slac2-c (synaptotagmin-like protein homologue lacking C2 domains-c), a novel linker protein that interacts with Rab27, myosin Va/VIIa, and actin. *J Biol Chem* 277 (45):43096-103, 10.1074/jbc.M203862200.

50.   Wu XS, Tsan GL, Hammer JA, 3rd (2005) Melanophilin and myosin Va track the microtubule plus end on EB1. *J Cell Biol* 171 (2):201-7, 10.1083/jcb.200503028.

51.   Park M, Serpinskaya AS, Papalopulu N, Gelfand VI (2007) Rab32 regulates melanosome transport in Xenopus melanophores by protein kinase a recruitment. *Curr Biol* 17 (23):2030-4, 10.1016/j.cub.2007.10.051.

52.   Kashina AS, Semenova IV, Ivanov PA, Potekhina ES, Zaliapin I, Rodionov VI (2004) Protein kinase A, which regulates intracellular transport, forms complexes with molecular motors on organelles. *Curr Biol* 14 (20):1877-81, 10.1016/j.cub.2004.10.003.

53.   de Graan PN, Eberle AN (1980) Irreversible stimulation of Xenopus melanophores by photoaffinity labelling with p-azidophenylalanine13-alpha-melanotropin. *FEBS Lett* 116 (1):111-5,

54.   Abe K, Robison GA, Liddle GW, Butcher RW, Nicholson WE, Baird CE (1969) Role of cyclic AMP in mediating the effects of MSH, norepinephrine, and melatonin on frog skin color. *Endocrinology* 85 (4):674-82, 10.1210/endo-85-4-674.

55.   Magun B (1973) Two actions of cyclic AMP on melanosome movement in frog skin. Dissection by cytochalasin B. *J Cell Biol* 57 (3):845-58,

56.   Potenza MN, Lerner MR (1992) A rapid quantitative bioassay for evaluating the effects of ligands upon receptors that modulate cAMP levels in a melanophore cell line. *Pigment Cell Res* 5 (6):372-8,

57.   Reilein AR, Tint IS, Peunova NI, Enikolopov GN, Gelfand VI (1998) Regulation of organelle movement in melanophores by protein kinase A (PKA), protein kinase C (PKC), and protein phosphatase 2A (PP2A). *J Cell Biol* 142 (3):803-13,

58.   Sugden D, Rowe SJ (1992) Protein kinase C activation antagonizes melatonin-induced pigment aggregation in Xenopus laevis melanophores. *J Cell Biol* 119 (6):1515-21,

59.   de Graan PN, van Dorp CJ, vad de Veerdonk FC (1982) Calcium requirement for alpha-MSH action on tail-fin melanophores of xenopus tadpoles. *Mol Cell Endocrinol* 26 (3):315-26,

60.   de Graan PN, Eberle AN, van de Veerdonk FC (1982) Calcium sites in MSH stimulation of xenopus melanophores: studies with photoreactive alpha-MSH. *Mol Cell Endocrinol* 26 (3):327-9,

61.   Deacon SW, Nascimento A, Serpinskaya AS, Gelfand VI (2005) Regulation of bidirectional melanosome transport by organelle bound MAP kinase. *Curr Biol* 15 (5):459-63, 10.1016/j.cub.2004.12.074.

62.   Isoldi MC, Rollag MD, Castrucci AM, Provencio I (2005) Rhabdomeric phototransduction initiated by the vertebrate photopigment melanopsin. *Proc Natl Acad Sci U S A* 102 (4):1217-21, 10.1073/pnas.0409252102.

63.   Passeron T, Bahadoran P, Bertolotto C, Chiaverini C, Busca R, Valony G, et al. (2004) Cyclic AMP promotes a peripheral distribution of melanosomes and stimulates melanophilin/Slac2-a and actin association. *FASEB J* 18 (9):989-91, 10.1096/fj.03-1240fje.

64.   Lerner AB, Case JD, Takahashi Y (1960) Isolation of melatonin and 5-methoxyindole-3-acetic acid from bovine pineal glands. *J Biol Chem* 235:1992-7,

65.   Ebisawa T, Karne S, Lerner MR, Reppert SM (1994) Expression cloning of a high-affinity melatonin receptor from Xenopus dermal melanophores. *Proc Natl Acad Sci U S A* 91 (13):6133-7,

66.   White BH, Sekura RD, Rollag MD (1987) Pertussis toxin blocks melatonin-induced pigment aggregation in Xenopus dermal melanophores. *J Comp Physiol B* 157 (2):153-9,

67.   Andersson TP, Skold HN, Svensson SP (2003) Phosphoinositide 3-kinase is involved in Xenopus and Labrus melanophore aggregation. *Cell Signal* 15 (12):1119-27,

68.   Karlsson AM, Lerner MR, Unett D, Lundstrom I, Svensson SP (2000) Melatonin-induced organelle movement in melanophores is coupled to tyrosine phosphorylation of a high molecular weight protein. *Cell Signal* 12 (7):469-74,

69.   Aspengren S, Wallin M (2004) A role for spectrin in dynactin-dependent melanosome transport in Xenopus laevis melanophores. *Pigment Cell Res* 17 (3):295-301, 10.1111/j.1600-0749.2004.00150.x.

70.   Andersson TP, Svensson SP, Karlsson AM (2003) Regulation of melanosome movement by MAP kinase. *Pigment Cell Res* 16 (3):215-21,

71.   Zaliapin I, Semenova I, Kashina A, Rodionov V (2005) Multiscale trend analysis of microtubule transport in melanophores. *Biophys J* 88 (6):4008-16, 10.1529/biophysj.104.057083.

72.   Rogers SL, Karcher RL, Roland JT, Minin AA, Steffen W, Gelfand VI (1999) Regulation of melanosome movement in the cell cycle by reversible association with myosin V. *J Cell Biol* 146 (6):1265-76,

73.   Gross SP, Tuma MC, Deacon SW, Serpinskaya AS, Reilein AR, Gelfand VI (2002) Interactions and regulation of molecular motors in Xenopus melanophores. *J Cell Biol* 156 (5):855-65, 10.1083/jcb.200105055.

74.   Levi V, Serpinskaya AS, Gratton E, Gelfand V (2006) Organelle transport along microtubules in Xenopus melanophores: evidence for cooperation between multiple motors. *Biophys J* 90 (1):318-27, 10.1529/biophysj.105.067843.

75.   Welte MA, Gross SP, Postner M, Block SM, Wieschaus EF (1998) Developmental regulation of vesicle transport in Drosophila embryos: forces and kinetics. *Cell* 92 (4):547-57,

76.   Schroer TA, Schnapp BJ, Reese TS, Sheetz MP (1988) The role of kinesin and other soluble factors in organelle movement along microtubules. *J Cell Biol* 107 (5):1785-92,

77.   King SJ, Schroer TA (2000) Dynactin increases the processivity of the cytoplasmic dynein motor. *Nat Cell Biol* 2 (1):20-4, 10.1038/71338.

78.   Berezuk MA, Schroer TA (2007) Dynactin enhances the processivity of kinesin-2. *Traffic* 8 (2):124-9, 10.1111/j.1600-0854.2006.00517.x.

79.   Schroeder HW, 3rd, Mitchell C, Shuman H, Holzbaur EL, Goldman YE (2010) Motor number controls cargo switching at actin-microtubule intersections in vitro. *Curr Biol* 20 (8):687-96, 10.1016/j.cub.2010.03.024.

80.   Schroeder HW, 3rd, Hendricks AG, Ikeda K, Shuman H, Rodionov V, Ikebe M, et al. (2012) Force-dependent detachment of kinesin-2 biases track switching at cytoskeletal filament intersections. *Biophys J* 103 (1):48-58, 10.1016/j.bpj.2012.05.037.

81.   Rodionov V, Yi J, Kashina A, Oladipo A, Gross SP (2003) Switching between microtubule- and actin-based transport systems in melanophores is controlled by cAMP levels. *Curr Biol* 13 (21):1837-47,

82.   Slepchenko BM, Semenova I, Zaliapin I, Rodionov V (2007) Switching of membrane organelles between cytoskeletal transport systems is determined by regulation of the microtubule-based transport. *J Cell Biol* 179 (4):635-41, 10.1083/jcb.200705146.

83.   Sheets L, Ransom DG, Mellgren EM, Johnson SL, Schnapp BJ (2007) Zebrafish melanophilin facilitates melanosome dispersion by regulating dynein. *Curr Biol* 17 (20):1721-34, 10.1016/j.cub.2007.09.028.

84.   Ali MY, Krementsova EB, Kennedy GG, Mahaffy R, Pollard TD, Trybus KM, et al. (2007) Myosin Va maneuvers through actin intersections and diffuses along microtubules. *Proc Natl Acad Sci U S A* 104 (11):4332-6, 10.1073/pnas.0611471104.

85.   Zimmermann D, Abdel Motaal B, Voith von Voithenberg L, Schliwa M, Okten Z (2011) Diffusion of myosin V on microtubules: a fine-tuned interaction for which E-hooks are dispensable. *PLoS One* 6 (9):e25473, 10.1371/journal.pone.0025473.

86.   Smith GE, Ju G, Ericson BL, Moschera J, Lahm HW, Chizzonite R, et al. (1985) Modification and secretion of human interleukin 2 produced in insect cells by a baculovirus expression vector. *Proc Natl Acad Sci U S A* 82 (24):8404-8,

87.   Vaughn JL, Fan F (1997) Differential requirements of two insect cell lines for growth in serum-free medium. *In Vitro Cell Dev Biol Anim* 33 (6):479-82, 10.1007/s11626-997-0067-5.

88.   Vaughn JL, Goodwin RH, Tompkins GJ, McCawley P (1977) The establishment of two cell lines from the insect Spodoptera frugiperda (Lepidoptera; Noctuidae). *In Vitro* 13 (4):213-7,

89.   Sambrook J, Russell DW. Molecular cloning : a laboratory manual. 3. ed. Cold Spring Harbor, NY: Cold Spring Harbor Laboratory Press; 2001.

90.   Zimmermann D. Dissertation. Involvement of myosin V in organelle transport and its unconventional interaction with microtubules. LMU München, 2012. https://edoc.ub.uni-muenchen.de/14668/.

91.   Schneider CA, Rasband WS, Eliceiri KW (2012) NIH Image to ImageJ: 25 years of image analysis. *Nat Methods* 9 (7):671-5,

92.   Spudich JA, Watt S (1971) The regulation of rabbit skeletal muscle contraction. I. Biochemical studies of the interaction of the tropomyosin-troponin complex with actin and the proteolytic fragments of myosin. *J Biol Chem* 246 (15):4866-71,

93.   Wegner A (1976) Head to tail polymerization of actin. *J Mol Biol* 108 (1):139-50,

94.   Mandelkow EM, Herrmann M, Ruhl U (1985) Tubulin domains probed by limited proteolysis and subunit-specific antibodies. *J Mol Biol* 185 (2):311-27,

95.   Wang F, Chen L, Arcucci O, Harvey EV, Bowers B, Xu Y, et al. (2000) Effect of ADP and ionic strength on the kinetic and motile properties of recombinant mouse myosin V. *J Biol Chem* 275 (6):4329-35,

96.   Keppler A, Pick H, Arrivoli C, Vogel H, Johnsson K (2004) Labeling of fusion proteins with synthetic fluorophores in live cells. *Proc Natl Acad Sci U S A* 101 (27):9955-9, 10.1073/pnas.0401923101.

97.   Los GV, Wood K (2007) The HaloTag: a novel technology for cell imaging and protein analysis. *Methods Mol Biol* 356:195-208,

98.   Ali MY, Lu H, Bookwalter CS, Warshaw DM, Trybus KM (2008) Myosin V and Kinesin act as tethers to enhance each others' processivity. *Proc Natl Acad Sci U S A* 105 (12):4691-6, 10.1073/pnas.0711531105.

99.   Scheres SH, Nunez-Ramirez R, Sorzano CO, Carazo JM, Marabini R (2008) Image processing for electron microscopy single-particle analysis using XMIPP. *Nat Protoc* 3 (6):977-90, 10.1038/nprot.2008.62.

100.   Carter NJ, Cross RA (2005) Mechanics of the kinesin step. *Nature* 435 (7040):308-12, 10.1038/nature03528.

101.   Larkin MA, Blackshields G, Brown NP, Chenna R, McGettigan PA, McWilliam H, et al. (2007) Clustal W and Clustal X version 2.0. *Bioinformatics* 23 (21):2947-8, 10.1093/bioinformatics/btm404.

102.   Hall TA (1999) BioEdit: a user-friendly biological sequence alignment editor and analysis program for Windows 95/98/NT. *Nucl Acids Symp Ser* (41):95-8,

103.   Rappsilber J, Ishihama Y, Mann M (2003) Stop and go extraction tips for matrix-assisted laser desorption/ionization, nanoelectrospray, and LC/MS sample pretreatment in proteomics. *Anal Chem* 75 (3):663-70,

104.   Nagaraj N, Kulak NA, Cox J, Neuhauser N, Mayr K, Hoerning O, et al. (2012) System-wide perturbation analysis with nearly complete coverage of the yeast proteome by single-shot ultra HPLC runs on a bench top Orbitrap. *Mol Cell Proteomics* 11 (3):M111 013722, 10.1074/mcp.M111.013722.

105.   Cox J, Mann M (2008) MaxQuant enables high peptide identification rates, individualized p.p.b.-range mass accuracies and proteome-wide protein quantification. *Nat Biotechnol* 26 (12):1367-72, 10.1038/nbt.1511.

106.   Cox J, Neuhauser N, Michalski A, Scheltema RA, Olsen JV, Mann M (2011) Andromeda: a peptide search engine integrated into the MaxQuant environment. *J Proteome Res* 10 (4):1794-805, 10.1021/pr101065j.

107.   Sbalzarini IF, Koumoutsakos P (2005) Feature point tracking and trajectory analysis for video imaging in cell biology. *J Struct Biol* 151 (2):182-95,

108.   Helenius J, Brouhard G, Kalaidzidis Y, Diez S, Howard J (2006) The depolymerizing kinesin MCAK uses lattice diffusion to rapidly target microtubule ends. *Nature* 441 (7089):115-9, 10.1038/nature04736.

109.   Otsu N (1979) A Threshold Selection Method from Gray-Level Histograms. *IEEE Transactions on Systems, Man, and Cybernetics* 9 (1):62-6,

110.   Chabrillat ML, Wilhelm C, Wasmeier C, Sviderskaya EV, Louvard D, Coudrier E (2005) Rab8 regulates the actin-based movement of melanosomes. *Mol Biol Cell* 16 (4):1640-50, 10.1091/mbc.E04-09-0770.

111.   Chijiwa T, Mishima A, Hagiwara M, Sano M, Hayashi K, Inoue T, et al. (1990) Inhibition of forskolin-induced neurite outgrowth and protein phosphorylation by a newly synthesized selective inhibitor of cyclic AMP-dependent protein kinase, N-[2-(p-bromocinnamylamino)ethyl]-5-isoquinolinesulfonamide (H-89), of PC12D pheochromocytoma cells. *J Biol Chem* 265 (9):5267-72,

112.   Ono-Saito N, Niki I, Hidaka H (1999) H-series protein kinase inhibitors and potential clinical applications. *Pharmacol Ther* 82 (2-3):123-31,

113.   Hidaka H, Watanabe M, Kobayashi R (1991) Properties and use of H-series compounds as protein kinase inhibitors. *Methods Enzymol* 201:328-39,

114.   Hume AN, Collinson LM, Rapak A, Gomes AQ, Hopkins CR, Seabra MC (2001) Rab27a regulates the peripheral distribution of melanosomes in melanocytes. *J Cell Biol* 152 (4):795-808,

115.   Nagashima K, Torii S, Yi Z, Igarashi M, Okamoto K, Takeuchi T, et al. (2002) Melanophilin directly links Rab27a and myosin Va through its distinct coiled-coil regions. *FEBS Lett* 517 (1-3):233-8,

116.   Wu X, Rao K, Bowers MB, Copeland NG, Jenkins NA, Hammer JA, 3rd (2001) Rab27a enables myosin Va-dependent melanosome capture by recruiting the myosin to the organelle. *J Cell Sci* 114 (Pt 6):1091-100,

117.   Wu X, Sakamoto T, Zhang F, Sellers JR, Hammer JA, 3rd (2006) In vitro reconstitution of a transport complex containing Rab27a, melanophilin and myosin Va. *FEBS Lett* 580 (25):5863-8, 10.1016/j.febslet.2006.09.047.

118.   Geething NC, Spudich JA (2007) Identification of a minimal myosin Va binding site within an intrinsically unstructured domain of melanophilin. *J Biol Chem* 282 (29):21518-28, 10.1074/jbc.M701932200.

119.   Wei Z, Liu X, Yu C, Zhang M (2013) Structural basis of cargo recognitions for class V myosins. *Proc Natl Acad Sci U S A* 110 (28):11314-9, 10.1073/pnas.1306768110.

120.   Li XD, Ikebe R, Ikebe M (2005) Activation of myosin Va function by melanophilin, a specific docking partner of myosin Va. *J Biol Chem* 280 (18):17815-22, 10.1074/jbc.M413295200.

121.   Eriksson TL, Svensson SP, Lundstrom I, Persson K, Andersson TP, Andersson RG (2008) Panax ginseng induces anterograde transport of pigment organelles in Xenopus melanophores. *J Ethnopharmacol* 119 (1):17-23, 10.1016/j.jep.2008.05.024.

122.   Huang JD, Mermall V, Strobel MC, Russell LB, Mooseker MS, Copeland NG, et al. (1998) Molecular genetic dissection of mouse unconventional myosin-VA: tail region mutations. *Genetics* 148 (4):1963-72,

123.   Wu X, Wang F, Rao K, Sellers JR, Hammer JA, 3rd (2002) Rab27a is an essential component of melanosome receptor for myosin Va. *Mol Biol Cell* 13 (5):1735-49, 10.1091/mbc.01-12-0595.

124.   Zanivan S, Gnad F, Wickstrom SA, Geiger T, Macek B, Cox J, et al. (2008) Solid tumor proteome and phosphoproteome analysis by high resolution mass spectrometry. *J Proteome Res* 7 (12):5314-26,

125.   Hornbeck PV, Zhang B, Murray B, Kornhauser JM, Latham V, Skrzypek E (2015) PhosphoSitePlus, 2014: mutations, PTMs and recalibrations. *Nucleic Acids Res* 43 (Database issue):D512-20, 10.1093/nar/gku1267.

126.   Ubersax JA, Ferrell JE, Jr. (2007) Mechanisms of specificity in protein phosphorylation. *Nat Rev Mol Cell Biol* 8 (7):530-41, 10.1038/nrm2203.

127.   Oberhofer A, Spieler P, Rosenfeld Y, Stepp WL, Cleetus A, Hume AN, et al. (2017) Myosin Va's adaptor protein melanophilin enforces track selection on the microtubule and actin networks in vitro. *Proc Natl Acad Sci USA* 10.1073/pnas.1619473114.

128.   Li XD, Mabuchi K, Ikebe R, Ikebe M (2004) Ca2+-induced activation of ATPase activity of myosin Va is accompanied with a large conformational change. *Biochem Biophys Res Commun* 315 (3):538-45, 10.1016/j.bbrc.2004.01.084.

129.   Liu J, Taylor DW, Krementsova EB, Trybus KM, Taylor KA (2006) Three-dimensional structure of the myosin V inhibited state by cryoelectron tomography. *Nature* 442 (7099):208-11, 10.1038/nature04719.

130.   Thirumurugan K, Sakamoto T, Hammer JA, 3rd, Sellers JR, Knight PJ (2006) The cargo-binding domain regulates structure and activity of myosin 5. *Nature* 442 (7099):212-5, 10.1038/nature04865.

131.   Wang F, Thirumurugan K, Stafford WF, Hammer JA, 3rd, Knight PJ, Sellers JR (2004) Regulated conformation of myosin V. *J Biol Chem* 279 (4):2333-6, 10.1074/jbc.C300488200.

132.   Yao LL, Cao QJ, Zhang HM, Zhang J, Cao Y, Li XD (2015) Melanophilin Stimulates Myosin-5a Motor Function by Allosterically Inhibiting the Interaction between the Head and Tail of Myosin-5a. *Sci Rep* 5:10874, 10.1038/srep10874.

133.   Wu X, Bowers B, Rao K, Wei Q, Hammer JA, 3rd (1998) Visualization of melanosome dynamics within wild-type and dilute melanocytes suggests a paradigm for myosin V function In vivo. *J Cell Biol* 143 (7):1899-918,

134.   Hume AN, Tarafder AK, Ramalho JS, Sviderskaya EV, Seabra MC (2006) A coiled-coil domain of melanophilin is essential for Myosin Va recruitment and melanosome transport in melanocytes. *Mol Biol Cell* 17 (11):4720-35, 10.1091/mbc.E06-05-0457.

10. Abbreviations

ABD   actin-binding domain

BD   binding domain

cAMP   cyclic adenosine monophosphate

C-terminus   carboxy terminus

DIC   differential interference contrast

F-actin   filamentous actin

G-actin   globular actin

GTD   globular tail domain

GTPase   guanosine triphosphatase

Mlph   melanophilin

*Mm*Mlph   melanophilin from *Mus musculus*

*Xl*Mlph   melanophilin from *Xenopus laevis*

*Xt*Mlph   melanophilin from *Xenopus tropicalis*

MT   microtubule

MyoVa   myosin Va

*Mm*MyoVa   myosin Va from *Mus musculus*

*Xl*MyoVa   myosin Va from *Xenopus laevis*

N-terminus   amino terminus

*Mm*Rab27a   Rab27a from *Mus musculus*

*Xl*Rab27a   Rab27a from *Xenopus laevis*

PAGE   polyacryl amide gel electrophoresis

PCR   polymerase chain reaction

PKA   protein kinase A

SD   standard deviation

Slp   synaptotagmin-like protein

SEM   standard error of the mean

SDS   sodium dodecyl sulfate

S.O.C.   Super optimal catabolite

TIRF   total internal reflection fluorescence

α-MSH   α-melanocyte-stimulating hormone

Acknowledgements

First and foremost, I am very indebted to Prof. Manfred Schliwa who convinced me and gave me the opportunity to start a PhD project on the fascinating motor proteins and always took the time to answer questions and give advice. I also thank Dr. Zeynep Ökten for supervising my PhD project, financing the last years, teaching me to think unconventionally and not to talk myself out of an experiment. During my PhD, I enjoyed a freedom to try experiments and follow 'crazy' ideas for what I am very grateful.

I would like to thank especially Thi-Hieu Ho for help with literally everything in the lab. Without you, the lab would not be as organized and nice to work in and my PhD project would have taken much longer! Many thanks also to Renate Dombi who patiently introduced me into cloning and helped with lab work in the Institute for Cell Biology!

Furthermore, I would like to thank my former colleagues Dr. Dennis Zimmermann, Dr. Süleyman Kösem, Dr. Marija Vukajlovic, Dr. Christoph Gallinger, Dr. Julia Gallinger, and Dr. Katharina von Roman for creating such a nice working atmosphere with conversations not only about science ☺. I am grateful to all the members of the former Institute for Cell Biology where I started my PhD thesis for providing an excellent environment to work in! Also, I thank my current colleagues at TUM for creating a small biological/chemical microsphere inside the Physics Department at TUM with lots of discussion and fun! Particularly, I am indebted to Willi Stepp who always helped me solve quantification problems and have a more physicist's view. Thanks to all the member of E22/E27 Biophysics for listening to many status reports, giving constructive input, and providing everything that is needed to work successfully in the lab!

A big thank you goes to Evi Meier and Hendrik Dietz from TUM without whom I would not have gotten those beautiful TEM images of myosin Va. Furthermore, I am grateful to Edgar Boczek, Florian Schopf and Johannes Buchner for providing me access to the isotope lab at the Chemistry Department of TUM and helping me optimize *the in vitro* phosphorylation assays.

I am very thankful to be part of the graduate school "Protein Dynamics in Health and Disease" in the Elite Network of Bavaria and participate in numerous helpful workshops, attend interesting talks and retreats, and meet other PhD students who broadened my horizon!

Lastly, I want to express my deepest gratefulness to my family, in particular Matthias and Lukas! Thank you for unconditionally supporting and motivating me during this PhD thesis! You are the best!!